Systematic Investigations on Some Strategies for Enhancement of Supercavity Size

A Thesis submitted to the

UPES

For the Award of

Doctor of Philosophy

in

Aerospace Engineering

By

Kumar Gaurav

October 2024

Supervisor
Dr. Ashish Karn

**Mechanical Cluster
School of Advanced Engineering (SoAE)
UPES
Dehradun- 248007: Uttarakhand**

Systematic Investigations on Some Strategies for Enhancement of Supercavity Size

A Thesis submitted to the

UPES

For the Award of

Doctor of Philosophy

in

Aerospace Engineering

By

Kumar Gaurav

(SAP ID: 500072287)

October 2024

Supervisor
Dr. Ashish Karn
Sr. Associate Professor
Mechanical Cluster
UPES

UPES
UNIVERSITY OF TOMORROW

Mechanical Cluster
School of Advanced Engineering (SoAE)
UPES
Dehradun - 248007: Uttarakhand

DECLARATION

I declare that the thesis entitled "Numerical Investigations on Some Strategies for Enhancement of Supercavity Size" has been prepared by me under the guidance of Dr. Ashish Karn, Sr. Assoc. Professor of Mechanical Cluster, UPES. No part of this thesis has formed the basis for the award of any degree or fellowship previously.

Kumar Gaurav

Mechanical Cluster, School of Advanced Engineering (SoAE)

UPES, Dehradun - 248007: Uttarakhand.

DATE: 22/09/24

CERTIFICATE

I certify that Kumar Gaurav has prepared his thesis entitled **"Systematic Investigations on Some Strategies for Enhancement of Supercavity Size",** for the award of PhD degree of the UPES, under my guidance. He has carried out the work at the Mechanical Engineering Cluster, UPES.

Internal Supervisor

Dr. Ashish Karn

Mechanical Cluster, School of Advanced Engineering (SoAE)

UPES, Dehradun - 248007: Uttarakhand.

DATE:

ABSTRACT

The phenomenon of supercavitation, characterized by the formation of a vapor-filled cavity around an underwater object, has attracted significant interest in fields such as naval engineering and underwater warfare. This study aims to explore and enhance supercavity formation, focusing on its size, shape, and behaviour under various conditions. By combining insights from multiphase flow dynamics, cavitator geometry, and thermal effects, the current research presents a comprehensive analysis aimed at improving the supercavity size and thus the performance of high-speed underwater vehicles, such as supercavitating torpedoes.

The first part of the current study pertains to the foundational aspects of elongated bubbles, which is crucial to understand the broader multiphase dynamics of coalescence that is involved in creation of a supercavity. The dynamics of elongated bubbles are influenced by numerous parameters such as flow rate, orifice size, fluid properties, and the height of fluid above the orifice. Experiments were conducted using different fluids, including water, acetone, and glycerol-water mixtures, to study the formation and behaviour of bubbles emerging from a submerged orifice. Through the use of high-speed cinematography and non-dimensional analysis, scaling laws were established between key parameters like the Reynolds, Weber, Froude, and Eotvos numbers. These relationships provide insight into elongated bubble geometries and the governing forces at play. This foundational understanding of elongated bubbles establishes the groundwork for investigating cavitation phenomena at larger scales.

Next, this study focuses on the ability of various cavitator shapes to generate supercavities of larger size and with minimal drag on the vehicle. Supercavitating torpedoes require effective cavitator designs to minimize skin friction drag while

maintaining a stable cavity. Thirteen different cavitator designs were simulated, with varying shapes and configurations. A disc-shaped cavitator was found to perform optimally, reducing skin friction drag by 92% at a cavitation number of 0.09. However, this drag reduction was offset by an increase in pressure drag, especially when the supercavity was larger than necessary to encompass the torpedo body. The study concluded that supercavity size must be precisely controlled, as excessive supercavities lead to increased pressure drag, while overly small supercavities result in greater skin friction drag. These results highlight the delicate balance required in cavitator design to achieve optimal performance, reinforcing the need to control supercavity size precisely.

Further, the current research also involves a ingenious technique for supercavity size enlargement: heat-enhanced supercavitation. In other words, the role of temperature—both cavitator and the surrounding fluid—on supercavity geometry was thoroughly explored. Through computational simulations, it was found that while cavitator temperature has negligible effects on supercavity formation, fluid temperature plays a crucial role. As the fluid temperature, the length of the supercavity increases significantly, particularly at lower cavitation numbers. This temperature sensitivity, however, diminishes as the cavitation number increases. The study also introduced a quadratic relationship between cavitation number and non-dimensional critical temperature, providing a predictive model for supercavity size based on thermal conditions. These findings are vital for the design of supercavitating vehicles operating in varying thermal environments, offering a method to enhance stability and performance by adjusting fluid temperature to control cavity size.

Finally, the fourth part of the study proposes a novel approach to further enhance supercavity dimensions through the use of secondary cavitators, which has hitherto not been explored. Typically, a single cavitator is mounted at the snout of a torpedo to generate a supercavity, but this research investigates the potential benefits of deploying a secondary cavitator at the rear portion of the vehicle. The simulations revealed that the secondary cavitator could significantly increase supercavity size,

particularly when placed at 80% of the primary supercavity length. This dual-cavitator configuration allows the vehicle to reach supercavitation at lower speeds, expanding the operational range of the torpedo. The interaction between the supercavities generated by the primary and secondary cavitators was found to occur within a narrow range of operational conditions, and the amplification in supercavity size was strongly correlated with the Froude number. This concept of using multiple cavitators provides a promising avenue for improving supercavity size control, enabling better performance and efficiency for high-speed underwater vehicles.

In conclusion, this comprehensive study provides significant advancements in understanding and controlling supercavitation dynamics. From the basic principles of elongated bubble to the complex interactions between cavitators and fluid temperatures, the research offers valuable insights into the mechanisms governing supercavity formation. The introduction of secondary cavitators as a method to enhance supercavity size represents a potential breakthrough in the design of supercavitating vehicles, offering greater flexibility and performance in underwater applications. These findings have broad implications for the development of next-generation underwater vehicles, where precise control over supercavity size is critical for achieving optimal speed, efficiency, and stability.

ACKNOWLEDGEMENT

Lastly, I would like to express my profound gratitude to my parents, parents-in-law, wife, brother, and sisters for their encouragement and unconditional support throughout this roller-coaster journey. They have been my constant source of motivation, giving me the perseverance to complete this work.

Finally, I am deeply appreciative of all those who have helped me, directly or indirectly, in the successful completion of my PhD.

Kumar Gaurav

TABLE OF CONTENTS

LIST OF FIGURES

LIST OF TABLES

Chapter 1

Introduction and Literature Survey

1.1 Elongated Bubbles

The characteristic of the formation process of bubble plays a vital role in many practical applications such as boiling (Coulibaly et al., 2014; Ivey, 1967), fermentation (Kheradmandnia et al., 2015), aeration(Karn, Ellis, Hong, et al., 2015b; Karn, Monson, Ellis, et al., 2015c), refrigeration (Benhmidene et al., 2011), drag reduction(Karn, Arndt, et al., 2016b; Karn & Rosiejka, 2017a), biomass energy (Rajaseenivasan & Srithar, 2017) and wastewater treatment (Painmanakul et al., 2010). Indeed, a large amount of work related to bubble behavior has been done in the past (De Jonge et al., 1982; X. Fan et al., 2008; Olowson & Almstedt, 1990; Park & Wang, 2015). This extensive prior literature has mainly focused on bubble geometry (Karn, Ellis, Milliren, et al., 2015a; Zhou et al., 2021), morphology (Calzavarini et al., 2008; Karn, Ellis, Hong, et al., 2015a), formation (Karn, Arndt, et al., 2016d), the coalescence process (Karn, Shao, et al., 2016; Olmos et al., 2001), mass transfer (Karn, Monson, Ellis, et al., 2015b; Wang & Wang, 2007) and regime classifications, all of which are crucially dependent on the forces acting on the bubbles. The principal forces acting on the gas bubbles while rising in liquid are the forces of surface tension, the upward buoyant force, and drag forces. The surface tension forces usually are responsible for keeping the bubbles in their most stable shape, i.e. a sphere, whereas the viscous drag force tries to deform it into a flattened shape. Further, for rising bubbles, bubble locomotion in a region of varying pressure distribution is another important factor, whether it is caused by decreasing hydrostatic pressure distribution or the low-pressure wake of advancing bubbles. Particularly, for large bubbles, the resistance force dominates over the forces of surface tension, causing them to take a highly unstable oscillating

1

flattened shape (Roig et al., 2012). Thus, bubble morphology is crucially governed by the magnitude of these forces, which typically depends on experimental parameters such as the gas flow rate, orifice shape and size, depth, and fluid properties. For instance, at low gas flow rates, the volume of the bubble is proportional to the surface tension and orifice radius, whereas, at high mass flow rates, the bubble volume is proportional to mass flow rate (Gerlach et al., 2007). Thus, the maximum diameter of the bubble can be predicted from the balance of surface tension, buoyancy, and drag force (Al-Hayes & Winterton, 1981).

The ratio of these forces also affects the formation process of the bubble. During the formation process, the bubble size is independent of injecting gas properties and liquid viscosity. However, the formation frequency does affect the bubble size, with higher frequencies yielding a larger bubble size. (Benzing & Myers, 1955). The buoyancy forces govern the bubble's rising velocity and hence also influences the bubble length. The higher bubble velocity stretches the bubble and results in a larger bubble length up to a certain limit (Agostini et al., 2008). The bubble velocity is directly proportional to the mass flow rate and vapor quality and inversely proportional to the saturation temperature. It can be expressed as a linear function of the two-phase superficial velocity (Arcanjo et al., 2010). Studies on the inclined pipes reported that the bubble drift velocity is directly proportional to the pipe inclination and diameter, and inversely proportional to the fluid viscosity (Livinus & Verdin, 2021).

Apart from the bubble formation, the bubbling process can be broadly classified into other regimes as well, for instance based on the gas injection Reynolds number : single bubbling, pairing and single coalescence, double coalescence, triple bubble formation, quadruple bubble formation, coalescence at the nozzle and triple or quadruple formation, chaining, and jetting (Kyriakides et al., 1997). Similarly, researchers have conducted experiments on a single submerged orifice and divided the formation of the bubbles into six different regimes according to liquid depth and gas velocity. These six regimes are meniscus,

steady jet, pulsating jet, imperfect bubble, perfect bubble, and deformed bubble (Muller & Prince, 1972).

After their formation, the bubbles rise and might merge into other bubbles forming a newer bubble of larger size. This process of bubble coalescence has been widely studied by researchers for the past several decades. The coalescence process is characterized by the formation of a neck connecting two bubbles, followed by a liquid drainage phenomenon. When the bubble coalescence is occurring away from solid walls, the neck radius is proportional to the square root of time elapsed since the moment of contact of the bubble interfaces. On the other hand, for the coalescence near the walls, the neck radius has been reported to be proportional to the 0.1 power of time since the bubble's interface contacted (Khadiya et al., 2021). The coalescence process can ordinarily occur only when the maximum liquid film length during collision is below a certain threshold limit, else the bubble collides and bounces off without merging (W. Yang et al., 2019). The coalescence of two bubbles also releases the surface energy, which generates interface velocity followed by damped prolate oscillations of large amplitude (Stover et al., 1997). The coalescence process accelerates while the coalescence region shrinks with the increase in bubble approach velocity (Orvalho et al., 2021). Some studies investigating the coalescence process have also explored the effect of electrolytes on bubble coalescence and it has been observed that the rate of bubble coalescence either decreases or remains constant on the addition of electrolytes to the working liquids (Craig et al., 1993b, 1993a).

In the recent past, bubbling experiments have been very extensively researched upon, particularly under some novel scenarios. For instance, the bubbling process was experimented under high pressure and temperature, and it is noted that the pressure and temperature have a significant impact on the behavior of bubble and bubble size distribution. (Leonard et al., 2021). During the bubble experiments from the micro-orifice, it is observed that the bubble formation mechanism is greatly affected by the gas kinetic energy and the capillary waves. As the bubble interface crosses its threshold value, the apex of the bubble

accelerates upward and the bubble forms a prolate configuration (Mohseni et al., 2020). In experimentation with periodic bubbling- bursting, it is observed that a continuous stream of gas penetrates through a thin liquid layer and is highly associated with orifice diameter. On increasing the thickness of the liquid layer, the jet first becomes thick and small and then gradually changes to a thin and long structure (Li et al., 2019). The effect of turbulence on the bubble size and population is also studied and found to have a prominent role. In the case of larger and fewer bubbles, the vertical fluctuating velocity component plays a vital role in the turbulent stresses (Wu et al., 2021).

Clearly, a vast amount of work has been done on the topic of bubble coalescence, yet the bubble morphology during its formation at the sub-millimeter orifice is not explored deeply. Previous works were also constrained with a limited range of operating conditions and generally focused on the effect of one or two parameters rather than a comprehensive effect. Moreover, due to limitations of resources in a few of the previously reported works such as the use of syringe pump in place of the orifice cannot reflect exact industrial applications. The bubble geometry reported by previous researchers did not consider a sufficient range of data sampling, which inherits some error in the results claimed. Therefore, in the present study, we have focused on the morphology of bubble rising and coalescence and the effect of various operating conditions on it. The influence of various operating parameters such as orifice size, flow rate, fluid properties, and fluid height is evaluated. Compared to previous similar work in this area, we have tried to quantify the cumulative effects of all operating parameters on bubble geometry during the formation process in terms of governing non-dimensional parameters such as Reynolds number, Weber number, Froude number, and Eotvos number. Simple scaling laws are also derived between Reynolds number and other non-dimensional parameters to predict the bubble geometry based on the operating conditions.

1.2 Supercavitation

Supercavitation is a phenomenon in which a cavitation bubble forms is large enough to encompass the whole object. The bubble reduces the area of the object exposed to the fluid, leading to a significant reduction in drag and hence allow the object to reach high speed underwater (Karn & Chawdhary, 2018; Nesteruk, 2012). This process involves creating a low-pressure region around the object, when the pressure drops below the vapour pressure of liquid the liquid starts to converts to vapour phase (Cao et al., 2017), which initiate the formation of multiple small bubbles. These small bubble later on coalesce with other to form a supercavity (Karn & Rosiejka, 2017b; Logvinovich & Serebryakov, 1975).

Supercavitation has a potential application in the fields involving high speed underwater transport, hydrofoil design, desalination, wastewater treatment and aeration etc. Over past decades, various researchers have demonstrated that the supercavitation has the potential to greatly enhance the speed and efficiency of submarines, torpedo (Alyanak et al., 2006). The studies concluded that the supercavitation provide an efficient, productive and sustainable approach for desalination applications (Likhachev et al., 2014; Zheng et al., 2019). The use of supercavitation in waste water treatment has the potential to increase the removal of pollutants, reduce energy consumption, and improve the overall sustainability of waste water treatment technologies (Dular et al., 2016; Sarc et al., 2018). Supercavitation has also been proved efficient in augmenting the overall performance of the aeration process (Schmid, 2010; Tomov et al., 2016).

Supercavitation can also be achieved artificially by injecting non-condensable gas at the nose of the underwater vehicle (Karn, Arndt, et al., 2016c). The gas form an envelope around the vehicle and act as supercavity (Shao et al., 2017). Once the vehicle passes, the supercavity collapses downstream of the object and gas start to leave in form of vortices, this referred to as the closure mechanism. The study of closure mechanism is critical in study of artificial supercavitation (Karn, Arndt, & Hong, 2015). Researchers have conducted studies that focuses on the physical

processes that control a ventilated supercavity's closure formation and transition between closure modes (Karn, Arndt, et al., 2016a).

Research on the augmentation of supercavity size has been an active area of investigation, with the goal of increasing the efficiency and performance of underwater propulsion systems. There have been studies related to shape optimize of vehicle to enhance supercavity size, for instance the study by Fan et. al. primarily focuses on the tail expansion and shrinkage impact on supercavitation. According to the study, an unsmooth expansion of the tail diameter will result in a new re-jet flow at the corner while a smooth expansion will demolish the cavity caused by the cavitator and minimise the upward movement of the rear jet (C. Fan et al., 2021). To artificially lengthen the supercavity, researchers have explored adopting a revolving non-axisymmetric cavitator. It was discovered that, despite a slight increase in drag force, the length of the supercavity grew as the rotational velocity increased. Overall, in comparison with a conventional disc cavitator, the length of the supercavity was larger against the same drag (S. Kim et al., 2022). An inviscid model for predicting the geometry of supercavitation is developed in a wide range of Froude numbers that accurately predicted the supercavity morphologies at high Froude number ($100 < Fr < 400$). However, due to the high effect of buoyancy in the case of low Froude number ($15 < Fr < 30$), the cavity morphologies were predicted with an error of 5–10% (J.-J. Yi et al., 2022). Since the supercavity forms through the coalescence of several small bubbles, the empirical relations developed in earlier studies to calculate the size of an elongated bubble formed by gas injection (Gaurav et al., 2022) can be extended to estimate the size of an artificial supercavity. Apart from this other mechanism such as use of microbubbles, textured surfaces were also employed to enhance the supercavity size. The cavity surface curvature and the process of gas shedding will be significantly influenced by the air-water free surface. The length diameter ratio of ventilated cavitation increases when free surface is present (Liu et al., 2023). Considerable amount of work has been done in optimizing cavitators for enhancing supercavity size. Previous studies have used disk cavitator, spherical cavitator,

conical cavitator and elliptical cavitator etc (Chen et al., 2023; M.-J. Kim et al., 2021; Shao et al., 2020). The extensive research in enhancing the size of the supercavity shows its importance in various applications.

A considerable amount of efforts has been made in the past to reduce the drag on underwater bodies using supercavitation (C.-X. Jiang et al., 2017; D. Yang et al., 2017; W. Yi et al., 2009). A numerical simulation on supercavities in water and turbulent drag-reducing solution have been conducted and it is observed that turbulent drag-reducing additives help promote supercavitation as well as further reduce drag (C.-X. Jiang et al., 2016). Researchers have also considered increasing the temperature of the gas that was injected in an attempt to expand the supercavity and further reduce drag (Y. Jiang et al., 2023). Previous research observed that an elevated liquid temperature is associated with an increase in both the rate of vapour production and the size of the supercavity. At 50 °C, the supercavity diameter enlarged by 53% as compared to the liquid temperature of 22 °C (Rajkumar et al., 2023). Researchers have performed numerical simulations to study the performance of a supercavitating propeller. The results showed a significant reduction in drag compared to a conventional propeller, demonstrating the potential for supercavitation in underwater propulsion (Matsuda et al., 1994). Studies have been conducted in the past to investigate the multi-factor-dependent and nonlinear hydrodynamic properties of a ventilated supercavitating vehicle with high Froude number. It was noticed that the hydrodynamic characteristic of ventilated supercavitating vehicles varies depending on position relationship between the supercavity perimeter and the solid surface and can be controlled and improved by tweaking the gas entrainment coefficient (Xu et al., 2023).

The present work provides an in-depth analysis of the supercavitation phenomenon and its application in high-speed heavyweight torpedoes, along with suggestions for methods to enhance the supercavitation cavity size. The research is organized into four distinct studies. The first study, presented in Chapter 3, investigates the formation and coalescence behaviour of elongated bubbles, laying the foundational

groundwork for understanding supercavitation. Experimental data obtained from this study are used to derive empirical relationships between key governing parameters, which can be applied to predict supercavitation characteristics. The second study, detailed in Chapter 4, focuses on the numerical investigation of supercavitation flow over a high-speed heavyweight torpedo. This study examines various cavitator shapes to determine the most effective design for generating supercavitation on such torpedoes. Chapters 5 and 6 are dedicated to exploring methods for enhancing supercavitation size. Chapter 5 presents a numerical study investigating the effects of temperature on supercavitation behavior, which is divided into two parts: the first part examines the use of a heated cavitator, while the second part explores the impact of using hot working fluid to enhance supercavitation. Chapter 6 examines the role of a secondary cavitator in increasing the size of the supercavitation cavity. This study involves the optimization of both the location and the height of the secondary cavitator to maximize the effectiveness of supercavitation.

1.3 Motivation:

The development of supercavitating torpedoes represents a cutting-edge advancement in naval warfare, with only five nations currently possessing this technology in their arsenals. As global maritime threats evolve, it becomes imperative for India to explore and develop this powerful capability. This research on supercavitating torpedoes is driven by several factors that make it a strategic priority for India.

1.3.1 India's Strategic Need for a Supercavitating Torpedo

India, with its vast coastline of approximately 7,500 km, faces unique security challenges. Nearly one-third of the nation's boundaries are vulnerable to enemy submarine incursions, especially as rival naval forces increase their presence in the Indian Ocean. Recent advancements in underwater warfare, including the

8

development of supercavitating torpedoes by neighbouring countries, pose a significant threat to India's maritime security.

As the Indian Ocean becomes a focal point for evolving regional tensions, the ability to counter submarine threats with high-speed, supercavitating torpedoes will strengthen India's naval defence. Such a system would not only act as a deterrent but also provide a technological edge, allowing the Indian Navy to respond swiftly and decisively to underwater threats.

1.3.2 Strategic Defence Priority and National Security

Researching and developing supercavitating torpedoes aligns with India's strategic defence priorities. Given the critical role naval forces play in protecting India's maritime interests, the addition of supercavitating torpedoes to the arsenal would significantly boost the nation's deterrence and combat capabilities. By pioneering indigenous technology in this field, India can reduce dependence on foreign defence imports and reinforce its national security posture.

1.3.3 Unique Research Opportunity

This PhD research presents a unique opportunity to contribute to both scientific knowledge and national defence. Supercavitation technology remains a relatively unexplored field in India, offering the chance to pioneer advancements that could reshape naval warfare. By focusing on this cutting-edge area, the research will not only address a critical defence need but also push the boundaries of engineering and fluid dynamics, laying the foundation for future innovations in underwater propulsion and high-speed manoeuvring systems.

This research is both a response to strategic defence challenges and an opportunity to contribute significantly to India's security and technological landscape.

1.4 Research Objectives:

The present research have the following objectives:

1. To develop empirical relations to predict the geometry of the elongated bubbles.
2. To design an efficient cavitator considering supercavitation size and overall drag for a high-speed heavyweight torpedo.
3. To computationally investigate the effect of temperature on supercavity geometry, particular to heat enhanced approach.
4. To test the strategy of installing a secondary cavitator to enhance supercavity size.

PART A
ELONGATED BUBBLE REGIME

Chapter 2

Multiphase Flow Dynamics of Elongated Bubbles

The study of elongated bubble formation and dynamics is highly relevant to the field of supercavitation, providing valuable insights into the behaviour of bubbles in fluid environments. The detailed observations on how elongated bubbles change shape during formation, rise, and coalescence can be directly applied to understanding how cavitation bubbles form and stabilize around objects. In supercavitation, maintaining a stable vapor cavity around a high-speed object is crucial to reduce drag. The present study provides a framework for predicting how elongated bubbles might behave under different flow conditions, which is essential for designing objects that can achieve and maintain supercavitation.

The scaling laws derived in this study, involving Reynolds number, Weber number, and Froude number, can be instrumental in modelling and predicting the behaviour of cavitation bubbles. These non-dimensional numbers help quantify the balance between inertial, gravitational, and surface tension forces, all of which are critical in supercavitation. By applying these scaling laws, the conditions under which supercavitation will occur and sustain can be better predicted. The study's insights into how fluid properties (like height above orifice and temperature) affect elongated bubble formation are valuable for optimizing the conditions needed for supercavitation. For instance, understanding how temperature influences bubble dynamics can lead to better control over the cavitation process, particularly in variable underwater environments. This could lead to improved designs for supercavitating vehicles that perform consistently under different thermal conditions.

The detailed understanding of bubble morphology under varying flow rates and orifice sizes can directly inform the design of high-speed underwater vehicles.

Supercavitating vehicles rely on creating and maintaining a vapor cavity to minimize drag. The research presented in this chapter can help in predicting how different flow conditions will affect the formation and stability of this cavity, leading to more efficient and effective designs. By applying the relationships established between various non-dimensional numbers, more accurate predictive models for supercavitation can be created. These models can be used to simulate different scenarios, optimize design parameters, and anticipate challenges in real-world applications.

In summary, the study of bubbles formation and coalescence provides a foundational understanding of bubble dynamics that is crucial for advancing supercavitation technology. The insights gained from this research can lead to better predictive models, optimized designs, and more effective control of supercavitation, ultimately contributing to innovations in high-speed underwater transportation and other related fields.

2.1 Experimental Methodology

2.1.1 Experimental Setup

The experimental setup for the present study consists of a transparent rectangular tank filled with quiescent liquid and fitted with a nozzle at the bottom of the tank for injecting compressed air as shown in Fig. 2.1. The tank is made up of plexiglass, with a cross-sectional area of 25 cm x 25 cm, and a depth of 40 cm. In our experiments, a maximum bubble diameter of 1 cm ensures that the wide cross-section area is large enough to cause a minimal 4% confinement effect of the wall. Fig. 2.2 shows the schematic diagram of the experimental setup.
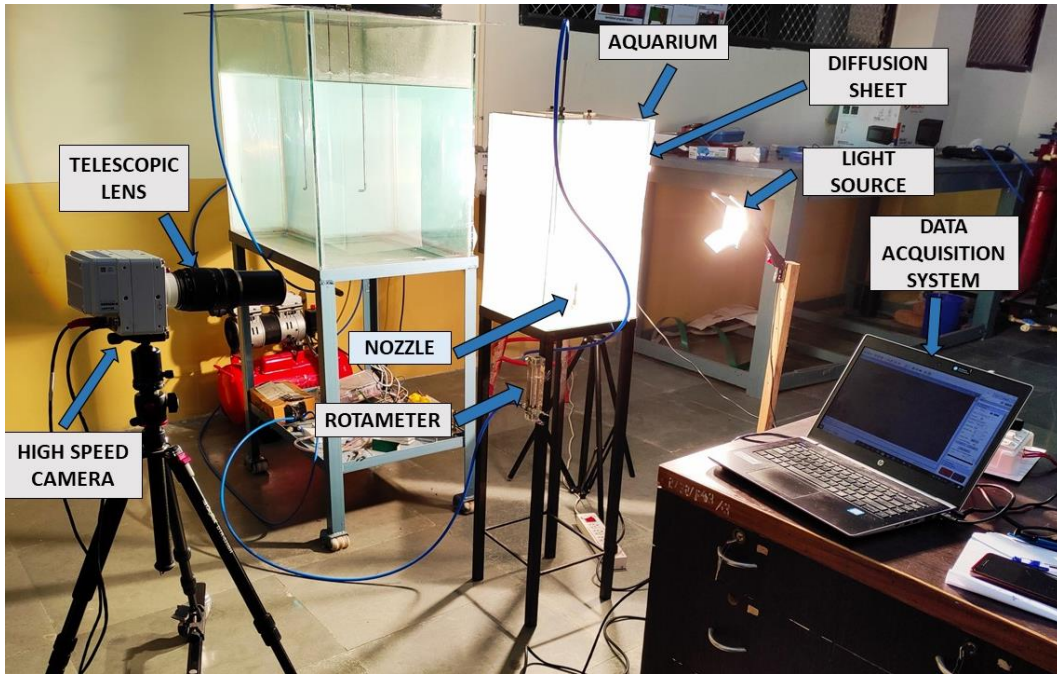
Fig. 2.1: The experimental setup used in the current study
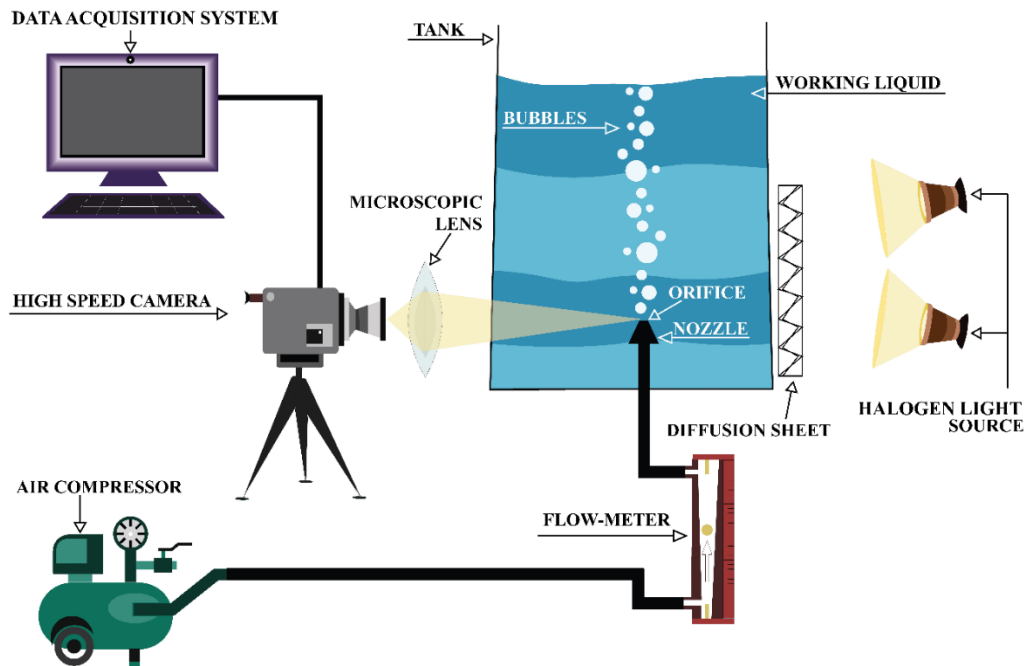
Fig. 2.2: Schematic diagram of the experimental setup used in the present study

2.1.2 Experimental/Test Parameters

The geometrical morphology of the bubble depends on the viscous force, surface tension force and pressure distribution inside the bubble. Therefore, to estimate the effect of all the forces, experiments have been done on various fluids at different mass flow rates, orifice diameters, and depths. The experiments were conducted on four different liquids i.e. water, acetone, 10% w/w glycerine water solution (Gly 10), and 20% w/w glycerin water solution (Gly 20). The properties of all the liquids are shown in Table 2.1:

Table 2.1: Properties of various liquids used in the present study

Fluid	Density (kg/m^3)	Viscosity $(mN.s/m^2)$	Surface tension (N/m)
Acetone	784.5	0.295	0.02308
Water	997	0.8891	0.07197
10% Glycerol solution (Gly 10)	1020.6	1.148	0.070639
20% Glycerol solution (Gly 20)	1045.2	1.5278	0.070208

The bubbles are generated by inserting compressed air into nozzles made up of brass with a circular orifice at the center of the top surface. Experiments are conducted using nozzles with an orifice diameter (d_o) of 0.4, 0.6, and 1 mm. To account for the effect of depth, the study is carried out at the fluid height (h) of 4, 8, and 12 cm above the nozzle orifice. The volume flow rate ($\dot{Q}$) of the compressed air is monitored and controlled using a flow meter, and the present experiments are conducted at 100, 200, and 300 ml per min.

The physical parameters in the present study are density (ρ) and viscosity (μ) of working liquid, the diameter of the orifice (d_o), gas flow rate ($\dot{Q}$), the height of liquid above orifice (h). The superficial gas velocity at the orifice (U_{gs}) can be calculated as $U_{gs} = 4\dot{Q}/\pi d_o^2$. The effective diameter (d_b) and aspect ratio (AR) of the bubble can be estimated as $d_b = \sqrt{L\,W}$ and $AR = L/W$ respectively, where L

and *W* are the length and width of the bubble. These physical parameters can be represented in terms of non-dimensional parameters such as Reynolds number, $Re = \rho U_{gs} d_b / \mu$; Weber number, $We = \rho U_{gs}^2 d_b / \sigma$; Froude number, $Fr = U_{gs} / \sqrt{gh}$ and Eotvos number, $Eo = \Delta \rho g d_b^2 / \sigma$, where σ is the surface tension between gas and liquid interface, *g* is the acceleration due to gravity and $\Delta \rho$ is the difference between gas and liquid densities.

2.1.3 High-Speed Image Processing

The images are captured at a frame rate of 5200 fps with a resolution of 1 megapixel using high-speed camera Phantom VEO 410. The camera is equipped with a telescopic lens of variable focal length in the range of 18-36 cm to capture the zoomed-in view of the bubble. To enhance the image quality, the light is intensified using two halogen lamps placed on the other side of the camera. A diffuser sheet is used to distribute the light uniformly inside the tank. The video stream data from the camera is collected on a computer using Phantom software. The images are processed to extract the bubble dimensions using the Digital Image Processing Toolbox in MATLAB using a script that has been described by previous authors. The script converts the raw image captured from high-speed cinematography into binary image to detect the bubble shape (Fig. 2.3). Bounding box algorithm is applied on the detected bubble shape to calculate bubbles length (*L*), width (*W*) and aspect ratio (*AR*) as shown in Fig. 2.4. This method of detection of bubble parameters has been extensively used by researchers in the past. The dimension is averaged over at least five to ten consecutive bubbles for each case.

a) Raw image	b) Binarized image

c) Complemented image	d) Detected bubble shape
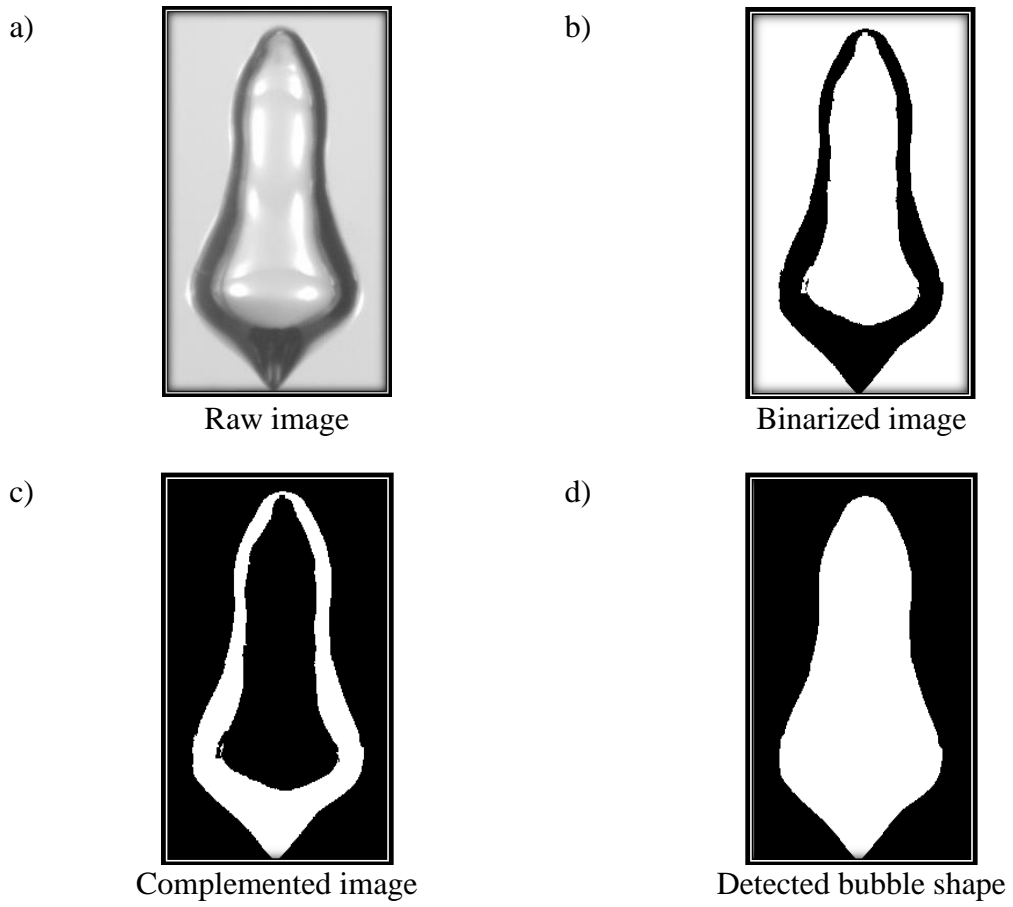
Fig. 2.3: Detection of bubble geometry from raw high-speed images
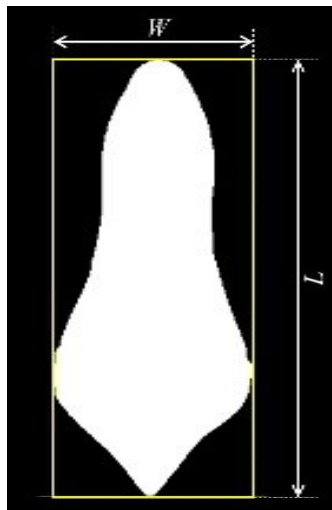
Fig. 2.4: Evaluation of bubble length (L) and width (W) using the bounding box algorithm

17

2.1.4 Uncertainty Analysis

The flow meter was calibrated before the conduction of experiments and the uncertainty in the measurement of superficial gas velocity, U_{gs} is approximately 5.6%. The nozzle orifice diameter has a maximum uncertainty of less than 0.3%. The fluid properties like density and viscosity are calculated based on the temperature which was measured with an accuracy of $\pm$ 0.1 °C. The depth of the orifice is measured using a metric scale with a least count of 1 mm. Finally, in the present study, the maximum uncertainty in the calculation of, $\hat{d}$, Re, Fr and Eo are estimated to be 1.6%, 6.9 %, 6.2% and 2.7 % respectively.

2.2 Results and Discussion

2.2.1 Qualitative Results

In such a scenario where bubbles are produced from submerged upward orifice in a quiescent fluid, both propulsive and resistive forces act on the bubbles in the upward and downward directions, respectively. The pressure force (given by Young-Laplace equation as $F_p = \pi d_o^2 \sigma / 4 d_b - \pi d_o^2 d_b \rho g / 4$), buoyancy force ($F_b = \pi d_b^3 g \Delta \rho / 6$) and the gas momentum force ($F_M = 4 \rho Q^2 / \pi d_o^2$), whereas the resistive forces are the viscous drag force ($F_D = -\pi d_b^2 C_D \rho / 8 \left(dY / dt \right)^2$), the liquid inertia force ($F_I = d(m_v U) / dt$), and the surface tension force ($F_s = \pi \sigma d_o \sin\theta$). In the above expressions, θ denote the contact angle between the bubble and the nozzle, m_v represents the added mass which is typically given as 11/16 times the product of bubble volume and the liquid density, U is the bubble rise velocity, Y is the vertical location of center of mass of the bubble and C_D is the drag coefficient of the bubble.

2.2.1.1 Morphology during bubble rise

Figure 5 shows the morphology of bubbles at the onset of their rise before it pinches off the nozzle. Initially, at a time duration of 6.15 ms, the shape of the

bubbles are governed by a quasi-static balance between the surface tension and upward buoyant forces. The bubbles forming in the liquid initially take a conical shape as shown in Fig. 2.5a. This is due to the high centerline gas momentum that causes axial elongation of the bubble. The propulsive forces are greater than the resisting forces, and the bubble undergoes an unstable condition in which both the growth of the bubble and its upward motion can be seen. The stretching in the central portion continues with time, leading to a flame-like shape, while the bubble is attached to the nozzle tip via a capillary neck (Fig. 2.5b). Further stretching causes the bubble to pinch off from the nozzle tip and the bubble starts to rise (Fig. 2.5c). This motion is caused by a rapid upward movement of the capillary neck due to the surface tension force after the bubble detachment. The bubble volume is controlled by the pressure level inside the bubble and the one inside the gas reservoir. Just after the pinch-off, a series of waves is observed on the surface of the bubble. These waves travel from the bottom toward the top of the bubble and flatten the bottom surface. As the bubble ascends, the tip of the bubble blunts due to the viscous effects at the air-water interface, hence lending a bullet-like shape to the bubble (Fig. 2.5d). This continued frictional effect further blunts the bubble tip and hence morphs it into a wavy hemispherical shape like a spherical cap bubble. (Fig. 2.5e). On further rising, the formation of a concave dimple on the bottom surface is observed (Fig. 2.5f). As the bubble rises further, another series of Kelvin-Helmholtz waves are observed on the bubble surface, but traveling from the top to the bottom surface, making a broad cross-section at the top, this provides the bubble shape of an inverted cone (Fig. 2.5g). The bubble oscillations continue, and the resulting viscous dissipation further flattens the bubble giving it a disk-like shape. (Fig. 2.5h), which continues to be dominated by the process of wave formation (Fig. 2.5i).

a) $t = 6.15$ ms

b) $t = 16.34$ ms

c) $t = 19.23$ ms

d) $t = 24.81$ ms

e) $t = 33.27$ ms

f) $t = 40.58$ ms

g) $t = 65.58$ ms

h) $t = 76.35$ ms

i) $t = 90.96$ ms
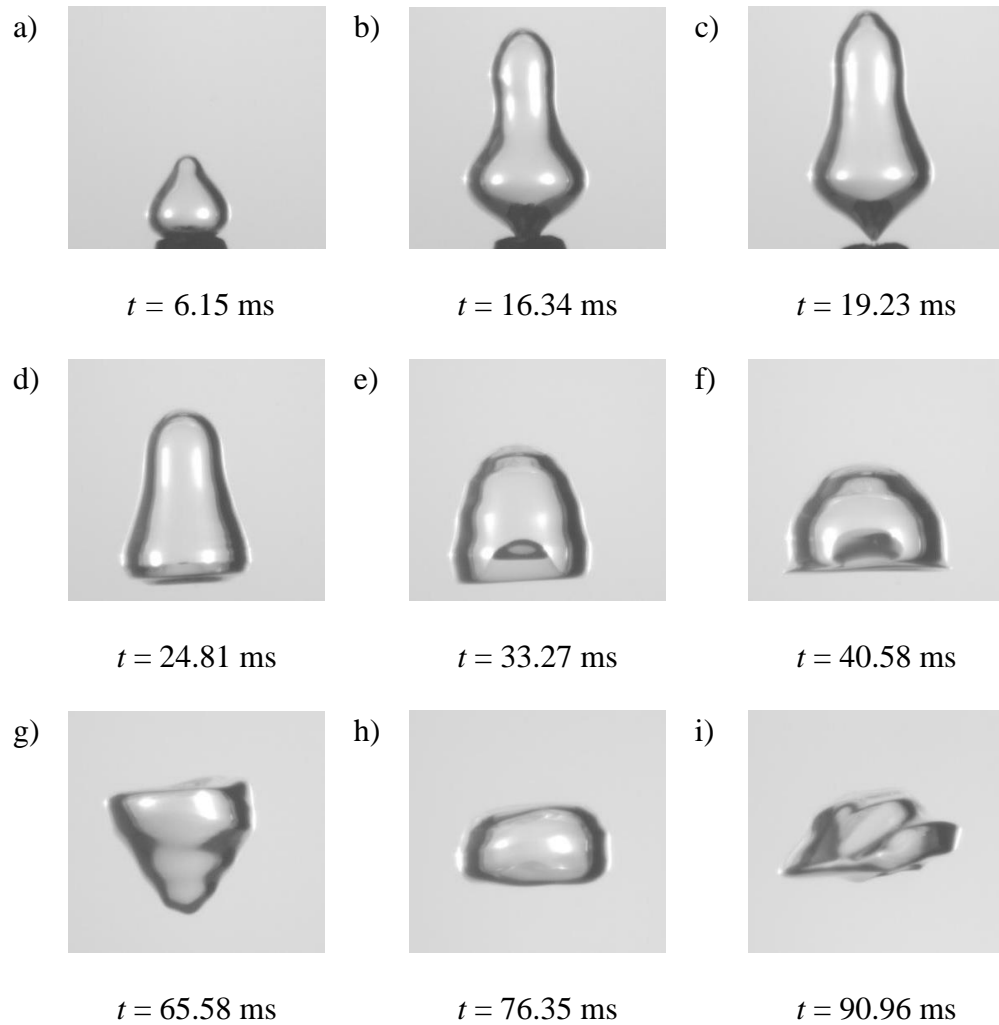
Fig. 2.5: Bubble geometry and morphology during rising at different time intervals (t). Similar morphology of bubble was observed for all the cases.

For small bubbles, surface tension forces are quite predominant, and the pressure difference is inversely proportional to the bubble radius. Since the pressure gradients travel at the speed of sound in the gas phase, the pressure inside a small bubble is expected to be almost uniform. Because of the large pressure difference, the small bubbles possess perfect spherical symmetry and are not influenced by external disturbances. This is not the case with the large bubbles, where surface tension forces are no longer dominant. Consequently, the large bubbles are more susceptible to external fluctuations in the flow and are governed by buoyancy and inertia forces.

2.2.1.2 Bubble coalescence morphology

The morphology of ejection of the leading bubble is similar to in the case of a single bubble where it took a conical shape initially followed by a centrally elongated shape. As soon as the leading bubble pinches off, a trailing bubble interface starts to form, which influences the shape of the leading bubble. The initial shape of the trailing bubble is oval, and it interacts and flattens with the lower part of the leading bubble (Fig. 2.6a). Due to the low-pressure wake formed behind the leading bubble, the trailing bubble encounters lower drag forces and hence attains a higher velocity and is more elongated than the leading bubble (Fig. 2.6b). The trailing bubble strikes the flattened lower surface of the leading bubble and creates a concave dimple on it (Fig. 2.6c). With the passage of time, the leading bubble morphs into a disk shape whereas the trailing bubble turns to an almost spherical shape due to the action of viscous forces (Fig. 2.6d). The trailing bubble starts coalescing into the leading bubble, forming a neck connecting both the bubbles. The neck formation is associated with the formation of two sets of waves, one moves upward into the leading bubble while the other travels downwards into the trailing bubble (Fig. 2.6e). The air from the trailing bubble then passes to the leading bubble through the connecting neck due to the buoyancy effect, creating a reverse truncated shape of the coalesced bubble (Fig. 2.6f). A couple of jets are formed from the upper and lower surface, the jet from the bottom surface is thinner and longer than that of the upper surface (Fig. 2.6g). The collision of the jet emerges from the bottom surface, into the upper surface, creating multiple strong surface waves. This water jet forces the upper surface to move faster than the bubble velocity, thus creating a sharp leading edge and morphs the coalesced bubble into a wavy conical shape (Fig. 2.6h). Further action of friction forces increases the bluntness of the bubble, providing it the shape of a wavy disk (Fig. 2.6i).
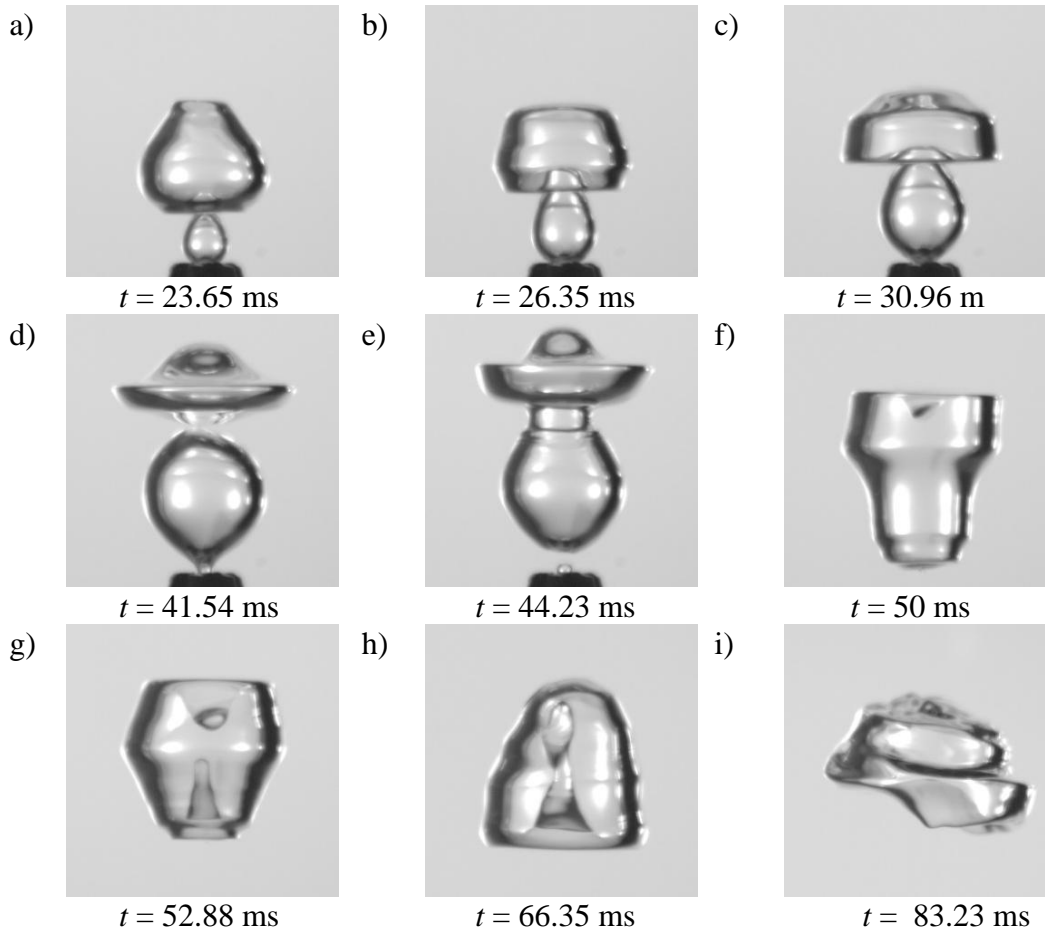
Fig. 2.6: Bubble coalescence morphology at different time instances. Similar pattern of coalescence was observed for all the cases.

2.2.2 Quantitative Results

For quantitative analysis of bubble formation, the experimental images at various time intervals are extracted from high-speed cinematography. The images are processed using an in-house developed MATLAB algorithm to extract bubbles' geometrical parameters. Assuming the bubble to be an ellipse, the minor and major axis diameter of the bubble are estimated using a bounding box algorithm. The diameter of the bubble is then computed by taking the geometric mean of the minor and major diameters. This methodology is applied to estimate the diameter of at least five to ten consecutive bubbles for each case. The average of these diameters is considered as the final diameter of the bubble for that case. This diameter is used to calculate forces on the bubble in terms of non-dimensional numbers.

The dynamics of elongated bubble formation are driven primarily by viscous force, buoyancy, surface tension, inertial force and thus can be recast in terms of non-dimensional parameters. Reynolds number plays an important role in the bubble shape during formation by accounting for the ratio of inertial and viscous forces. Since the surface tension plays a crucial role in the bubble formation process, the Weber number is also taken into account. The gravitational and buoyancy force stretches the bubble and alters its aspect ratio. These effects are taken into account by monitoring the Froude number and Eotvos number. The non-dimensional numbers are determined for each case and are plotted against each other to find out a scaling relation between them. These relations can be helpful in the prediction of bubble geometry during formation.

2.2.2.1 Effect of gas superficial velocity on bubble geometry

The gas superficial velocity has a significant impact on the bubble length. The gas superficial velocity can be increased either by increasing the volume flow rate of the gas or by decreasing the orifice diameter. At a constant orifice diameter, any rise in volume flow rate results in a proportional rise in the gas superficial velocity which further causes an elongation of the bubble as shown in Fig. 2.7a. However, the variation in width is relatively negligible and thus an augmentation in the bubble aspect ratio is observed. However, at a fixed volume flow rate, the gas superficial velocity shows an increment upon a reduction in the orifice diameter. In such cases, the bubble length reduces with an enhancement in the gas superficial velocity. Fig. 2.7b shows the increase in bubble diameter with decrease in gas superficial velocity, which in turn can be attributed to the increase in orifice diameter. However, the width almost remains constant, consequently, a decrease in aspect ratio is also observed.

a)

| $U_{gs} = 2.12$ m/s | $U_{gs} = 4.24$ m/s | $U_{gs} = 6.36$ m/s |

b)

| $U_{gs} = 13.270$ | $U_{gs} = 5.898$ | $U_{gs} = 2.123$ |
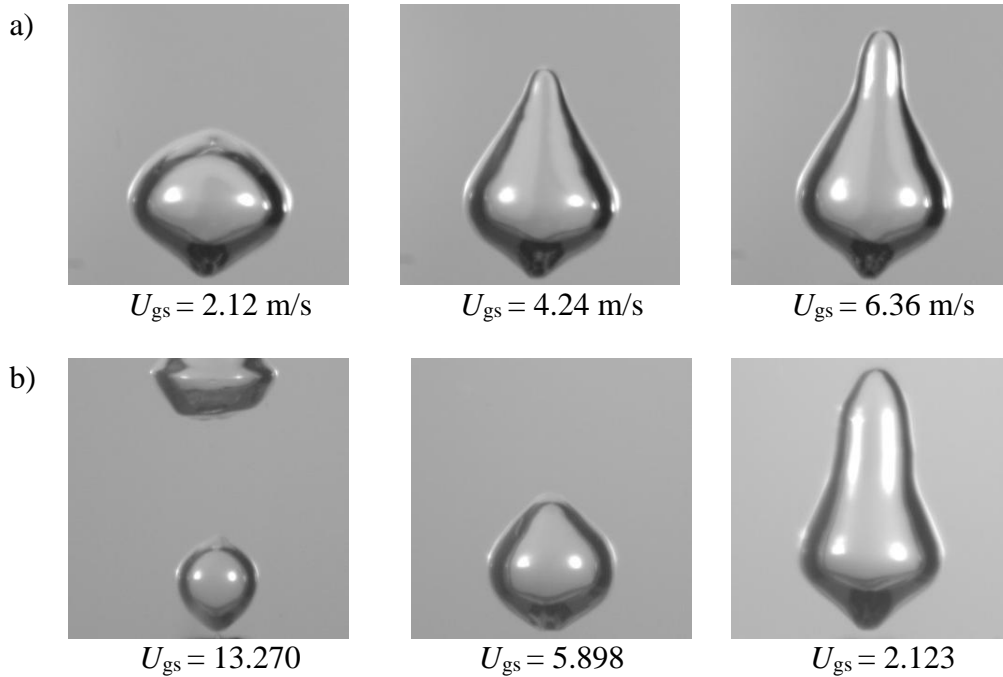
Fig. 2.7: Bubble geometrical changes due to change in gas superficial velocity through (a) increasing flow rate, (b) increasing orifice diameter. Note that the velocity changes in part (b) simply correspond to the increasing orifice area of the nozzle.

Figure Fig. 2.8 illustrates the dependence of bubble height as well as the bubble aspect ratio on the orifice diameter, or alternatively, the gas superficial velocity. For all the liquids used in our experiments, the bubble size is noted to increase as the orifice diameter is increased. In accordance with the continuity principle, this can alternatively be stated as the inverse dependence of the bubble size upon the gas superficial velocity. At an orifice diameter of 0.4 µm, the bubble sizes lie in the range of 5-6 mm, at an orifice diameter of 0.6 µm, in the range of 8-9 mm, and finally bubble sizes of approximately 12 mm are obtained for an orifice diameter of 1 µm. Conversely, a decreasing trend is observed with respect to aspect ratio: at a smaller orifice size of 0.4 µm, a near spherical bubble with a mean aspect ratio around 1.25 is obtained. This mean aspect ratio increases to 1.55 and 1.8, for orifice sizes of 0.6 µm and 1 µm, respectively.
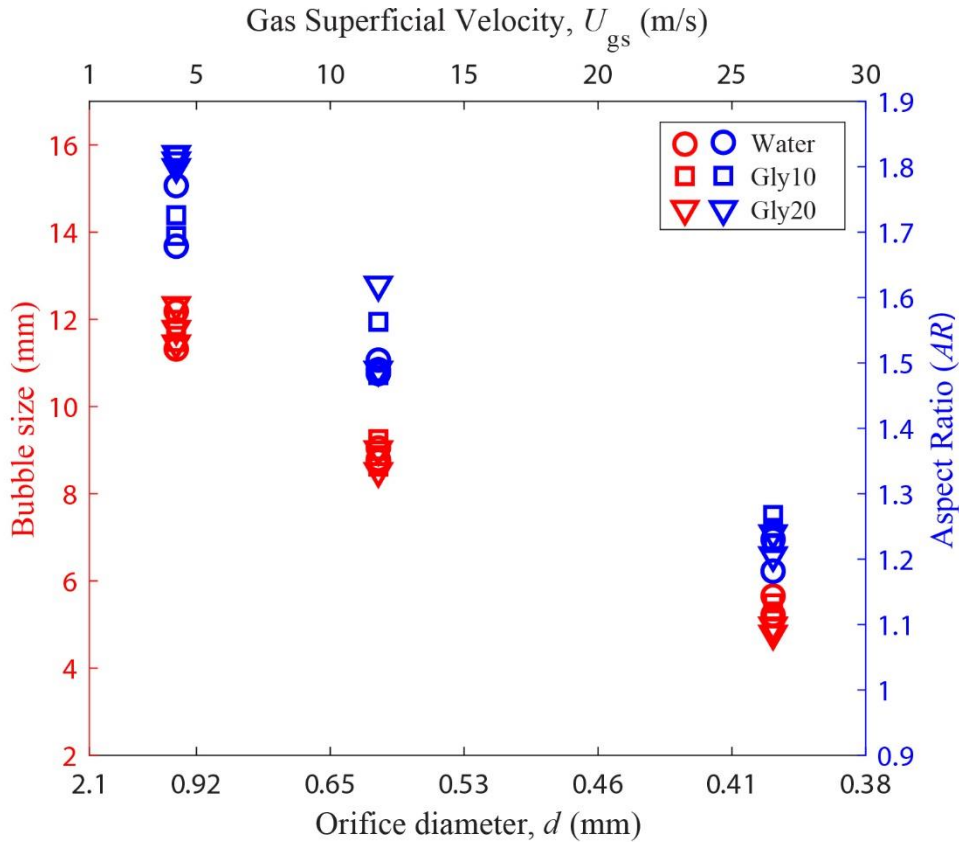
Fig. 2.8: Effect of variation in the bubble height (in red), and bubble aspect ratio (in blue) with the orifice diameter or its corresponding superficial gas velocity (shown on the top horizontal axis).

2.2.2.2 Effect of fluid depth on bubble geometry

The effect of fluid depth on bubble geometry varies with respect to experimental conditions, most noticeably on the orifice diameter. For the larger orifice diameter, the bubble size decreases with an increase in orifice depth as shown in Fig. 2.9b. However, for lower orifice diameter, the effect diminishes, and almost equal size bubbles are formed at all fluid depths as shown in Fig. 2.9a. However, the bubble width is almost unaffected by the liquid depth. Consequently, the aspect ratio also follows the same trend as the length of the bubble. Fig. 2.9 also shows that for constant volume flow rate at a specific depth, the length and hence

volume of the bubble is greater for larger orifice diameter. Therefore, the frequency of bubble formation is lower in the case of higher orifice diameter.

a)

| $h = 4$ cm | $h = 8$ cm | $h = 12$ cm |

b)

| $h = 4$ cm | $h = 8$ cm | $h = 12$ cm |
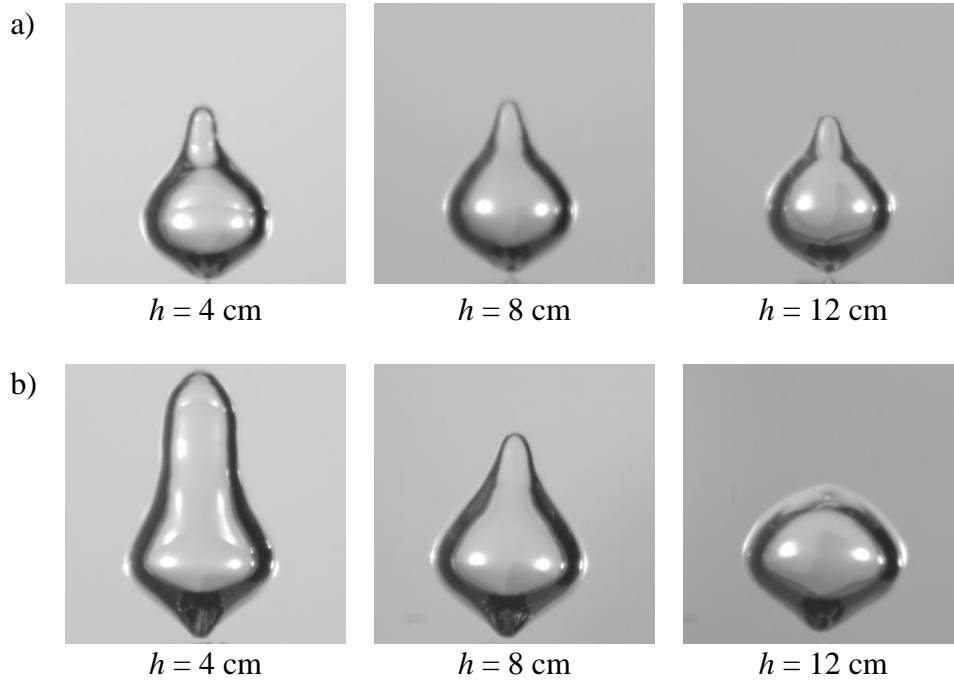
Fig. 2.9: Effect of depth on bubble geometry at orifice diameter of (a) 0.6 mm and (b) 1 mm

As seen above, the aspect ratio of the bubble depends on the orifice diameter and the depth of the orifice. To further explore this variation, a non-dimensional number $\hat{d}$ is defined as $\hat{d} = \frac{d_o}{h} * 10^3$. The aspect ratio of the bubble is plotted against $\hat{d}$ and is shown in Fig. 2.10. At a particular $\hat{d}$, the data collected for all the cases are denoted by employing the vertical error bars, and later the mean value at each $\hat{d}$ is joined using a dashed line, suggesting a preliminary trend in the variation of *AR*. It can be clearly inferred that the mean value of aspect ratio increases almost linearly with increase in $\hat{d}$.
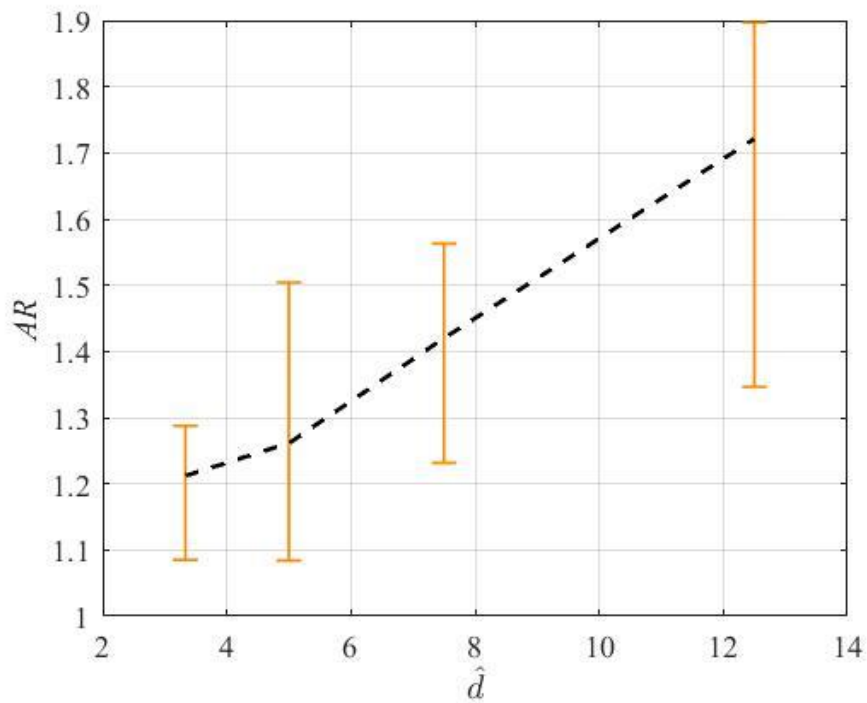
Fig. 2.10: Variation of mean bubble aspect ratio with non-dimensional parameter $\hat{d}$. The vertical bars don't represent the standard deviation in the measurement of data. Rather, it is the range of AR that is observed across all cases at a particular value of $\hat{d}$.

2.2.2.3 Effect of fluid properties on bubble geometry

The bubble formed in the acetone medium is the smallest and has an oval shape with pointed ends as shown in Fig. 2.11a. Due to the small volume of bubbles, the frequency of bubble generation is greatest in acetone. In most cases of acetone, it is observed that as soon as the leading bubble detaches, multiple small trailing bubbles erupt and strike the trailing bubble which then bounced back without coalescence. For a few cases, such as at an orifice diameter of 1 mm and a flow rate of 100 ml per min, single bubbling is observed. In chaotic bubbling, there is a significant difference in the geometry of bubbles, therefore these cases are omitted from the scaling law analysis. In water, a nearly spherical-shaped bubble is formed with a diameter that is approximately equal to the length of bubbles in acetone at

27

the same experimental conditions (Fig. 2.11b). In both Water-Glycerine solutions, a highly elongated bubble is formed with a size quite larger than in the case of water and acetone as shown in Fig. 2.11c and Fig. 2.11d. The longest bubble is observed in Gly 10. It is also found out that the dependence of the geometry of the bubble can't be extricated with respect to the density or viscosity of the liquid, rather it depends on all the fluid properties. Therefore, to suitably understand and predict the variation of bubble geometry with the fluid properties, a detailed study is presented in the following sections.
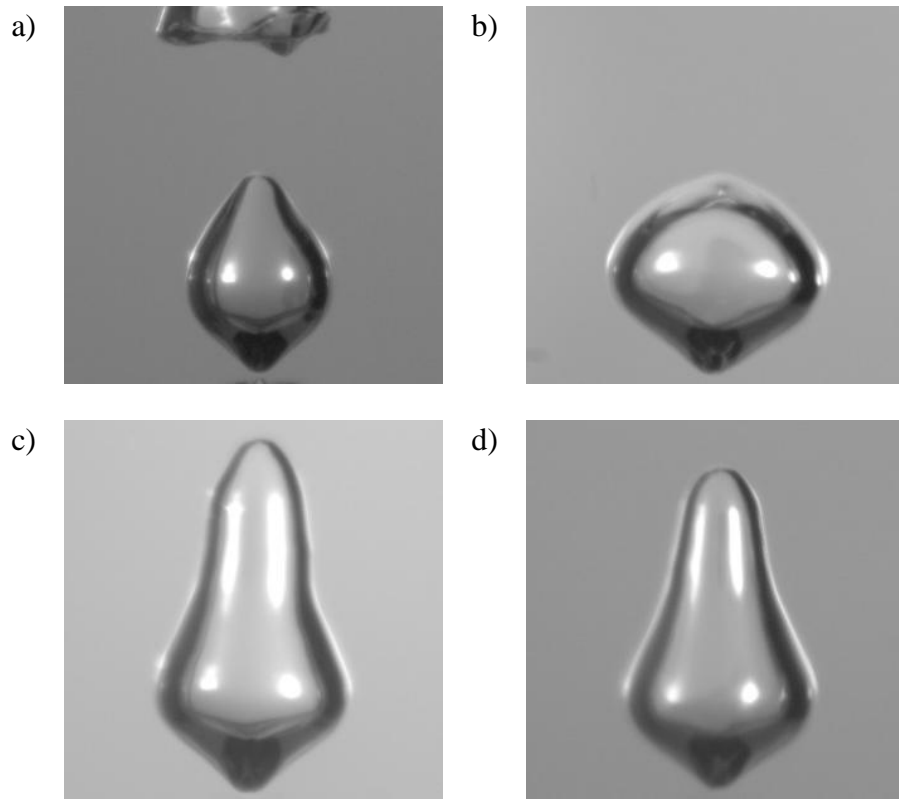
Fig. 2.11: Bubble geometry just after pinch-off in various liquids (a) Acetone, (b) Water, (c) Gly 10, (d) Gly 20

2.2.2.4 The inter-relationships between inertia, surface tension and viscous forces: *Re-We* scaling

Surface tension tries to keep the bubble in a more stable form whereas the viscous effect tries to flatten the bubble. Therefore, the final shape of the bubble during the formation process critically depends on the balance between these two forces. To quantify this effect, Reynolds number and Weber number are estimated based on bubble geometry just after the pinch-off. The Reynold number varied over the range of 16,000 – 155,000, whereas the weber number varied from 430 to 51,500. The values are plotted against each other to derive a scaling law between Reynolds number and Weber number, which can predict the effect of viscous and surface tension forces on bubble formation geometry as shown in Fig. 2.12.
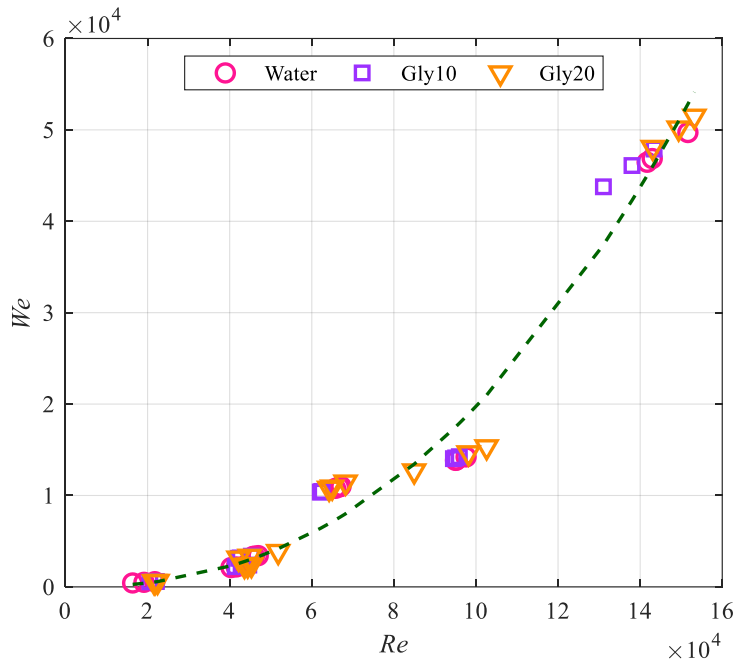
Fig. 2.12: Reynolds number and Weber number relation for bubbles just after pinch-off. Curve fitting RMSE value = 2557, R squared value: 0.976

The figure clearly shows that the Reynolds number and Weber number follow a parabolic law i.e. on increasing the Reynolds number, the Weber number increases slightly higher than the square of the Reynolds number. The increase in Reynolds number is associated with either an increase in inertial force or a decrease

in viscous force. The Weber number is also directly proportional to the inertial force; hence, it increases with an increment in Reynolds number. Put simply, when the inertial forces are predominant over the viscous forces (at high Re), in such a scenario, the weak surface tension forces are also susceptible to being overpowered by it. The exact dependence is found out by regression analysis as,

$$We = 2.98 * 10^8 * Re^{2.364} \qquad\qquad ….. \text{Eqn. (2.1)}$$

This relation quantifies the cumulative effect of injection parameters such as orifice diameter and gas flow rate and fluid properties on the bubble size.

2.2.2.5 The inter-relationships between inertial, viscous, and gravitational forces: *Re-Fr* scaling

Gravity also plays an important role in the determination of geometrical characteristics of bubbles during their formation. The effect of gravity can be considered by including the Froude number in this scaling analysis, since it is the measure of the ratio of inertial and gravitational forces. Figure Fig. 2.13 shows the plot between the Froude number and the Reynolds number. The nature of this dependence may yield crucial insight into the determination of the bubble velocity and length. As per Fig. 2.13, there is an almost linear relation between Froude and Reynolds number.

$$Fr = 2.67 * 10^{-6} * Re^{1.368} + 0.854 \qquad\qquad …….\text{Eqn. (2.2)}$$

It is evident from the relation that an increase in Reynolds number consequently also increases the Froude number. This is because an increase in the inertial forces increases the bubble size which results in a higher gravitational force on the bubble that increases both Reynolds number and Froude number. On the contrary, an increment in the viscous forces leads to greater shearing forces or smaller size bubbles are which are characterized by lesser magnitude of gravitational forces and hence a smaller Froude number. The variability in Fr for the same Re is primarily due to the dependence of Fr on other factors, including fluid depth and buoyancy

forces, which can lead to slight variations even when Re is constant. This effect becomes more pronounced at higher Re values, where increased inertial forces cause the formation of elongated bubbles. These bubbles experience greater buoyancy forces, resulting in larger variability in Fr.
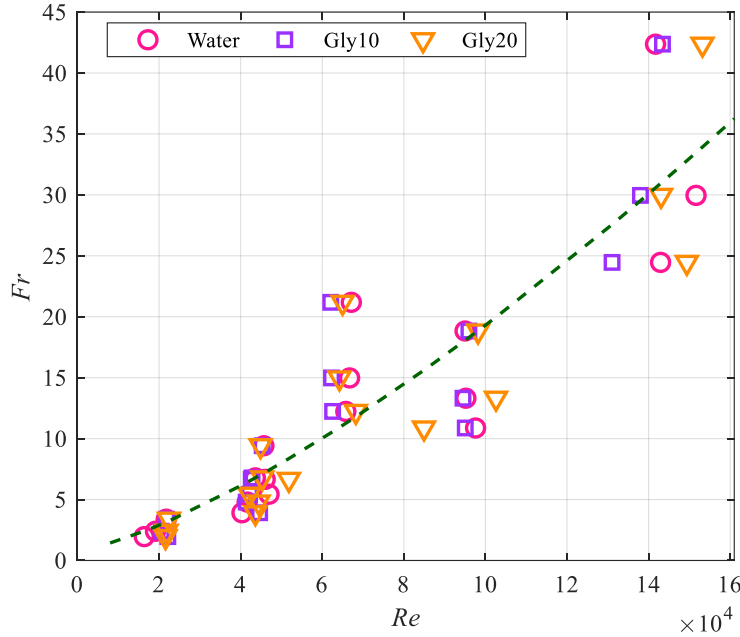
Fig. 2.13: Reynold number and Froude number relation for bubble just after pinch-off. Curve fitting RMSE value = 4.69, R-squared value: 0.815

2.2.2.6 The inter-relationships between the relevant forces: A new scaling law.

It is clear from the previous graphs that the *Re*, *We*, and *Fr* have a prominent effect on the bubble geometry during the formation process. However, the *Re-We* relation underscores the effect of Viscous and surface tension forces only. On the other hand, *Re – Fr* relationship highlights the effects of viscosity and gravity. It can also be clearly observed that the scaling law between Froude number and Reynolds number is rather discrepant with a smaller R-squared value equaling 0.815. This suggests the need for a better scaling law that can accurately capture

31

the physics of the formation process. Such a scaling law must incorporate the aggregate effects of the inertial force, viscous force, surface tension, and gravitational force. In order to explore such a scaling law, the ratio of *We* to *Fr* is plotted against *Re,* and shown in Fig. 2.14.
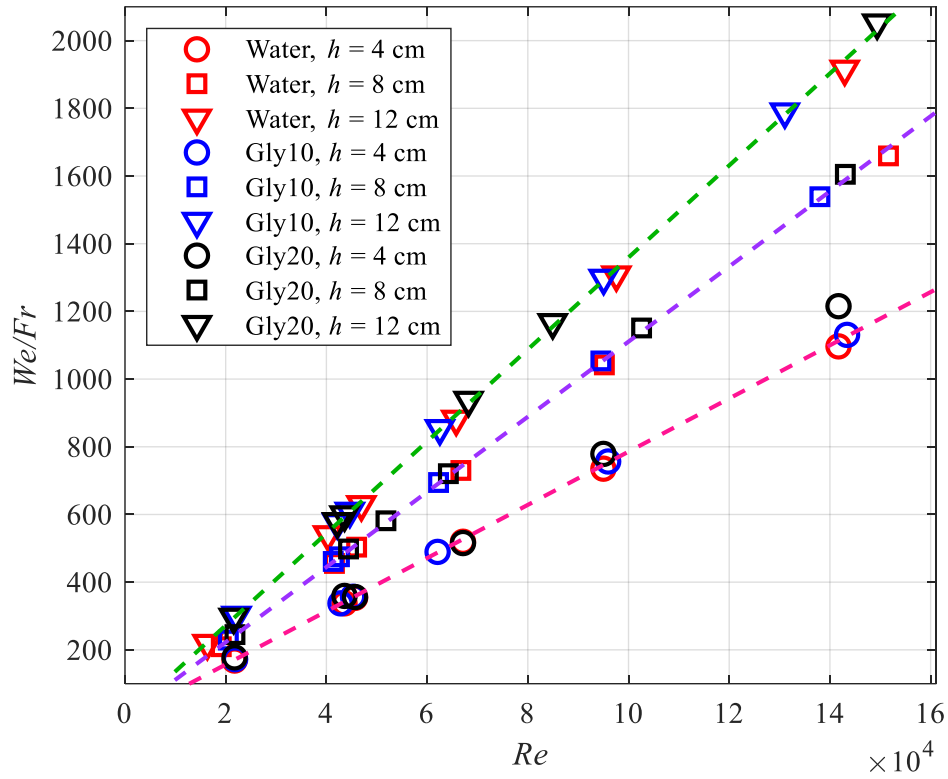
Fig. 2.14: Variation in ratio of Weber to Froude number with Reynold number. Curve fitting details: (a) h = 4cm: RMSE = 7.07, R squared = 0.999, (b) h = 8cm: RMSE = 10.14, R squared = 0.999, (c) h = 12cm: RMSE = 12.09, R squared = 0.999

When the results are plotted in such a fashion, interestingly the data corresponding to all three fluids converge on one single straight line, with a very precise value of R-square greater than 0.999. It is evident from Fig. 2.14 that there are three different lines of varying slopes, and each line represents a particular depth of bubble formation. A scaling law shows that the *Re* is linearly proportional to the *We/Fr* and can be expressed as $We/Fr = m * Re + c$, and the slope of the line(*m*)

32

depends on the depth of the orifice from the surface of the water. All the regression coefficients for different heights are shown in Table 2.2 that shows the slope of the line (m) increases as the liquid height (h) increases. A relation has also been derived between depth of orifice (h) and the slope of the line (m) as shown below:

$$m = 0.06925h + 0.005247 \qquad \text{.....Eqn. (2.3)}$$

Table 2.2: Regression coefficients for different heights

Depth of orifice	Regression coefficients	
h	m	c
0.04 m	0.00786	-0.4826
0.08 m	0.0111	0.6193
0.12 m	0.0134	0.3954

2.2.2.7 The inter-relationship between Reynolds number and Eotvos number.

The buoyancy force is also crucial in bubble rise velocity and hence bubble length. To account for the buoyancy effect, the Eotvos number is also estimated and analyzed. The Eotvos number is plotted against Reynolds number, to quantify the combined effect of inertial, viscous, buoyancy, and surface tension force. It is found that the Eotvos number is directly proportional to the Reynolds number as shown in Fig. 2.15.

It can be depicted that higher inertial forces resulted in the formation of larger bubbles that possess a higher force of buoyancy than the smaller bubbles. Therefore, an increase in Reynolds number also increases the value of the Eotvos number. Again, by fitting a curve to the experimental data shows that the relation can be expressed as $Eo = m * Re + c$. However, the value of m and c depends on the gas superficial velocity and is tabulated in Table 2.3. For higher gas superficial velocities, the value of m is lower i.e. increment in Reynolds number gradually increases Eotvos number, due to decrease in inertial force and vice versa.
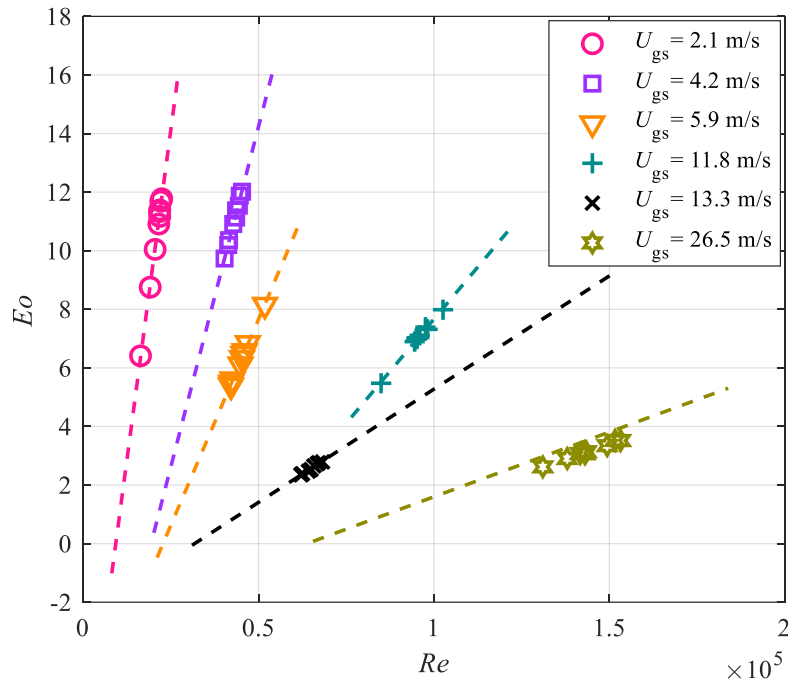
Fig. 2.15: Reynold number and Eotvos number relation for bubbles just after pinch-off

It may also be concluded that at higher gas superficial velocity, the gravitational and viscous forces are dominant, whereas at low gas superficial velocity the bubble formation phenomenon is surface tension driven. Further, another interconnecting relation between the regression coefficients and the gas superficial velocity has been derived using interpolation method as

$$m = 2.5 * 10^{-3} * U_{gs}^{-1.25} \qquad\qquad \text{…….. Eqn. (2.4)}$$

Table 2.3: Regression coefficients for different gas superficial velocity

Gas superficial velocity	Regression coefficients	
U_{gs}	m	c
2.1 m/s	9×10^{-4}	- 8.377
4.2 m/s	4.65×10^{-4}	-9
5.9 m/s	2.81×10^{-4}	-6.408
11.8 m/s	1.42×10^{-4}	-6.566
13.3 m/s	7.73×10^{-5}	-2.455
26.5 m/s	4.15×10^{-5}	-2.819

2.3 Significance of the findings:

The current paper reports the geometrical morphology of bubbles during formation, rising, and coalescence in different fluids at three different orifice sizes. Each orifice is provided with a range of mass flow rates at different heights. We have also studied the effect of these parameters explicitly on the geometry of bubbles during the formation. These parameters are then expressed in form of non-dimensional numbers such as Reynolds number, Weber number, Froude number, and Eotvos number. Simple scaling law is derived between Reynolds number and other non-dimensional parameters to quantify the influence of various forces on the bubble geometry. The scaling law can effectively predict the bubble geometry for a given set of experimental conditions. The major findings of the current manuscript can be summarized as follows:

- During the rising process, the shape of the bubble changes from an elongated cone to a bullet, to a hemisphere, and then to an inverted cone and finally a disk. A concave dimple is observed on the bottom of the bullet and hemispherical shape. A series of surface waves traveling from bottom to top is observed during pinch off which makes the surface of the bubble wavy and later causes the bubble to take an inverted cone shape.

- The leading bubble emerged similar to a single bubble initially followed by the formation of a trailing bubble. Both the bubbles interfere and thus affect each other's geometry. The trailing bubble is faster and becomes more elongated due to the wake of the leading bubble whereas a dimple is imprinted by the trailing bubble on the bottom surface of the leading bubble. A neck is formed at the contact point of the bubbles during coalescence. The neck formation is associated with the formation of two sets of waves, one set traveling upward into the leading bubble and the other down into the trailing bubble. Just after the coalescence, a couple of jets are also observed from the bottom and top surface of the coalesced bubble.

- The bubble length and aspect ratio during formation increases with an increase in gas flow rate, and decrease in orifice diameter. The effect of

35

fluid height on bubble length and aspect ratio depends on the orifice size. For larger orifice size (1 mm diameter), the bubble length increases with a decrease in fluid height above orifice, for smaller orifice (0.6 and 0.4 mm diameter) the bubble length is almost constant for all fluid height.

- The shape of the bubble depends on the relative magnitudes of viscous force, surface tension force and forces due to pressure distribution, and therefore a relation between weber number and Reynolds number is established. It is found that Weber number is directly proportional to the square of Reynolds number and can be estimated as $We = 2.98 * 10^8 * Re^{2.364}$.

- To account for the effect of gravity on bubble geometry, the scaling law between Froude number and Reynold number is found as $Fr = 2.67 * 10^{-6} * Re^{1.368} + 0.854$. Based on the scaling law, it is concluded that for a lower value of inertial forces, the bubble geometry is dependent majorly on gravitational forces than viscous forces. As the inertial force rises, the viscous force starts to dominate the bubble geometry than gravitational forces.

- It is found that the ratio of Weber number to Froude number has a linear relation with Reynold number and can be expressed in as $We/Fr = m * Re + c$. However, the slope of the curve depends on the height of fluid above the orifice and can be estimated by using the relation $m = 0.06925h + 0.005247$

- The Eotvos number depends linearly on the Reynolds number, and the slope of the Re-Eo curve is inversely proportional to the gas superficial velocity. The slope of the Re-Eo curve can be estimated as $m = 2.5 * 10^{-3} * U_{gs}^{-1.25}$

- The liquid temperature also affects the bubble formation morphology and therefore the effect of liquid temperature on the proposed scaling law can also be investigated in future studies.

PART B
SUPERCAVITATION REGIME

Chapter 3

Performance Evaluation of Various Cavitator Shapes

3.1 Introduction

Cavitators— specifically designed devices placed at the front of the underwater vehicle—are instrumental in inducing supercavitation. These cavitators come in various shapes, each contributing differently to the supercavitation dynamics. The geometrical configuration of a cavitator directly influences its ability to generate a supercavity, the size of which is critical in minimizing drag. A larger supercavity reduces the skin friction drag but increases pressure drag, which necessitates a delicate balance in cavitator design to optimize overall vehicle performance. This chapter focuses on the performance comparison of different cavitator shapes to identify the optimal design that balances supercavity size and drag forces. By employing a range of simulations, the study evaluates cavitators in terms of their ability to reduce skin friction drag, taking into account the various cavitation numbers at which these devices operate. This chapter emphasizes that the ideal cavitator must generate a supercavity just large enough to encompass the vehicle without unnecessarily increasing pressure drag, a key factor in high-speed underwater travel. This comprehensive assessment provides insights into how cavitator design impacts the effectiveness of supercavitation, offering valuable information for future applications in naval and industrial settings. Next, we begin with the description of various geometries of cavitators used in our study.

3.1.1 Geometry

A survey of numerous heavy-weight torpedoes is conducted to select the torpedo's geometry for the present study. Majority of the torpedoes are considered from India, Russia, UK, and USA. The torpedo design employed in the current

study has a length of 8 metres and a diameter of 800 millimetres. The equation for designing the torpedo for minimum drag is derived by Myring (Myring, 1976). The equation for designing nose and tail of the torpedo is shown in Eqn. (3.1) and (3.2) respectively. The main body of the torpedo is considered to be of cylindrical shape. In the present study same approach is used to design the torpedo.

$$y_n = \frac{1}{2}d\left[1 - \left(\frac{x-a}{a}\right)^2\right]^{1/n} \qquad\qquad\qquad \dots\dots\text{Eqn. (3.1)}$$

$$y_t = \frac{1}{2}d - \left(\frac{3d}{2c^2} - \frac{tan\theta}{c}\right)(x - a - b)^2 + \left(\frac{d}{c^3} - \frac{tan\theta}{c^2}\right)(x - a - b)^3 \dots\text{Eqn. (3.2)}$$

where y_n and y_t are y locations of nose and tail curve respectively, a, b and c are the length of the nose, main body and tail of the torpedo respectively, d is the maximum diameter of the torpedo, θ is the half-angle made by the tail as illustrated in Fig. 3.1. The bluntness of the nose is governed by the variable n, larger values of n results in highly blunted nose.
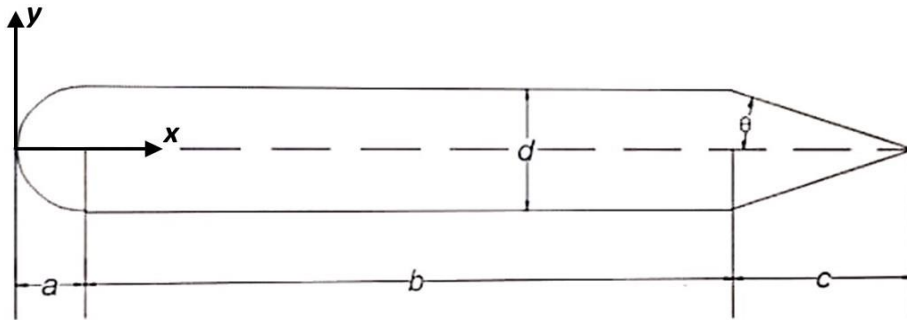
Fig. 3.1: Torpedo geometrical parameters

The cavitator is attached to the torpedo's nose by a 150 mm-long circular rod to generate supercavity as shown in Fig. 3.2.
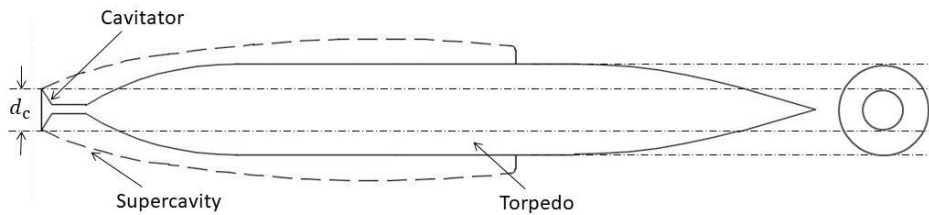
Fig. 3.2: Geometrical features of torpedo with a cavitator attached at the front.

In the present work, seven different cavitator shapes i.e., a disc cavitator (DC), conical cavitator (CC), tapered cone cavitator (TC), an elliptical cavitator (EC), a parabolic cavitator (PC), a spherical cavitator (SC), and Myring cavitator (MC) are employed to generate a supercavity on the torpedo. The diameter of all the cavitators (d_c) is kept constant i.e., 320 mm in the present study. Figure Fig. 3.3 shows the shapes of these cavitators.
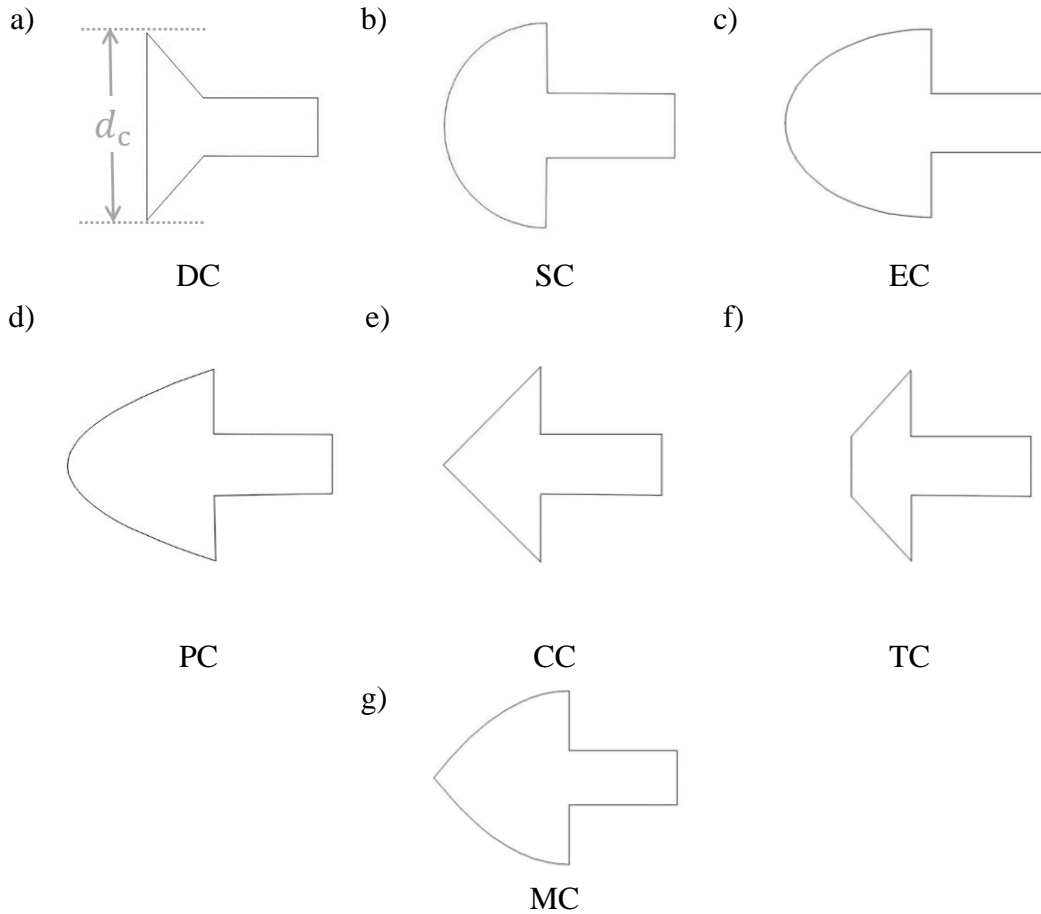
Fig. 3.3: Shape of various cavitator used in present study: (a) Disc Cavitator, (b) Spherical Cavitator, (c) Elliptical Cavitator, (d) Parabolic Cavitator, (e) Conical Cavitator, (f) Tapered Cone Cavitator and (g) Myring Cavitator

Three different geometrical configurations are used in the case of conical, tapered cone and Myring cavitator shape, Distinct cone angles (θ) are used to design conical cavitators; CC-120, CC-90, and CC-60 (Fig. 3.4a), respectively, have cone angles of 120°, 90°, and 60°. As illustrated in Fig. 3.4b, varied ratios between the

tapered diameter (a) and base diameter (b) are used to design tapered cone cavitators; TC-16, TC-32, and TC-48 have, respectively, a/b ratios of 16%, 32%, and 48%. Myring cavitators (Fig. 3.4c) are designed to offer low pressure drag using Eqn. (3.1). Three different values of n are adopted for the design of the Myring cavitators; the n values for the MC-1, MC-1.5, and MC-2 are 1, 1.5, and 2 respectively.

(a)

CC-60   CC-90   CC-120

(b)

TC-16   TC-32   TC-48

(c)

MC-1   MC-1.5   MC-2
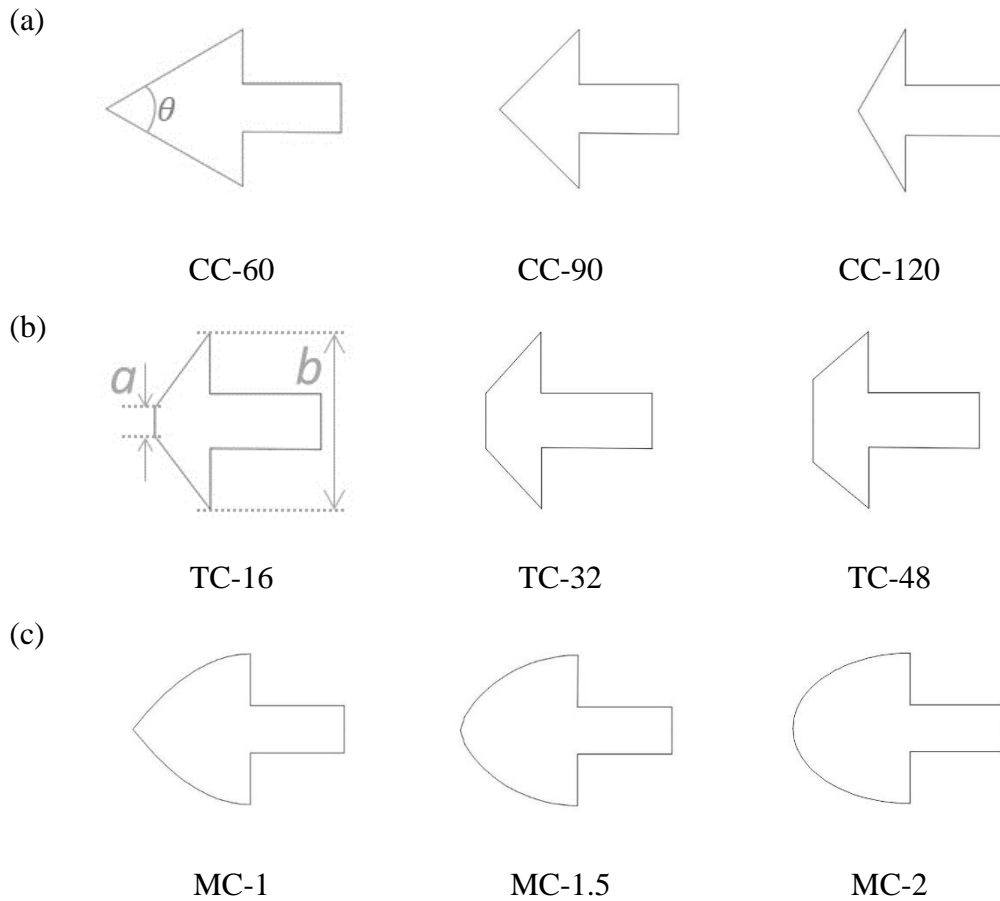
Fig. 3.4: Various geometrical configurations of (a) Conical Cavitators (CC), (b) Tapered Cone Cavitators (TC), and (c) Myring Cavitators (MC) used in the present study.

3.1.2 Meshing

To finalize the mesh for the present study, a grid independence test is conducted using four structured meshes with different numbers of elements. The first mesh, referred to as Mesh-1, contains around 40,000 elements. For the second mesh (Mesh-2), the number of elements is increased by 1.4, resulting in approximately 56,000 elements. Similarly, the third mesh (Mesh-3), and fourth mesh (Mesh-4) contain 80,000 and 112,000 elements, respectively. The details of all the meshes are tabulated in Table 3.1.

Table 3.1: Properties of meshes used for grid independence test

Mesh	No. of elements	Wall Distance	Y+ Value
Mesh-1	40,000	$6.1 \times 10^{-5} \, m$	150
Mesh-2	56,000	$4.1 \times 10^{-5} m$	100
Mesh-3	80,000	$1.6 \times 10^{-5} m$	40
Mesh-4	112,000	$8.2 \times 10^{-6} m$	20

The simulation is conducted at five different cavitation numbers ranging from 0.09 to 0.13 on a torpedo with a conical cavitator having a diameter of 120mm (CC-120). The non-dimensional length of the supercavity, calculated as $\tilde{L} = L/d_c$, where L is the supercavity length, and d_c is the cavitator's diameter, is compared for each case as shown in Fig. 3.5.
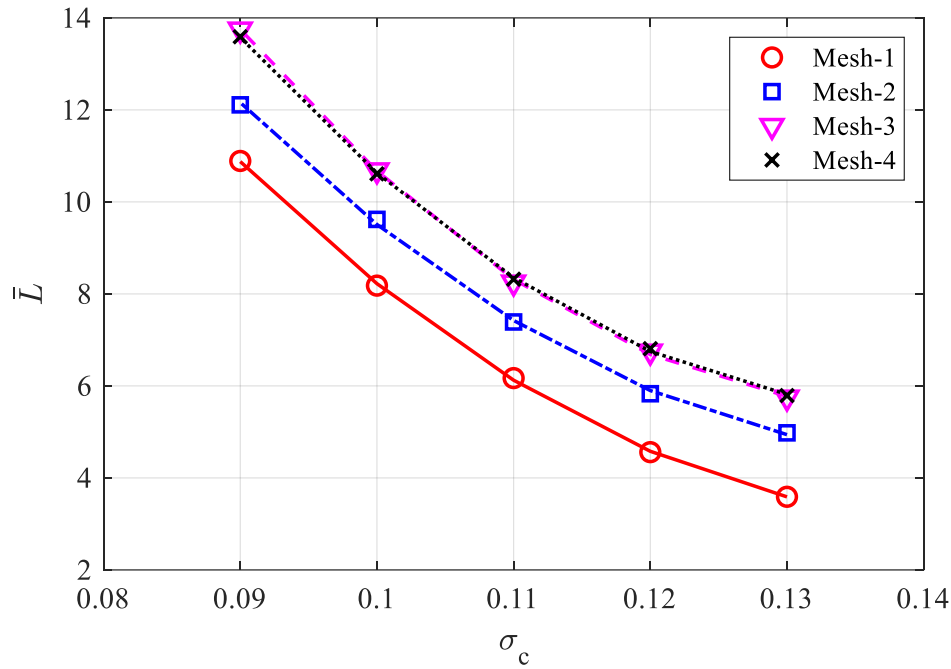
Fig. 3.5: Variation of non-dimensional cavitation length ($\tilde{L}$) with cavitation number (σ_c) for various meshes.

It is observed that the value of $\tilde{L}$ is changing with the number of elements for Mesh-1 and Mesh-2. However, the corresponding value remains approximately the same for Mesh-3 and Mesh-4 for all cavitation numbers. Therefore, Mesh-3, which consists of about 80,000 elements, is considered for discretizing the fluid domains of all the simulations discussed in this paper, as shown in Fig. 3.6a.

The first cell's size is determined based on the Reynolds number range. The smallest element size which is placed on the surface of the solid object corresponds to a y+ of 40, which is outside the viscous sublayer. The wall function is employed to determine the properties within the viscous sublayer. A growth factor of 1.2 is used to generate coarser grid away from the surface. Fig. 3.6(b) shows the zoomed-in view of the mesh near the cavitator surface.
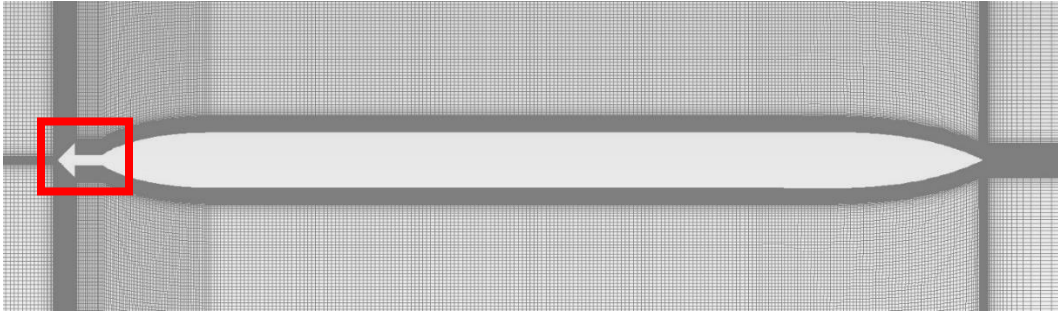
(a)
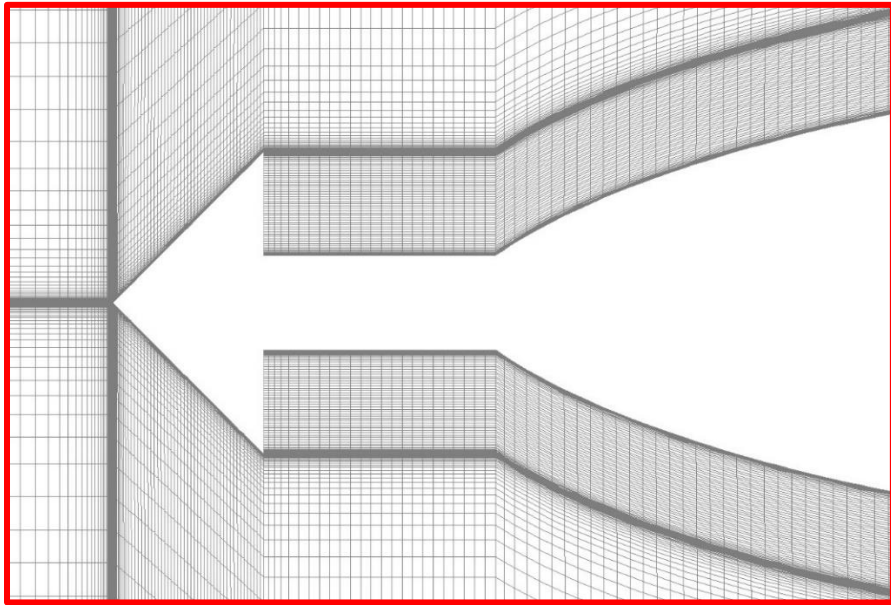
(b)

Fig. 3.6 (a) Discretization of the computational domain (b) Zoomed in view of the mesh near the cavitator

3.1.3 Computational Methodology

3.1.3.1 Governing Equations

The computations are carried out on ANSYS Fluent software. The 2D steady axisymmetric model is used for the simulations carried out in the present work. Computations are based on the solution of Reynolds-Averaged Navier-Stokes (RANS) equations, which is solved using pressure-based algorithm. The RANS approach is based on the assumption that the turbulence in a flow can be represented by the time-averaged velocity field. This time-averaged velocity field is then used to calculate the Reynolds stresses and turbulence intensities, which are important for the estimation of the rate of generation and dissipation of turbulent kinetic energy. For a homogeneous mixture without relative motion between the phases, the mass and momentum governing equation of RANS are given in Eqn. (3.3) and (3.4) respectively.

$$\frac{\partial \rho}{\partial t} + \nabla(\rho V) = 0 \qquad \qquad \text{.....Eqn. (3.3)}$$

$$\frac{\partial (\rho V)}{\partial t} + \nabla(\rho U.U) = -\nabla p + \nabla \tau + F \qquad \text{..... Eqn. (3.4)}$$

where τ is Newtonian viscous stress tensor and F is body forces acting on the flow. For the coupling of velocity and pressure terms, a coupled scheme is utilized. Gradients are evaluated using least squares cell-based method.

3.1.3.2 Operating Conditions

For the current investigation, seawater and water vapor are the primary and secondary phase materials respectively; their properties being defined in Table 3.2. The simulations are conducted at an operating pressure of 201681 Pa, which corresponds to pressure at a depth of 10 meters. The boundary conditions type for inlet and outlet are velocity inlet and pressure outlet respectively. The simulations are conducted at flow velocities ranging from 47.5 m/s to 60 m/s.

Table 3.2: Properties of seawater used in present computations.

Fluid Property	Value
Density (ρ)	$1023 \ kg/m^3$
Dynamic Viscosity (μ)	$9.2 \ X \ 10^{-4} \ kg/ms$
Saturation Pressure	$3494 \ Pa$
Specific Heat (c_p)	$4010 \ J/kgK$

3.1.3.3 Multiphase flow model

To account for Multiphase flow dynamics, the VOF equations are solved using implicit volume fraction formulation. The VOF method tracks the interface between different phases in a flow, such as liquid and gas, by defining a scalar field that represents the fraction of each phase present at any given location. The transport equation for the volume fraction of the liquid and vapour phase can be expressed in Eqn. (3.5) and (3.6) respectively.

$$\frac{\partial \alpha_l}{\partial t} + \nabla.(\alpha_l U) = \frac{\dot{m}}{\rho_l} \qquad \qquad \text{.....Eqn. (3.5)}$$

$$\frac{\partial \alpha_v}{\partial t} + \nabla.(\alpha_v U) = -\frac{\dot{m}}{\rho_v} \qquad \qquad \text{.....Eqn. (3.6)}$$

where α_l and α_v denotes the volume fraction of the liquid and vapour phases respectively, ρ_l and ρ_v represents the density of liquid and vapour phase respectively, $\dot{m}$ donates the mass transfer rate per unit volume caused by cavitation between the liquid and vapor phase.

3.1.3.4 Cavitation model

In this study, cavitation phenomenon is responsible for the mass transfer between the liquid phase and the vapour phase. The mass transfer rate between the cavitation phases is estimated using the Schnerr and Sauer (Schnerr & Sauer, 2001) cavitation model. In this cavitation model, a correlation between bubble growth and volume fraction change rate is established by using Eqn. (3.7) and (3.8).

For $p > p_v$

$$\dot{m}^+ = C_c \frac{\rho_v \rho_l}{\rho} \alpha_v (1 - \alpha_v) \frac{3}{R} \sqrt{\frac{2}{3} \frac{p - p_v}{\rho_l}} \qquad \text{.....Eqn. (3.7)}$$

For $p < p_v$

$$\dot{m}^- = C_v \frac{\rho_v \rho_l}{\rho} \alpha_v (1 - \alpha_v) \frac{3}{R} \sqrt{\frac{2}{3} \frac{p - p_v}{\rho_l}} \qquad \text{.....Eqn. (3.8)}$$

where R stands for bubble radius, p is static pressure, p_v is vapour pressure, ρ_l is the density of the liquid, α_v is vapour volume fraction, C_c and C_v are coefficients for the cavitation model.

3.1.3.5 Turbulence model

Since cavitation is generally considered a high-turbulence phenomenon, turbulence modelling is important and must be accurately addressed in addition to the cavitation model. In the present study, the realizable k-ε model is employed to predict the turbulence effect outside the viscous sublayer. To model the turbulence properties inside the viscous sublayer, wall function is used. The k-ε turbulence model assumes turbulence as a mixture of coherent structures and turbulence energy, represented by the turbulence kinetic energy (k) and the turbulence dissipation rate (ε). The model solves for the time evolution of these two turbulence quantities and provides a means to predict the turbulence effects on the mean flow. However, the standard k-ε turbulence model can suffer from some limitations, such as producing unphysical negative values of turbulence quantities in some cases. On the other hand, the realizable k-ε model incorporates a correction term to ensure the turbulence dissipation rate remains positive. This correction term helps to avoid unphysical negative values of turbulence quantities, improving the accuracy of the turbulence predictions. The transport equations for the realizable k-ε model are provided in Eqn. (3.9) and (3.10).

$$\frac{\partial}{\partial t}(\rho k) + \frac{\partial}{\partial x_j}(\rho k u_j) = \frac{\partial}{\partial x_j}\left[\left(\mu + \frac{\mu_t}{\sigma_k}\right)\frac{\partial k}{\partial x_j}\right] + G_k + G_b - \rho\varepsilon - Y_m + S_k$$

…..Eqn. (3.9)

$$\frac{\partial}{\partial t}(\rho\varepsilon) + \frac{\partial}{\partial x_j}(\rho\varepsilon u_j) = \frac{\partial}{\partial x_j}\left[\left(\mu + \frac{\mu_t}{\sigma_\varepsilon}\right)\frac{\partial\varepsilon}{\partial x_j}\right] + \rho C_1 S_\varepsilon - \rho C_2 \frac{\varepsilon^2}{k + \sqrt{(\vartheta\varepsilon)}} +$$

$$C_{1\varepsilon}\frac{\varepsilon}{k}C_{3\varepsilon}G_b + S_\varepsilon \qquad\qquad\qquad\qquad\qquad …..\text{Eqn. (3.10)}$$

where G_k, G_b represents the generation of turbulence kinetic energy due to the mean velocity gradients and buoyancy respectively. Y_m represents the contribution of the fluctuating dilatation in compressible turbulence to the overall dissipation rate, σ_k and σ_ε are turbulent Prandtl numbers for k and ε respectively. S_k and S_ε are the source terms for k and ε respectively.

3.1.3.6 Validation of numerical model

The accuracy and reliability of the numerical model used in the present study have been rigorously validated against experiments conducted by R.L. Waid (Waid, 1957). The experiments were performed on a circular disc cavitator with a diameter of 25.4 mm at a freestream velocity of 6 m/s. The experiments were conducted on six cavitation numbers ranging from 0.063 to 0.085 The half-length and maximum diameter of the supercavity is transformed into a non-dimensional form by dividing it by the cavitator diameter. The validation procedure entails comparing the non-dimensional half-length and maximum diameter of the supercavity for various cavitation numbers. Fig. 3.7(a) shows the comparison of non-dimensional half-length, and Fig. 3.7(b) represents the comparison of non- dimensional maximum diameter of the supercavity. The experimental data and computational data show good agreement, with an RMSE value of 4.62% for half-length and 4.01% for maximum diameter of the supercavity.

(a)

(b)
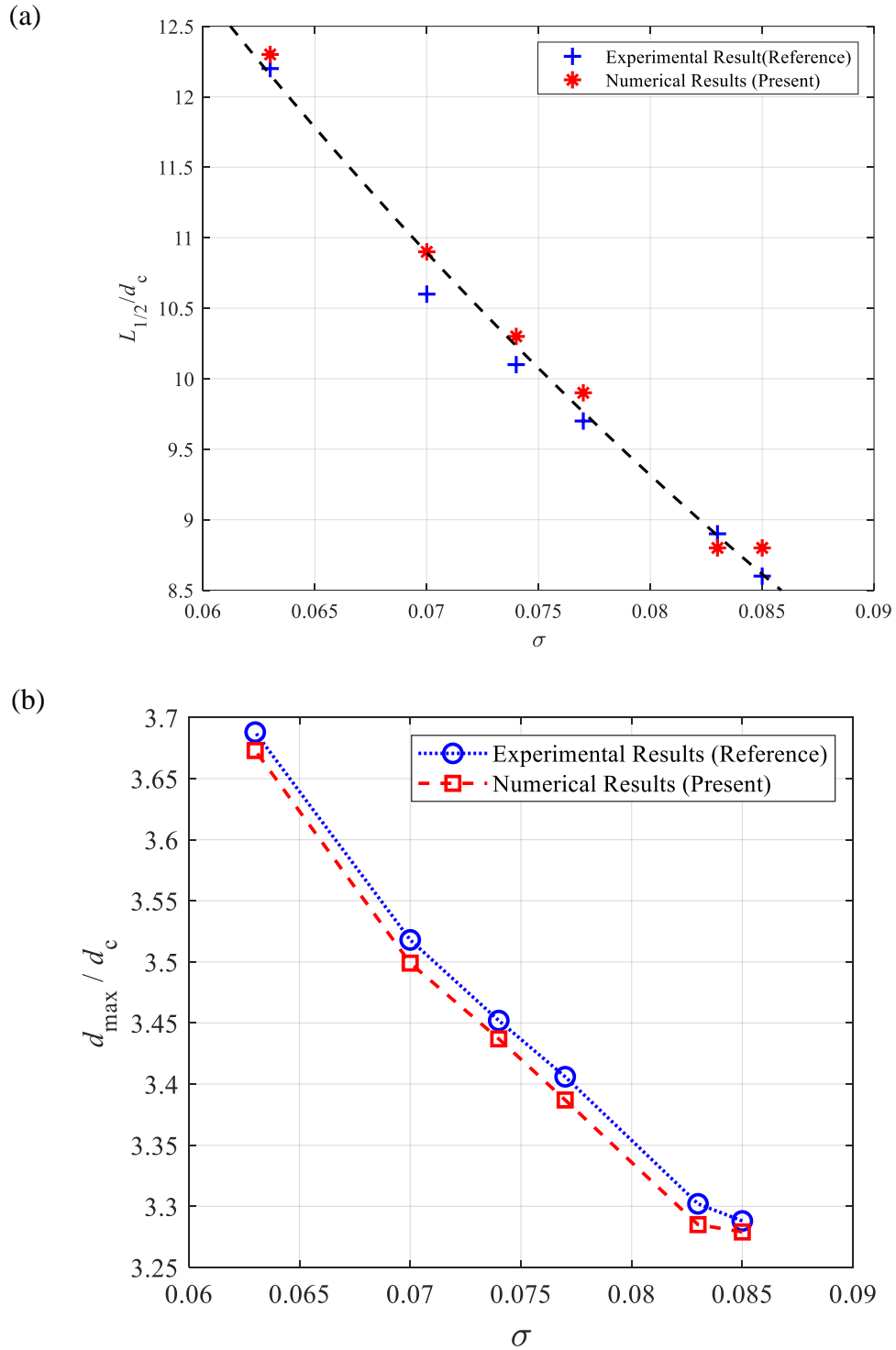
Fig. 3.7: Comparison of (a) Non-dimensional half-length, and (b) Non-dimensional maximum diameter of the supercavity at various cavitation number obtained from computational results from present study with the experimental result reported by R.L. Waid (1957). The dotted line represents the quadratic polynomial curve fit for the computational data.

3.1.4 Simulation Cases

The current study involves conducting simulations on fourteen distinct geometries. Specifically, one of these geometries is a torpedo without a cavitator, while the remaining thirteen geometries have different cavitator shapes. The cavitator shapes utilized in this research are as follows: a disc cavitator (DC), three conical cavitators (CC-120, CC-90, and CC-60), three tapered cone cavitators (TC-0.16, TC-0.31, and TC-0.47), an elliptical cavitator (EC), a parabolic cavitator (PC), a spherical cavitator (SC), and three Myring cavitators (MC-1, MC-1.5, and MC-2). Each of these geometries undergoes testing at five distinct cavitation numbers, ranging from 0.092 to 0.128. Consequently, the study comprises a total of 70 distinct simulations.

3.2 Results

3.2.1 Flow patterns

To comprehend the flow patterns better, streamlines coloured by velocity magnitudes are drawn over various cavitators in figure Fig. 3.8. The pattern of the streamlines clearly suggests that the cavitator deflected the flow of seawater away from the torpedo, creating a region of low pressure adjacent to the torpedo's surface. Water starts converting into vapour phase owing to the low ambient static pressure. Since there is an adverse pressure gradient, the vapour tends to migrate upstream and generate a reverse flow. The entire process results in the formation of a recirculating zone of water vapour inside the supercavity. It was noticed that, when the supercavity length is smaller than the nose cone of the torpedo, a single recirculating zone of water vapour is formed just behind the cavitator and extended up to the cavity closure as shown in the Fig. 3.8(a). However, when the supercavity length is larger than the torpedo's nose cone, two recirculating zones are observed. The first recirculating zone forms immediately following the cavitator (Fig. 3.8b) whereas, the second is observed at supercavity closure. The vapour exits from the first recirculating zone and follows the flow downstream until it reaches the second recirculation zone at the supercavity closure. A new recirculating zone arises at the cavity closure as a result of high pressure at the cavity closure forcing the vapour to start moving upstream once again.
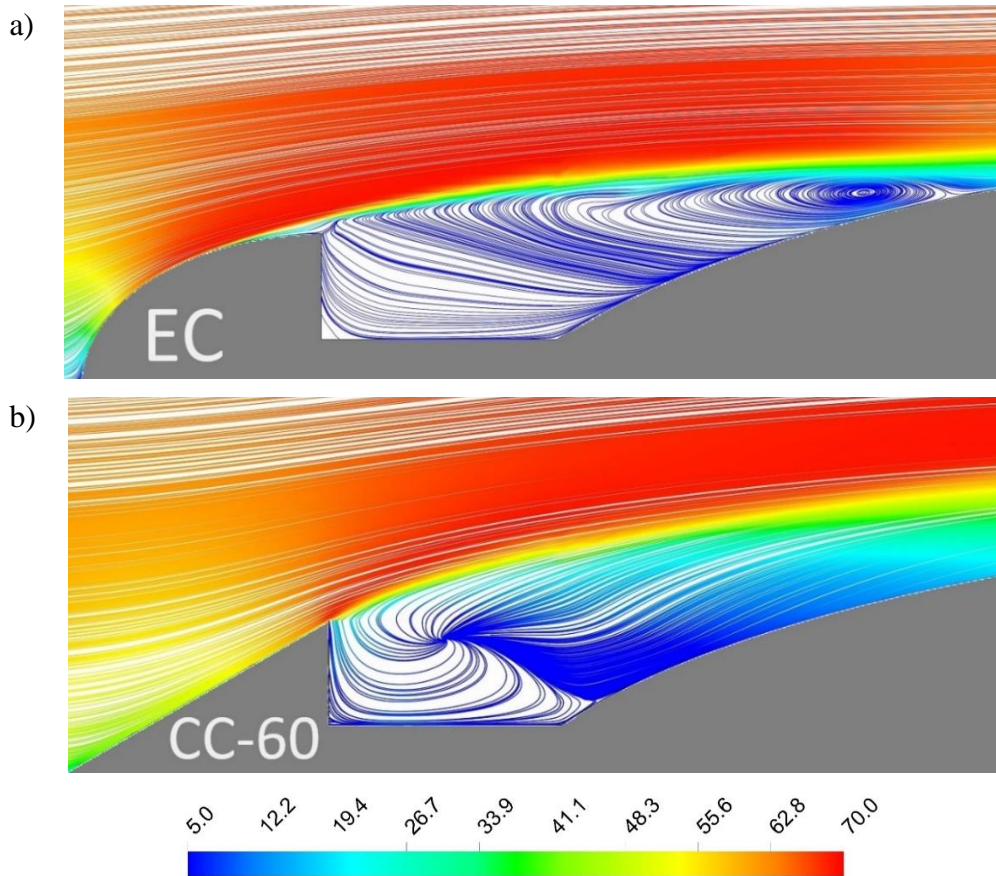
Fig. 3.8: Streamlines coloured by velocity magnitude over a) EC and b) CC-60 cavitators. Freestream flow is from left to right.

3.2.2 Supercavity size

The size of the supercavity is crucial in determining the amount of friction drag that will be applied to the torpedo's body. Therefore, it is imperative to design a cavitator that can produce a supercavity to span the maximum possible torpedo surface area. Fig. 3.9 shows the volume fraction of seawater that depicts the supercavity shape for various cavitators at fixed cavitation number. The contours clearly demonstrate that the disc cavitator (DC) can generate the largest supercavity, followed by the conical cavitator (CC-120), truncated cone cavitator (TC-16), spherical cavitator (SC), parabolic cavitator (PC), Myring cavitators (MC-1.5) and the elliptical cavitator (EC). The observations indicate that the size of the supercavity produced is dictated by the ability of the cavitator to divert the flow in the radially outward direction. The flow resulting from radial

51

motion undergoes a localised contraction region, leading to a reduction in the local static pressure to ranges comparable to the vapour pressure of the liquid. This process induces the vaporisation of the water, resulting in the subsequent creation of the supercavity.

Fig. 3.9: Contour of volume fraction of seawater at σ_c of 0.09 for various cavitators: a) Without cavitator, b) DC, c) CC–120, d)TC-16, e) SC, f) PC g) MC-1.5, and h) EC

52

It is also observed that for conical cavitators (CC), the length of the supercavity decreases with a decrease in the cone angle i.e., CC-120 produces the larger supercavity followed by CC-90 and CC-60 as shown in Fig. 3.10. The CC-120 cavitator deflects the flow in a radial outward direction at a higher angle as compared to the other two configurations, leading to the formation of a longer supercavity. This observation aligns with the previously suggested explanation for the size of the supercavity.
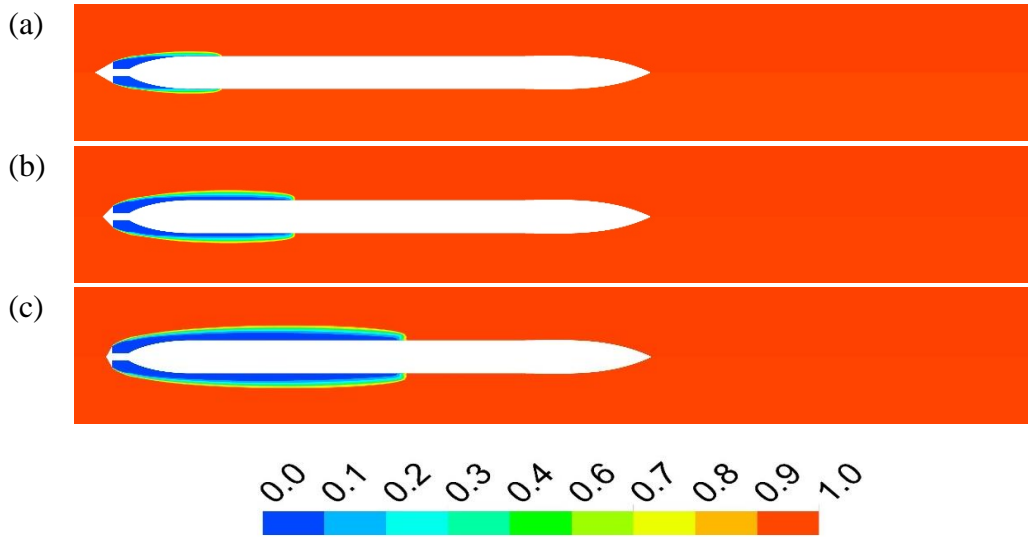
Fig. 3.10: Contour of volume fraction of seawater at σ_c of 0.09 for various configurations of conical cavitator (a) CC-60, (b) CC-90 and (c) CC-120

In the case of truncated cone cavitators (TC), the size of the supercavity reduces with an increase in a/b ratio, which means that TC-16 yields the largest supercavity, whereas TC-48 yields the smallest supercavity as shown in Fig. 3.11. This occurrence can be attributed to the fact that a smaller a/b ratio yields a greater flow deflection angle, hence causing formation of a larger supercavity. For the Myring cavitator (MC), it was observed that MC-1 forms the longest supercavity, followed by MC-1.5 and MC-2. It is noteworthy that the length of the supercavity decreases with an increase in the value of n, which represents the increase in the bluntness of the cavitator for fixed cavitator diameter and length. Among the three different configurations, MC-1 is the least blunt, resulting in the highest flow deflection angle along its outer periphery and thus generating to a bigger

supercavity. In contrast, the periphery of MC-2 exhibits a near-parallel alignment with the direction of the freestream velocity.
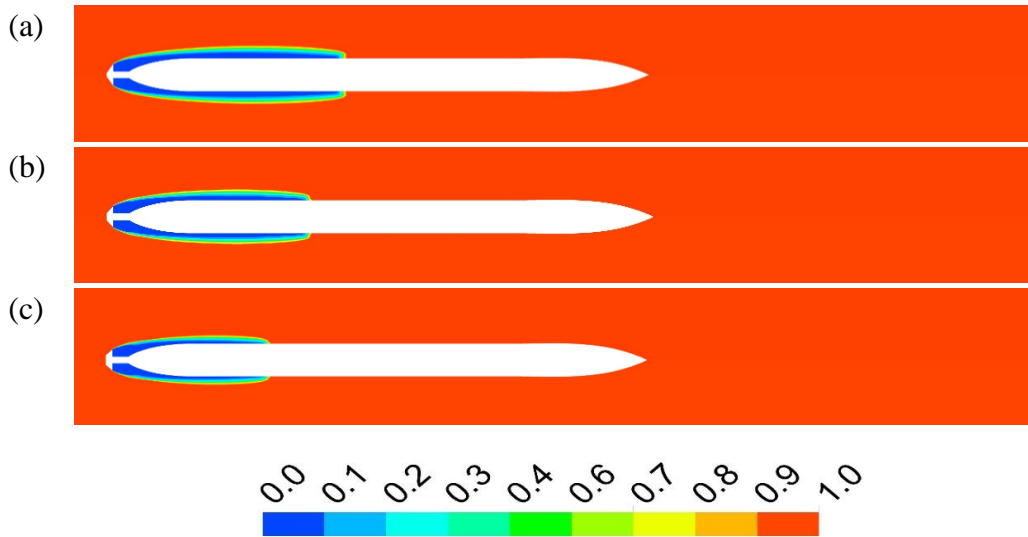
Fig. 3.11: Contour of volume fraction of seawater at σ_c of 0.09 for various configurations of tapered cone cavitator (a) TC-16, (b) TC-32 and (c) TC-48

For the Myring cavitator (MC), it was observed that MC-1 forms the longest supercavity, followed by MC-1.5 and MC-2 as shown in Fig. 3.12. It is noteworthy that the length of the supercavity decreases with an increase in the value of n, which represents the increase in the bluntness of the cavitator for fixed cavitator diameter and length.
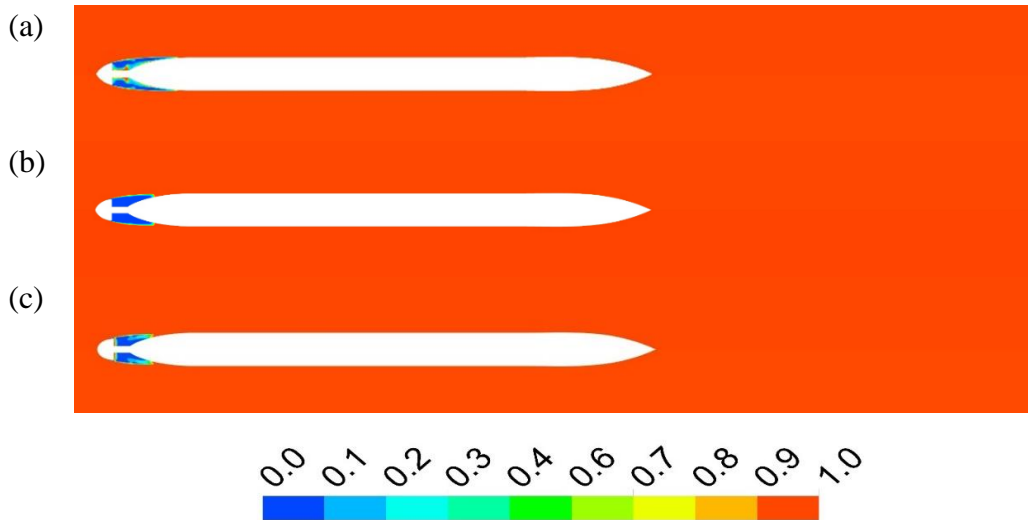
Fig. 3.12: Contour of volume fraction of seawater at σ_c of 0.09 for various configurations of Myring cavitator (a) MC-1, (b) MC-1.5 and (c) MC-2

Among the three different configurations, MC-1 is the least blunt, resulting in the highest flow deflection angle along its outer periphery and thus generating to a bigger supercavity. In contrast, the periphery of MC-2 exhibits a near-parallel alignment with the direction of the freestream velocity.

3.2.3 Cavitator performance evaluation at various cavitation numbers (σ_c)

To effectively comprehend the performance of cavitator at varying σ_c, a plot illustrating the relationship between non-dimensional supercavity length $(\tilde{L})$ and σ_c is shown in Fig. 3.13, where $(\tilde{L})$ is defined as the ratio of the length of supercavity divided by cavitator diameter i.e. $\tilde{L} = L/d_c$. The length of the supercavity increases squarely in proportion to the decrease in the cavitation number. This happens because the decrease in the cavitation number represents a rise in the energy of expansion $(0.5\rho V^2)$ over the energy of contraction $(p_o - p_c)$.

The plot indicates that the disc cavitator can develop the largest supercavity compared to the other cavitators for all the values of σ_c, and the largest cavity was observed at σ_c of 0.09 with $(\tilde{L})$ of approximately 20. Moreover, it is noted that the order of the size of the supercavity formed by various cavitators observed at σ_c of 0.09 in the previous section is found to be the same for other values of σ_c as well. Therefore, it can be inferred that the ability of a cavitator to generate larger supercavity is dependent upon the divergence angle of the flow's direction. It is noteworthy that each cavitator does have a different capability of producing supercavitation and must be employed according to torpedo size. For instance, CC-120 is the preferred option for torpedoes with a length that corresponds to $(\tilde{L})$ of 14, whereas TC-16 is the recommended option for torpedoes with a length corresponding to $(\tilde{L})$ of 9. When selecting the cavitator, pressure drag must also be taken into consideration in addition to the supercavity size, which is discussed in the coming section.

a)

b)
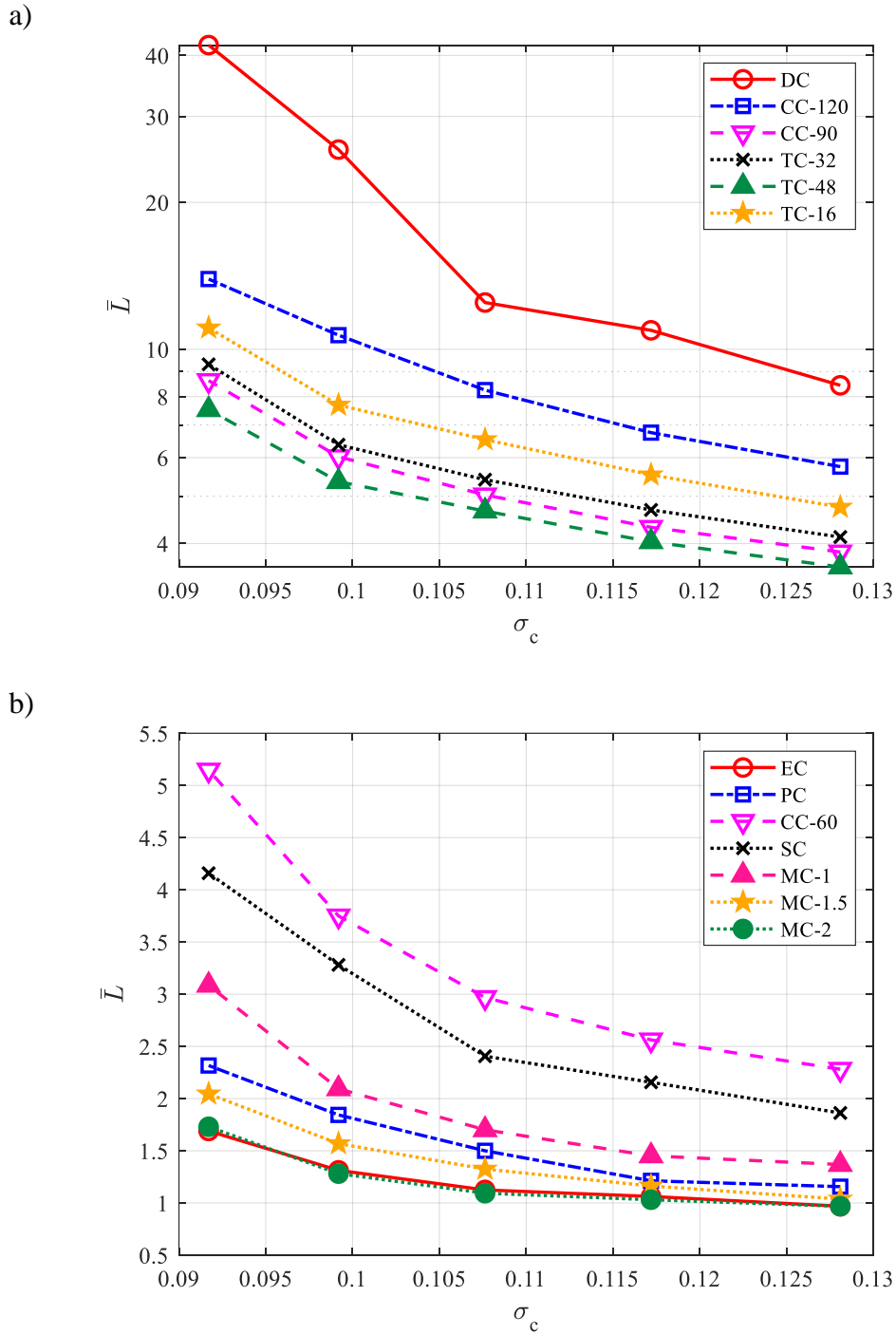
Fig. 3.13: Variation of non-dimensional length of the supercavity at various cavitation number for (a) the cavitators producing relatively large supercavities, and (b) those producing smaller supercavities.

A similar limitation on the torpedo diameter is also applicable, and thus the diameter of the torpedo must be decided such that the torpedo body accommodates inside the supercavity. Non-dimensional supercavity diameter $(\widetilde{D})$ is defined as the ratio of supercavity maximum diameter (d_{max}) to the cavitator diameter (d_c). Fig. 3.14 shows the variation of $(\widetilde{D})$ with σ_c for various cavitators.

a)

b)
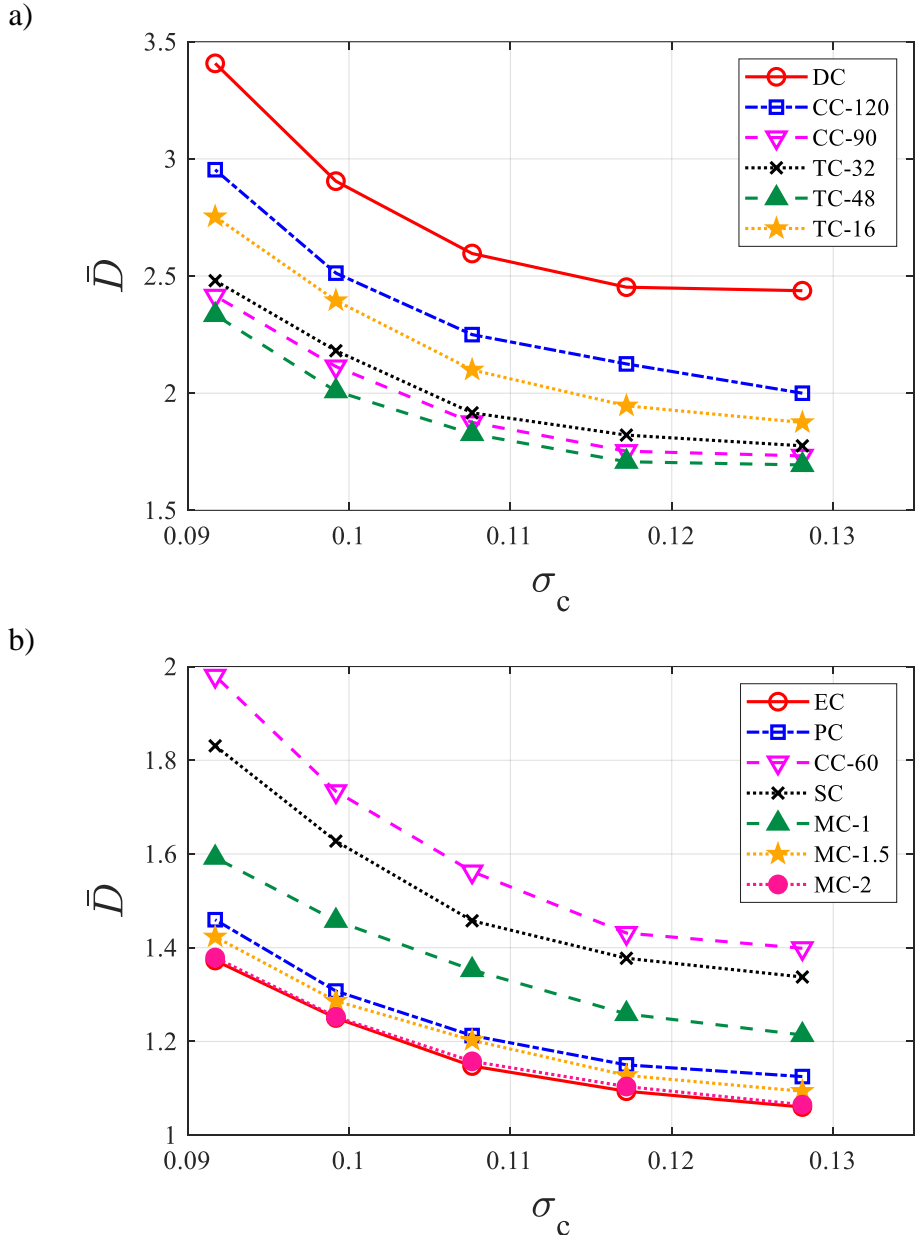
Fig. 3.14: Variation of non-dimensional maximum diameter of the supercavity at various cavitation number for (a) the cavitators producing relatively large supercavities, and (b) those producing smaller supercavities.

3.2.4 Skin friction drag

Once the supercavitation phenomenon creates a water vapour layer, the torpedo experiences reduced skin friction drag because the vapour layer reduces the contact area between the torpedo's surface and the water. The reduction in the amount of skin friction drag depends on the geometry of both the supercavity as well as the torpedo. The data presented in this section pertain to a heavy-weight torpedo with a diameter of 800 millimetres and a length of 8 metres. The plot shown in Fig. 3.15 illustrates the variation of the coefficient of skin friction drag at various cavitation numbers for different cavitators. It is apparent that the majority of the cavitator significantly decreased the skin friction drag as compared to the case without cavitator.

When considering a torpedo without a cavitator, the coefficient for skin friction drag is approximately 0.095 and maintains a relatively constant value, even when the cavitation number changes. On the other hand, when cavitators are incorporated, the coefficient for skin friction drag decreases as the cavitation number decreases due to the expansion of the supercavity. In the case of a disc cavitator, the coefficient for skin friction drag initially experiences a reduction, but subsequently stabilizes almost entirely after reaching a cavitation number of 0.11. This is because once the cavitation number reaches 0.11, the supercavity has enveloped the entire torpedo, resulting in minimal observable drag reduction despite the increase in supercavity size. The most significant decrease in skin friction drag occurs with the implementation of a disc cavitator, achieving an approximate reduction of 92%. Following closely is the CC-120 cavitator, which achieves a reduction of around 79%.

Notably, however, even though the supercavity formed by the disc cavitator at a cavitation number of 0.09 is almost 1.43 times larger than that created by the CC-120 cavitator, the percentage difference in the reduction of skin friction drag is merely 13%. This happened because the supercavity generated by the disc cavitator extends beyond the torpedo body, and the trailing portion of this supercavity does

not contribute to the reduction in skin friction drag. Therefore, it is crucial to select a cavitator that produces a supercavity just large enough to surround the torpedo body.

a)
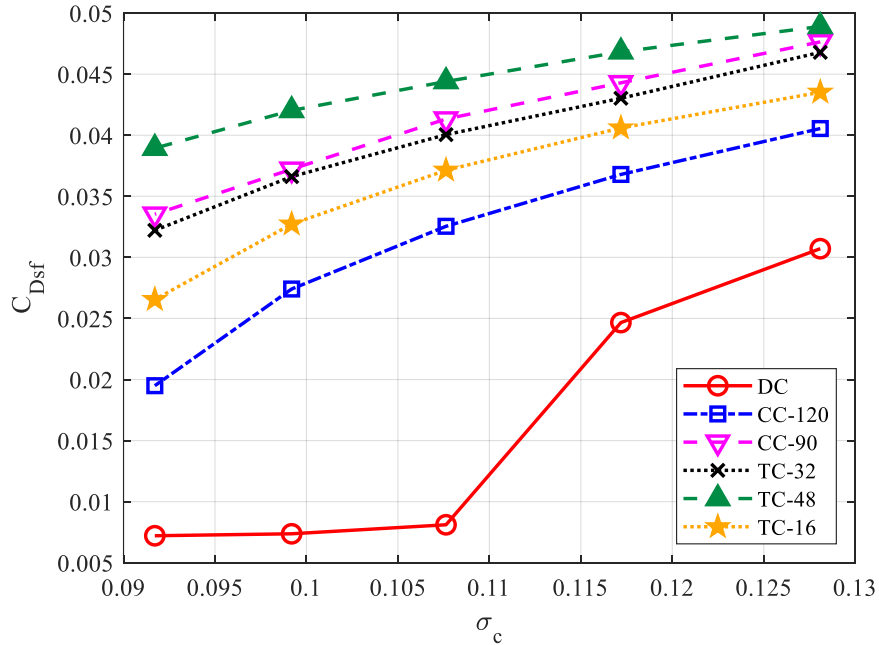
b)
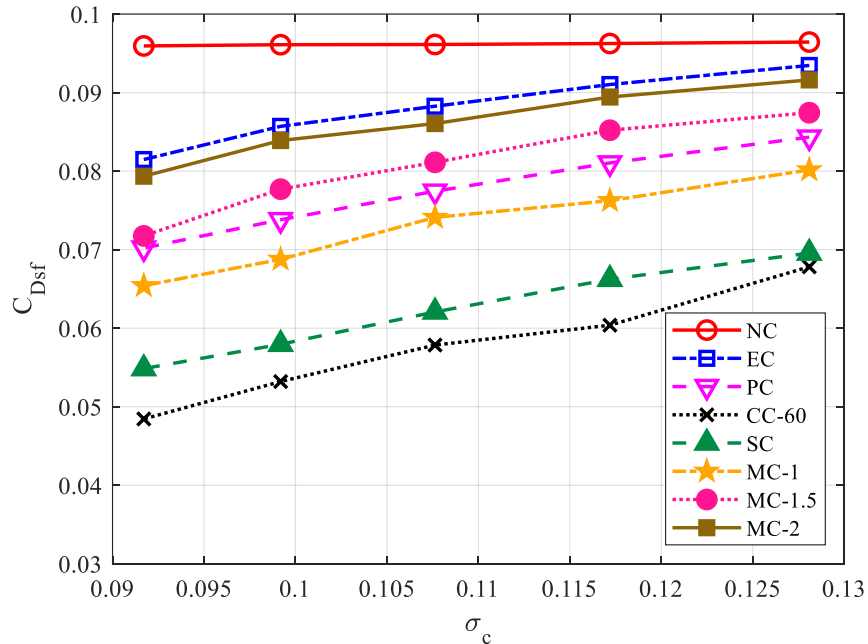
Fig. 3.15: Variation of skin friction drag coefficient (C_{Dsf}) with cavitation number for (a) the cavitators producing relatively large supercavities, and (b) those producing smaller supercavities.

3.2.5 Pressure Drag due to cavitator

Although the integration of the cavitator on the torpedo nose reduces the skin friction drag but it is also associated with a disadvantage of additional pressure drag offered by the cavitator. Fig. 3.16 shows the change in pressure drag coefficient due to the addition of each cavitator at different σ_c. The plot indicates that the cavitators that produce large supercavity also provide high pressure drag. The reason for this finding can be attributed to the fact that cavitators with higher flow deflection angles exhibit larger stagnation regions. As a result, the front surface of the cavitator experiences higher pressure, leading to a correspondingly greater amount of pressure drag. For instance, a disc cavitator, due to its high flow deflection angle, has the largest stagnation zone; consequently, it is subject to the highest amount of pressure drag.

a)

b)
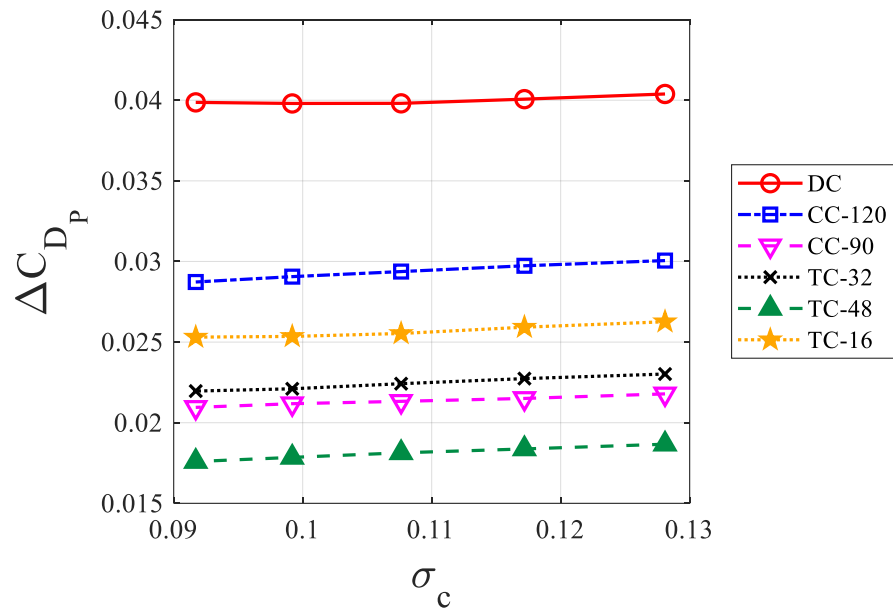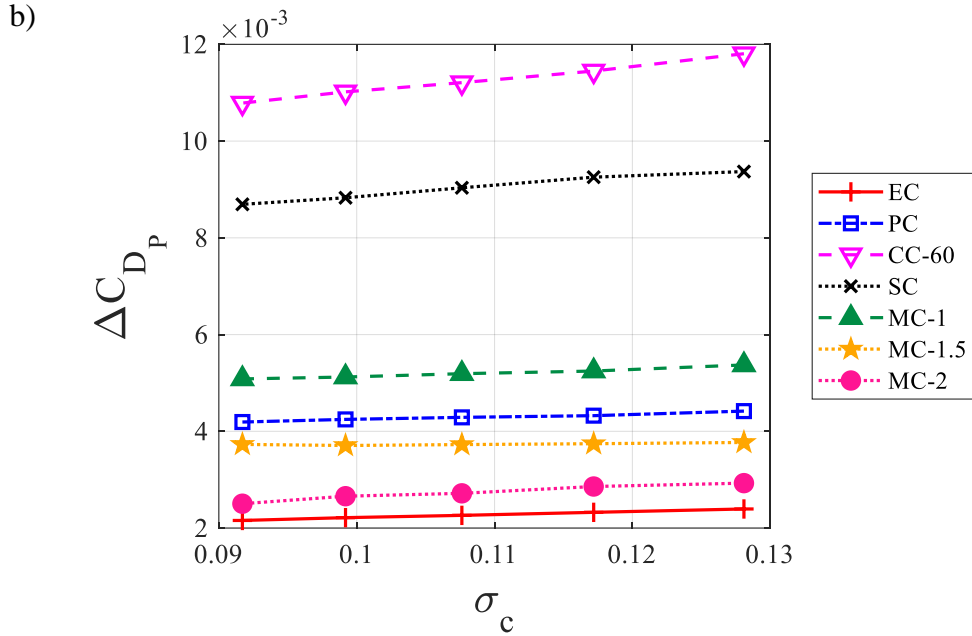
Fig. 3.16: Change in pressure drag coefficient (C_{Dp}) at various cavitation number σ_c due to addition of (a) the cavitators producing relatively large supercavities, and (b) those producing smaller supercavities.

3.2.6 Selection of a cavitator: Comprehensive analysis of overall drag

The choice of a cavitator is determined based on the reduction in the overall drag coefficient resulting from its deployment as compared to the case when no cavitator is employed (NC). Therefore, it is necessary to take into consideration both the reduction in skin-friction drag (which depends on the supercavity and torpedo size) and the increase in pressure drag when identifying the best-suited cavitator shape for a particular torpedo. Table 3.3 presents a comparison of the drag coefficients of the three cavitator types: DC, CC-120, and TC-16 at cavitation number of 0.09 with respect to NC scenario. Other cavitators are not included in this evaluation due to their limited ability to generate a supercavity in comparison to the length of the torpedo under consideration, resulting in minimal reduction in skin friction drag. It can be deduced from the data that the disc cavitator is the most suitable choice for the heavyweight torpedo under investigation.

61

Table 3.3: Comparison of various drag coefficients for DC, CC-120 and TC-16 cavitator with respect to no cavitators (NC)

Cavitator	Reduction in skin-friction drag coefficient	Increase in pressure drag coefficient	Net reduction in overall drag coefficient
Disc	0.0887	0.0399	0.0488
CC-120	0.0765	0.0287	0.0478
TC-16	0.0694	0.0253	0.0441

Nevertheless, the installation of a disc cavitator on a smaller-sized torpedo may lead to an increase in overall drag. This is due to the fact that the reduction in skin friction drag is not as significant as the substantial increase in pressure drag. Consequently, other cavitators have the potential to outperform the disc cavitator. For example, when the length of the torpedo is 10 times the diameter of the cavitator, DC, CC-120, and TC-16 cavitators can create a supercavity at a cavitation number of 0.09 that is capable of fully enclosing the torpedo while maintaining a similar level of skin friction drag. As a result, the cavitator with the lowest pressure drag, TC-16 in this scenario, will result in the least overall drag. In a similar vein, the CC-60, SC, and MC-1 cavitators are considered advantageous when the length of the torpedo is 5, 4, and 3 times the diameter of the cavitator, respectively. In summary, it can be inferred that several key aspects, such as torpedo design, cavitation number, supercavity geometry, and pressure drag on the cavitator, play a vital role in determining the most appropriate cavitator for a torpedo.

3.3 Significance of the findings

In the present work, simulations are carried out on thirteen different cavitators, covering a range of cavitation number ranges from 0.09 to 0.13. Various characteristics, including supercavity geometrical parameters, the skin friction drag coefficient, and changes in the pressure drag coefficient, are considered. The study demonstrates that the cavitator's ability to enhance the energy of expansion $(1/2\,\rho V^2)$ by deflecting the flow radially outward allows it to generate a supercavity. The numerical results reveal that the most expansive supercavity is

generated by the disc cavitator (DC), followed by the conical cavitator (CC), truncated cone cavitator (TC), spherical cavitator (SC), parabolic cavitator (PC), Myring cavitators (MC), and the elliptical cavitator (EC). The findings indicate that the dimensions of the supercavity are significantly influenced by the angle at which the flow is deflected by the cavitator. It should be noted that the size of the supercavity increases squarely in proportion to the decrease in the cavitation number for all cavitator shapes.

The reduction in the skin friction drag coefficient depends on the area of the torpedo's body that can be accommodated within the supercavity. During cavitator selection, a judicious choice pertains to the cavitator's capacity to produce a sufficiently capacious supercavity to encapsulate the torpedo. Additionally, in cases where the supercavity's dimensions exceed the torpedo's body, the coefficient of skin friction drag remains relatively constant, even as the supercavity expands. Despite the advantage conferred by diminished skin friction drag, the incorporation of a cavitator introduces the concomitant drawback of supplementary pressure drag. It is noteworthy that increases in the coefficient of pressure drag are particularly higher for cavitators generating larger supercavities. The reason for this behaviour is that a cavitator with a high flow deflection angle also encounters a larger stagnation region, resulting in higher pressure drag.

Thus, the nuanced interplay between changes in skin friction and pressure drag requires meticulous consideration in the cavitator selection process. The selection of a cavitator that generates a supercavity of dimensions just large enough to envelop the entire torpedo is desirable, as smaller supercavities induce escalations in skin friction drag, whereas larger supercavities prompt an increase in pressure drag. Ultimately, this investigation culminates in the assertion that the optimal cavitator choice for a given torpedo depends upon a composite evaluation of multiple factors, including supercavity geometry, torpedo geometry, reductions in skin friction drag, increments in pressure drag, and the range of operating cavitation numbers.

Chapter 4

Heat Enhanced Supercavitation as a strategy for supercavity size enhancement

4.1 Introduction

This chapter discusses the phenomenon of supercavitation, where a vapor-filled cavity is formed around an object moving at high velocity underwater, effectively reducing drag and allowing for high-speed underwater transport. Despite numerous studies on optimizing the supercavity's size and shape, the impact of liquid temperature on supercavity geometry remains underexplored. The liquid temperature plays a significant role in supercavitation, affecting the vapor generation rate and thus the size of the supercavity. Higher temperatures result in greater vapor production, leading to larger supercavity dimensions. This chapter aims to investigate the effect of varying liquid temperatures on the supercavity's properties, providing insights into how temperature variations influence key geometrical parameters like the maximum diameter and half-length of the supercavity.

The current chapter presents the computational methods used to simulate the effects of temperature on supercavitation, which include meshing, boundary conditions, and operating parameters. The results are validated against established empirical data, and the findings highlight the significant influence of temperature on supercavity formation. The next section discusses the various geometry and other conditions at which our simulations are conducted.

4.1.1 Geometry

The present simulations are conducted on a disc-shaped cavitator attached to a connecting rod as shown in Fig. 4.1. The cavitator has a diameter of 200 mm and a width of 50 mm, with slightly tapered edges. The connecting rod, which has a length of 150 mm and a circular cross-section with a diameter of 20 mm, is attached to the center of the cavitator.
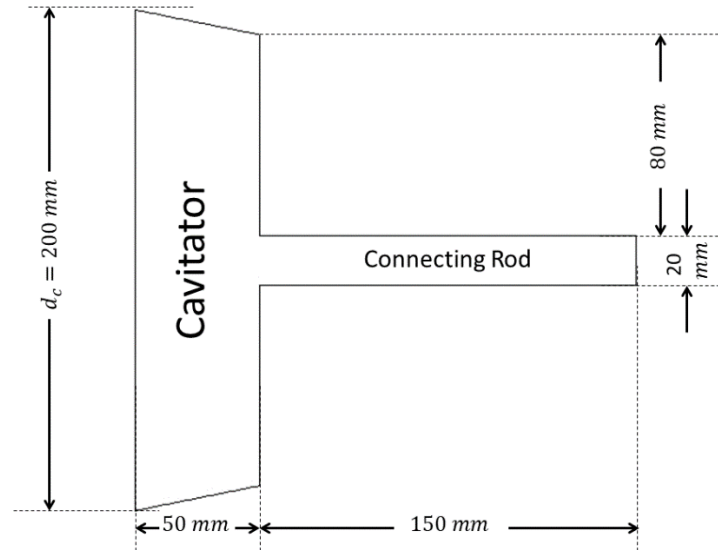
Fig. 4.1: The geometry of cavitator and connecting rod used in present study.

4.1.2 Meshing

The computational mesh for the simulation is generated within a domain extending 1 meter upstream and 10 meters downstream of the cavitator as illustrated in Fig. 4.2. A structured mesh is employed, comprising 103,000 elements, with increased resolution near the cavitator to accurately capture detailed flow dynamics. The Reynolds number for the present study ranges from 9.8×10^6 to 1.3×10^7. The mesh's minimum element size is 1.8×10^{-5} meters, providing sufficient refinement in critical regions around the cavitator. The mesh incorporates a growth factor of 1.2, which manages the gradual expansion of element size with increasing distance from the cavitator. This minimum element size corresponds to a y^+ value of 40, indicating

65

that the mesh does not resolve the viscous sublayer; thus, a standard wall function is applied to model flow properties in this region. A high mesh quality is maintained, with a minimum orthogonality of 0.98 and a maximum aspect ratio of 446, ensuring that the elements are well-oriented with respect to the flow.
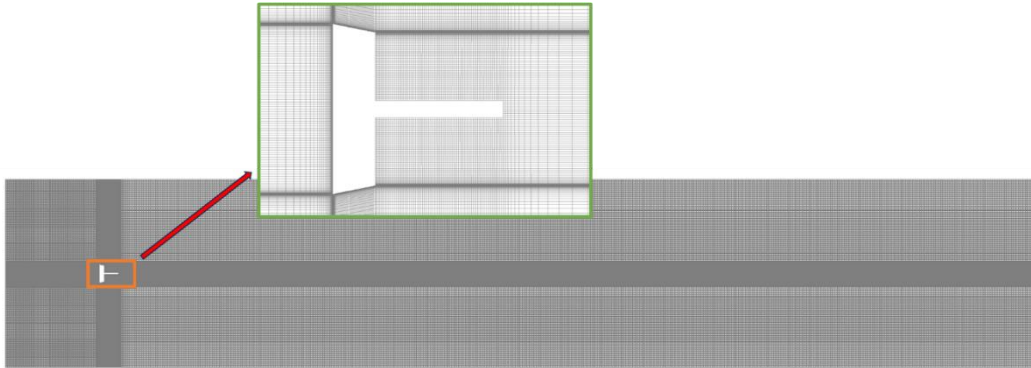
Fig. 4.2: The present computational domain discretized using structured mesh with grid refinement near the cavitator.

4.1.3 Computational Methodology

In this study, the computational methodology remains consistent with the approach detailed in Section 3.1.3, ensuring continuity in the core numerical framework. However, to account for temperature variation and the associated phase changes between the liquid and vapor phases, specifically through evaporation and condensation, a few modifications have been introduced. These modifications represent three key differences from the previously described methodology.

First, the energy conservation equation is now solved alongside the mass and momentum conservation equations to capture the thermal effects. Second, an evaporation-condensation model has been incorporated in conjunction with the cavitation model while solving the Volume of Fluid (VOF) multiphase equations, thereby enhancing the accuracy of phase transition predictions. Third, the vapor density is computed at each iteration using the ideal gas law, and viscosity is calculated using the three-coefficient Sutherland law, ensuring more precise thermophysical property estimations during the simulation

.

4.1.4 Simulation Cases

The aim of this study is to estimate the effect of changes in fluid operating temperature on supercavity size across a wide range of cavitation numbers. Since cavitation is influenced by the difference between the fluid's operating temperature and its saturation temperature, a non-dimensional temperature parameter $\tilde{T} = (T_s - T)/T_s$ is defined, where T_s represents the fluid's saturation temperature, and T is the fluid's operating temperature. In this study, seawater temperature is varied between 288 K and 345 K, and the saturation temperature of seawater at a depth of 10 meters is 394 K. Therefore, the corresponding $\tilde{T}$ values range from 0.124 to 0.269. Simulations is conducted for various fluid temperatures across different cavitation numbers, ranging from 0.12 to 0.2.

4.2 Results

4.2.1 Effect of Fluid Temperature on Supercavity Geometry

To extract the supercavity geometry from the present simulations, a contour of the volume fraction of water vapor is plotted. The region where the volume fraction of water vapor is 50% or more is considered the cavitation region. Fig. 4.3 shows the supercavity geometry at various $\tilde{T}$ ranging from 0.129 – 0.269 at fixed cavitation number. It is observed that that as the difference between the operating temperature and the saturation temperature of the working fluid decreases, the length of the supercavity increases.
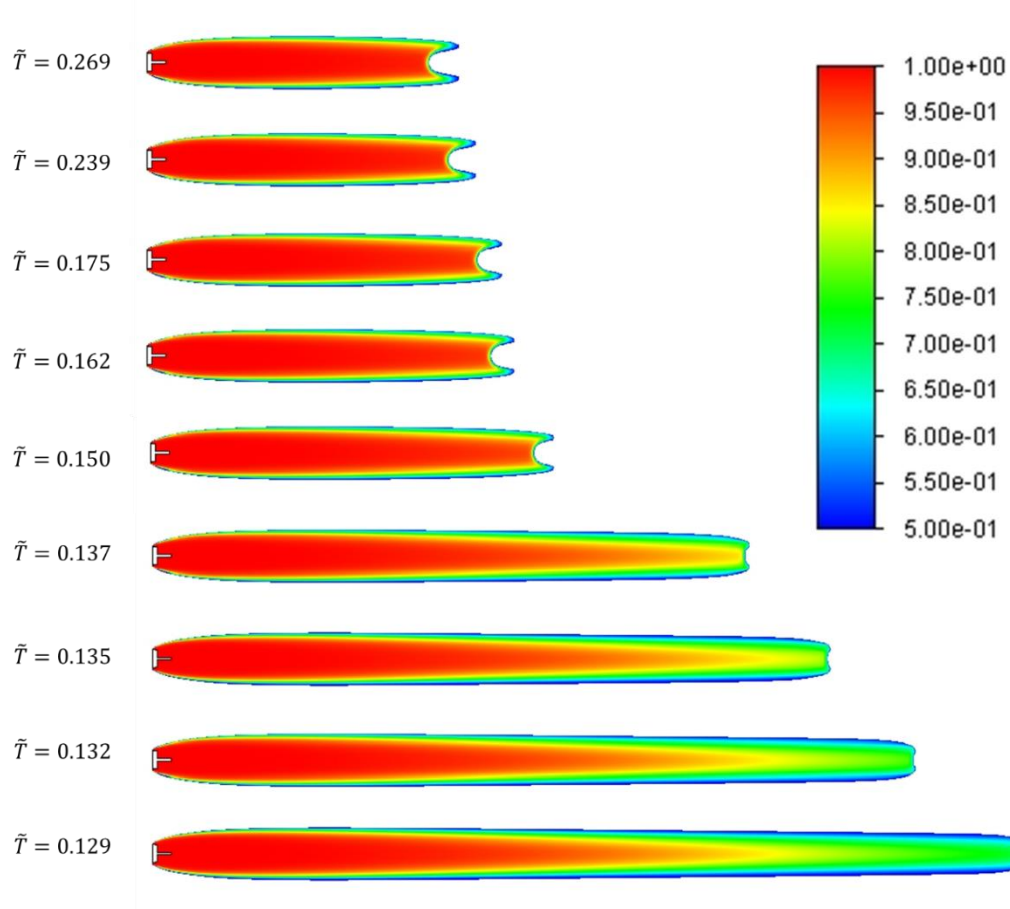
Fig. 4.3: Contour of volume fraction of water vapor at various $\tilde{T}$ at fixed cavitation number

4.2.2 Effect of increasing fluid temperature at varying cavitation number

To observe the effect of increasing the fluid temperature at various cavitation number, a graph is plotted illustrating the relationship between the non-dimensional temperature $(\tilde{T})$ and the non-dimensional supercavity length $(\tilde{L})$ for different values of the cavitation number (σ_c) as shown in Fig. 4.4. Across all cavitation numbers, $(\tilde{L})$ decreases as $(\tilde{T})$ increases. The increase in $(\tilde{L})$ is more pronounced at lower values of $(\tilde{T})$, particularly below $(\tilde{T}) = 0.15$. Fig 4.4 suggests that the supercavity length is independent of temperature at lower temperature values (larger $\tilde{T}$) and exhibit similar behaviour across different cavitation numbers.

At lower cavitation numbers (e.g. $\sigma_c = 0.12, 0.14$), the supercavity length increases rapidly with increasing temperature i.e. decreasing $(\tilde{T})$. This suggests that at lower cavitation numbers, the supercavity is more sensitive to changes in temperature and therefore a increase change in temperature results in a prominent increase in the supercavity length. On the other hand, at higher cavitation number (e.g., $\sigma_c = 0.18, 0.20$), the increase in supercavity with increase in temperature is less steep. This indicates that at higher cavitation numbers, the supercavity is less affected by changes in temperature. As $(\tilde{T})$ increases beyond 0.2, the curves for different σ_c values tend to flatten, indicating that the impact of temperature change on supercavity length diminishes.

Overall, the graph suggests that both fluid temperature and cavitation number significantly influence the supercavity length. At higher $(\tilde{T})$, changes in cavitation number have a more pronounced effect on the supercavity length, while at lower $(\tilde{T})$, the supercavity length becomes highly sensitive to both the parameters.
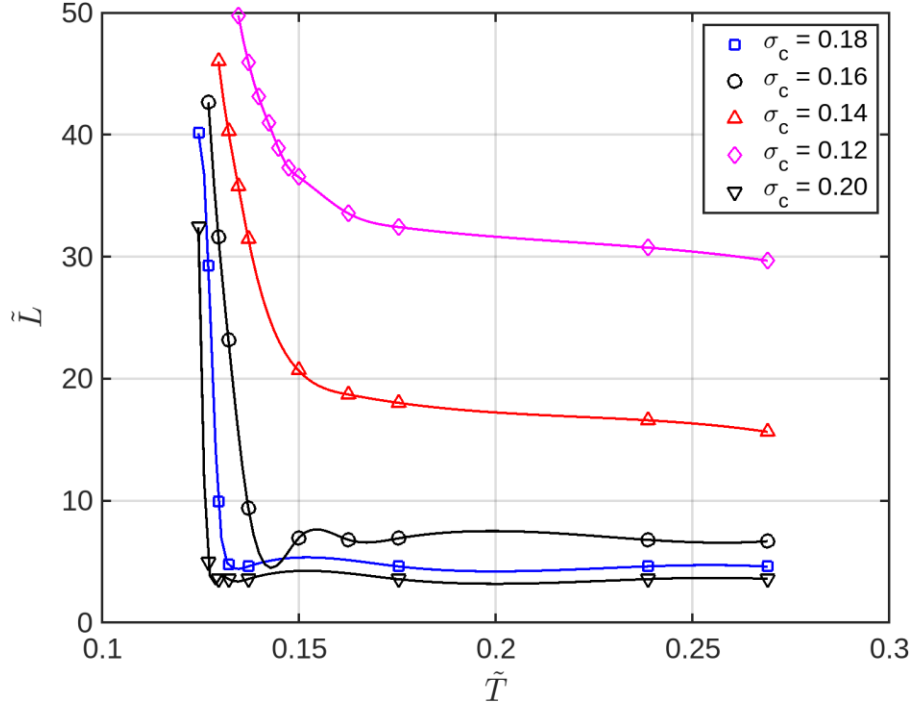
Fig. 4.4: Variation of supercavity length with temperature at various cavitation number

4.2.3 Relationship between critical temperature and cavitation number

As reported in the previous section, after a certain temperature value, the supercavity length becomes very sensitive to changes in temperature. The temperature at which the supercavity length suddenly increases with a rise in temperature is termed the critical temperature. The critical temperature is converted to a non-dimensional form using the relation $\widetilde{T^*} = (T_s - T^*)/T_s$, where T^* is the critical temperature in Kelvin, and $\widetilde{T^*}$ is the non-dimensional critical temperature. Fig. 4.5 shows the relationship between the cavitation number and the non-dimensional critical temperature. The quadratic fit provides a smooth curve that closely follows the trend of the data points, suggesting that the relationship between σ_c and $\tilde{T}^*$ can be adequately modeled by a quadratic equation. This fit can help predict $\tilde{T}^*$ values for other σ_c values within the range studied.
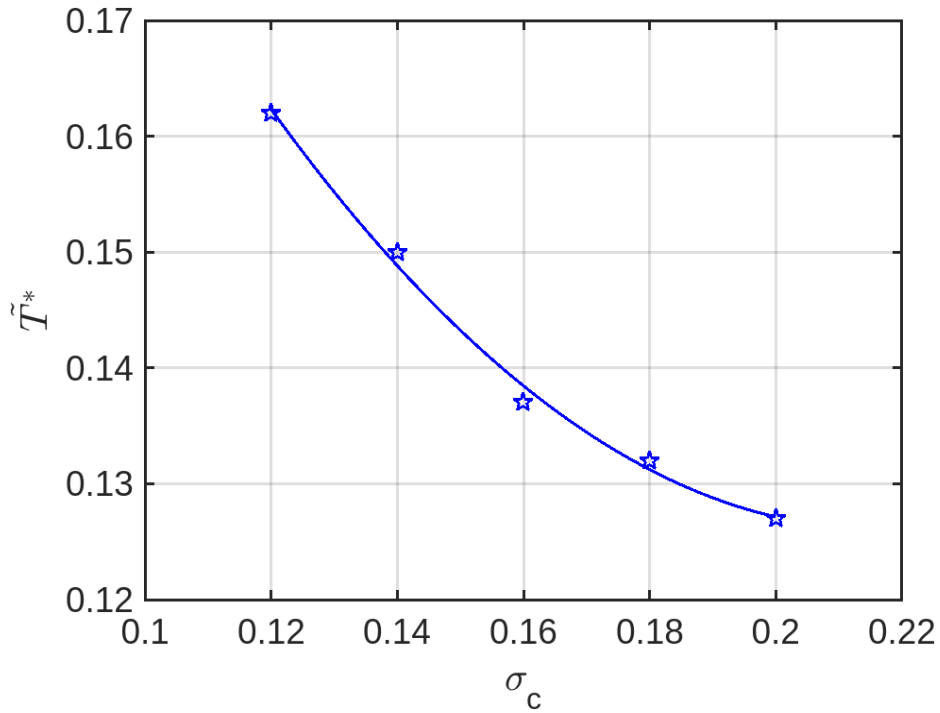
Fig. 4.5: Relationship between the cavitation number and the non-dimensional critical temperature.

4.3 Significance of the findings:

The present study demonstrates the significant influence of fluid operating temperature on the geometry of supercavities formed by a disc-shaped cavitator. As the operating temperature approaches the saturation temperature of the fluid, the length of the supercavity increases, particularly at lower cavitation numbers. This sensitivity diminishes as the cavitation number rises, indicating a complex interplay between temperature and cavitation dynamics. The relationship between cavitation number and critical non-dimensional temperature, successfully modeled by a quadratic equation, provides a predictive tool for assessing supercavity behavior under varying conditions. These findings are crucial for improving the efficiency of supercavitating vehicles and underwater systems, where precise control over cavity size is essential for performance and stability. Future work could extend these simulations to explore the impact of other fluid properties and geometries, further refining our understanding of supercavitation.

71

Chapter 5

Exploring the implementation of secondary cavitators for enlargement of supercavity size

5.1 Introduction

This chapter explores the dynamics of supercavitation, focusing on enhancing the supercavity through the use of secondary cavitators, a novel concept aimed at achieving more efficient underwater propulsion. Traditionally, supercavitation has been achieved using a single cavitator, often mounted at the nose of an underwater vehicle, which generates a vapor-filled cavity around the body as the pressure around the vehicle drops below the vapor pressure of the liquid. However, studies have shown that a secondary cavitator, positioned at the appropriate location along the vehicle's body, can significantly amplify the size of the supercavity, resulting in greater drag reduction and higher operational efficiency. By introducing a secondary cavitator, the formation of an elongated supercavity becomes possible, even at lower speeds, making it feasible to achieve high-speed underwater locomotion without compromising the vehicle's structural integrity or propulsion capabilities.

This chapter investigates the interaction between the primary and secondary cavitators in generating an extended supercavity. Through numerical simulations, the effects of different cavitator sizes and configurations are analyzed across varying Froude numbers. The analysis demonstrates how the secondary cavitator enhances the overall supercavity size by merging with the primary cavity under optimal conditions. This research sheds light on the critical parameters, such as cavitator shape, size, and placement, which must be carefully tuned to maximize the supercavity and achieve efficient underwater propulsion. The next section

discusses the geometry of primary and secondary cavitators for conducting simulations.

5.1.1 Geometry

The torpedo geometry used in this study remains the same as that reported in Chapter 3. A 150mm-long circular rod connects the torpedo's nose to the cavitator body. A disc-shaped cavitator is used in the current study to produce the supercavity around the torpedo. The diameter of the torpedo and the primary cavitator is denoted by d_v and d_{pc} respectively. The height of the secondary cavitator is represented by h_{sc} as illustrated in Fig. 5.1.
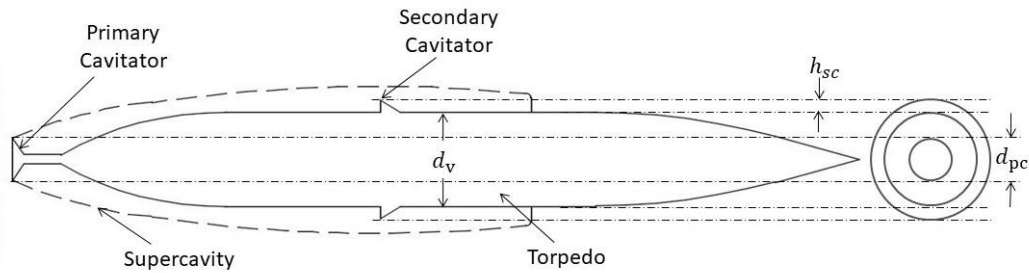
Fig. 5.1: Torpedo installed with primary and secondary cavitator

The ratio of the primary cavitator diameter to the torpedo diameter is defined as $\tilde{d}_{cv}$. The study is conducted on the primary cavitator with three different diameters corresponding to $\tilde{d}_{cv}$ of 0.40, 0.45, and 0.50. The secondary cavitator is positioned at 80% of the length of the supercavity that the primary cavitator produces. The ratio of the height of the secondary cavitator to the diameter of the primary cavitator is defined as $\tilde{d}_{sp}$. In the present work, the study is carried out on eight different secondary cavitator size ranges from $\tilde{d}_{sp} = 0.01 - 0.08$.

5.1.2 Meshing

To finalize the mesh for the present study, a grid independence test is conducted using four structured meshes with different numbers of elements. The first mesh, referred to as Mesh-1, contains around 43,000 elements. For the second mesh (Mesh-2), the number of elements is multiplied by 1.42, resulting in approximately

61,000 elements. The choice of 1.42 allows for a progressive refinement without overwhelming the computational resources. This is a standard factor which is used by previous researcher during grid independence study. Similarly, the third mesh (Mesh-3) and fourth mesh (Mesh-4) contain 87,000 and 123,000 elements, respectively. The details of all the meshes are tabulated in Table 5.1.

Table 5.1: Properties of meshes used for grid independence test

Mesh	No. of elements	Wall Distance	Y+ Value
Mesh-1	43,000	$6.7 \, X \, 10^{-5} \, m$	150
Mesh-2	61,000	$4.5 \, X \, 10^{-5} m$	100
Mesh-3	87,000	$1.8 \, X \, 10^{-5} m$	40
Mesh-4	123,000	$9 \, X \, 10^{-6} m$	20

The simulation is conducted at a Froude number (Fr) of 5 on a torpedo with only a primary cavitator having a diameter corresponding to $\tilde{d}_{cv}$ of 0.4. The non-dimensional length of the supercavity, calculated as $\tilde{L} = L/d_c$, where L is the supercavity length and d_c is the cavitator's diameter is compared for each case as shown in Fig. 5.2. It is observed that $\tilde{L}$ for Mesh-1 is smaller compared to the other meshes. However, it is approximately same for Mesh-2, Mesh-3, and Mesh-4.
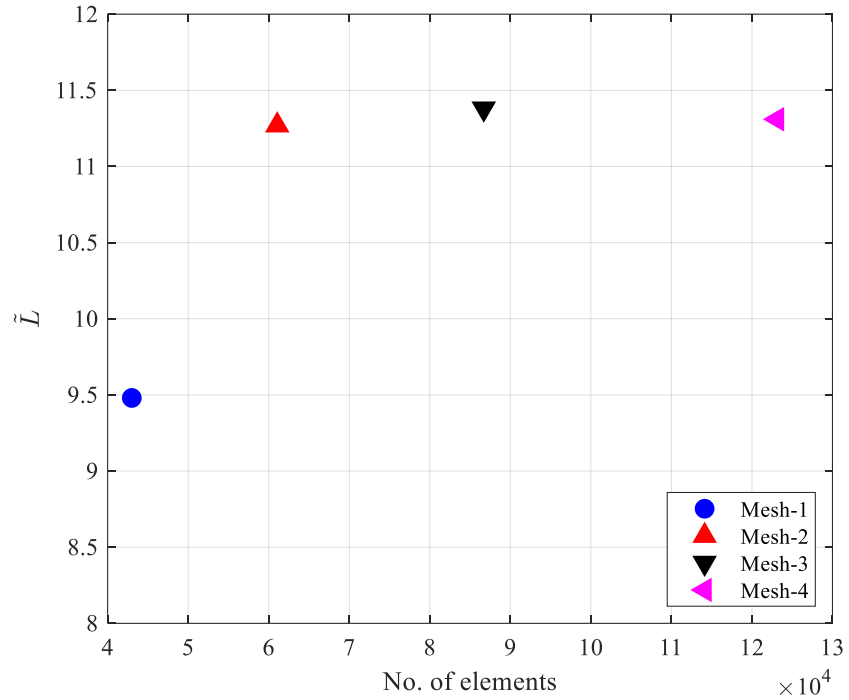
Fig. 5.2: Variation of non-dimensional supercavity half-length (L̃) with number
of elements present in various grids

Therefore, Mesh-2, with around 61K elements, is selected for the present study, as
shown in Fig. 5.3(a). The element size is kept finer near the solid surface to capture
the boundary layer and then gradually increases with a growth rate of 1.2 as shown
in Fig. 5.3(b). The first cell height is decided based on the Reynolds number range.
The smallest element size which is placed on the surface of the solid object
corresponds to a y^+ distance of 40, which is outside the viscous sublayer. The
properties inside the viscous sublayer are calculated using the wall function.
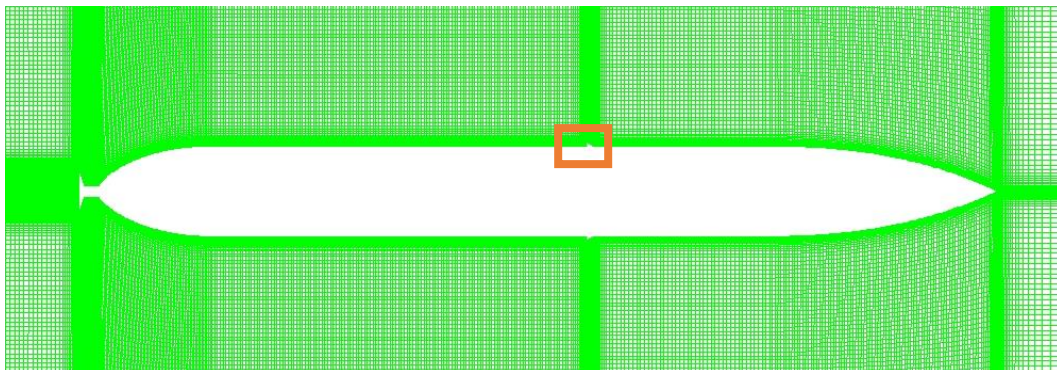
(a)
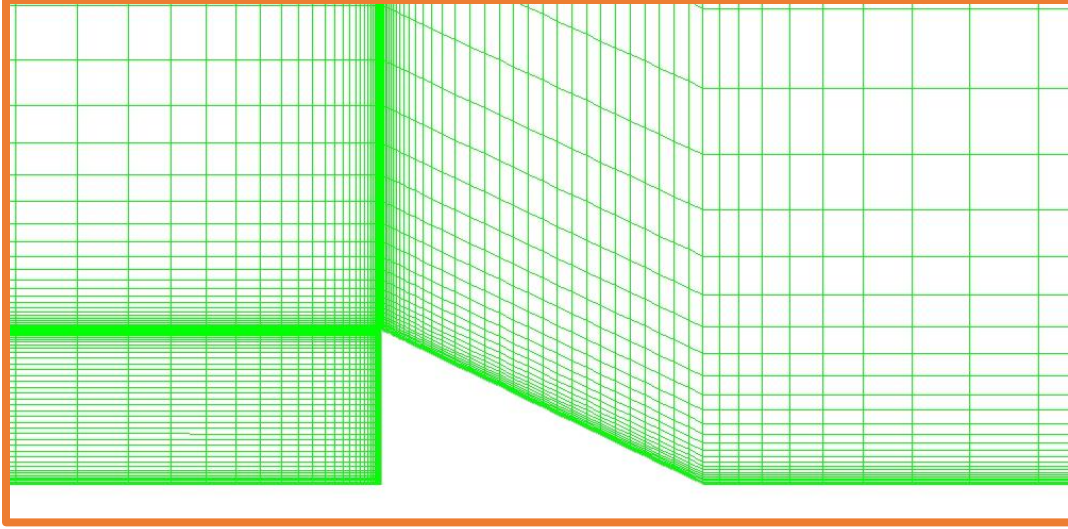
(b)

Fig. 5.3: (a) Spatial discretization of fluid (b) Close up view of the mesh near secondary cavitator

5.1.3 Computational Methodology

The computational methodology employed in this chapter is similar to the approach detailed in Section 3.1.3, ensuring consistency in the numerical framework throughout the study.

5.1.4 Simulation Cases

For torpedo with a primary cavitator, the size of the supercavity depends on the size of the primary cavitator, velocity of the torpedo, fluid properties and depth of the torpedo. these parameters can be consolidated to two non-dimensional parameters i.e. Froude number defined as $Fr = U/\sqrt{gd_v}$ and ratio of diameter of primary cavitator to the vehicle ($\tilde{d}_{cv} = d_{pc}/d_v$). If secondary cavitator is also introduced, then the supercavity size will also depend on the height of the seconday cavitator, which can be converted to non-dimensional form using the diameter of primary cavitator ($\tilde{d}_{sp} = d_{sc}/d_{pc}$). In present study, the simaulations are conducted on three different primary cavitator size corresponding to $\tilde{d}_{cv} = 0.4, 0.45$ and 0.5. Each cavitator generates a supercavity which ends on the surface of torpedo only for a specific range of Froude number. Therefore, for $\tilde{d}_{cv}$ of 0.45 and 0.5, the simulation

76

is conducted at Fr of 5 and 5.5; whereas, for $\tilde{d}_{cv}$ of 0.4, the simulation is conducted at Fr of 5.5 and 6. Therefore, the present study can be sub-divided in six distinct cases with three different primary cavitator size and two different Froude number. For all six cases, nine different values of $\tilde{d}_{sp}$ is simulated starting from 0 to 0.8 with an increment of 0.1 in each case. Therefore, for a specific value of Froude number and $\tilde{d}_{cv}$, nine simulations are carried out that sums up to 54 simulations. Apart from this, to understand the effect of flow velocity and depth explicitly on the optimized value of $\tilde{d}_{sp}$, ten more simulations are carried out at four additional values of velocity and six additional values of depth. Therefore, a total of 64 simulations are carried out in the present investigation.

5.2 Results

5.2.1 Supercavitation with primary cavitator

Supercavity generated with the primary cavitator ends on the torpedo surface for the range of Froude number considered in this investigation as shown in Fig. 5.4. "Inset (a)" shows the streamlines near primary cavitator. The flow upstream of the primary cavitator is deflected by the cavitator away from the surface, this gives rise to the energy of expansion which in turn forms the supercavity as mention in previous literatures (Semenenko, 2001). It is observed that a circulation zone of water vapour is formed after the primary cavitator. This happens because the vapour start travelling upstream due to adverse pressure gradient. "Inset (b)" shows the geometry of supercavity at the closure. It is worthy to notice that at this location, the water vapour has dissipated its energy, and have no energy to overcome the pressure force of liquid and thus starts travel upstream. This formed a recirculation zone, and the vapour gradually condenses back to liquid. This happens when hydrostatic pressure gradient is negligible as compared to the dynamic forces and thus the cavity closely resembles an axisymmetric shape. This types of closure are referred as re-entrant jet in the previous literature (Semenenko, 2001). In these cases, the reduction in drag is limited as the trailing part of the torpedo surface is still exposed to seawater. Therefore, to enlarge the supercavity size, higher speed

is required, which is not always possible due to limitation of propulsion system, material strength etc. To attain a supercavitation at this speed, installation of a secondary cavitator is proposed in this study which will be discussed in coming sections.
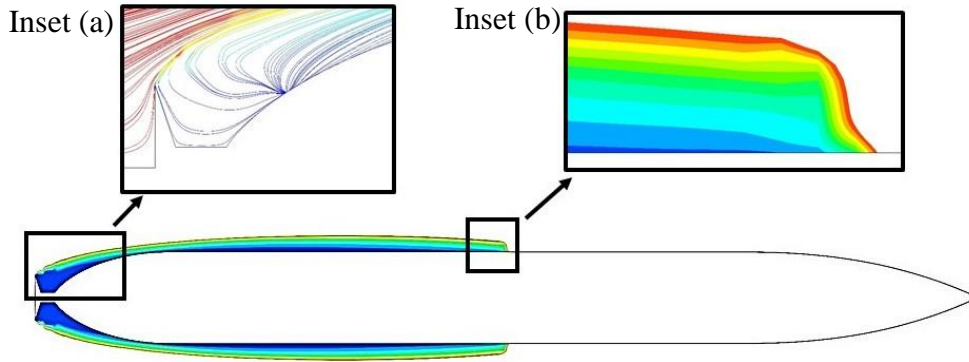
Fig. 5.4: Flow Properties of the supercavitation generated by primary cavitator; Inset (a) is showing the streamlines near the primary cavitator; Inset (b) show represents the zoomed in view of the shape of the supercavity closure

5.2.2 Secondary Supercavitation

The inclusion of a secondary cavitator leads to the formation of a secondary supercavity on the torpedo body. When the secondary supercavity interacts with the primary supercavity, a new supercavity is produced.

On investigating the flow close to the secondary cavitator, two distinct types of flow patterns are typically observed: one when the size of the secondary cavitator is smaller than the critical value, and the other when it is larger than the critical value. In cases where the secondary cavitator size is smaller than the critical value, it is observed that the secondary cavitator diverts the water vapor toward the periphery of the supercavity as shown in Fig. 5.5. In this process, a recirculating zone of water is created as a result of the condensation of the water vapor just ahead of the secondary cavitator. The vapor travels over this region of recirculation and proceeds in the direction of the supercavity's perimeter. This forces the supercavity's boundary to expand, increasing the size of the supercavity. The flow behind the secondary cavitator is closely similar to that of the step flow. When the

78

secondary cavitator size exceeds the critical value, the water stream strikes the cavitator and starts flowing in the opposite direction in form of a powerful jet. This reverse flow leads to a shrinkage of the primary supercavity.
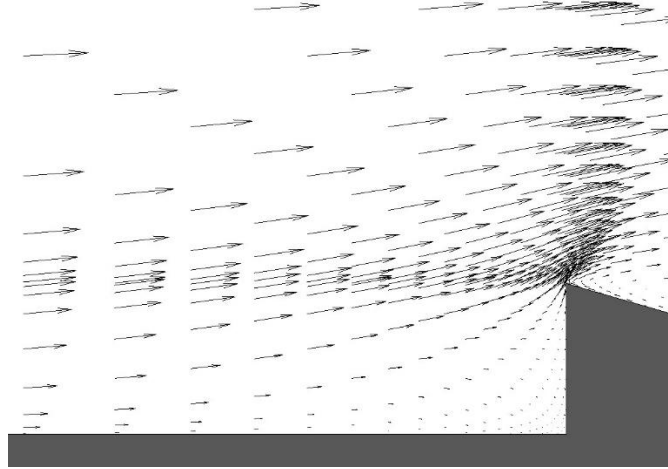
Fig. 5.5: Velocity vectors of the flow near the secondary cavitator

5.2.3 Optimization of the location of the secondary cavitator

To find out the best suited location of the secondary cavitator on the surface of the torpedo, the simulations are conducted by placing the secondary cavitator at different locations. The simulation are conducted at cavitation number ranges from 0.05 – 0.09, that corresponds to Froude number of 6.41 to 8.88. The secondary cavitator is placed at 35%, 45%, 55% and 65% of the torpedo length.

The term, "Amplification factor" is introduced to quantify the supercavity's size enhancement. The coalescenced new supercavity's length (L_c) divided by the original length of the primary supercavity (L_{cp}) is defined as the amplification factor (Eqn. 6)

$$\eta = \frac{L_c}{L_{cp}} \qquad \qquad .....\text{Eqn. (5.1)}$$

Fig. 5.6 shows the amplification factor for various location of secondary cavitator for different cavitation number. When cavitator is placed at 35% of the torpedo

length, amplification factor peaks above 1.3 near cavitation number of 0.06, and then returns close to 1 as cavitation number increases beyond 0.08. When cavitator is placed at 45% of the torpedo length, amplification factor shows a rapid increase and becomes over 1.3 cavitation number of 0.6, followed by a sharp drop to near 1 as cavitation number approaches 0.07. When cavitator is placed at 55% of the torpedo length, amplification factor remains stable near 1 and then, there is a small peak around cavitation number of 0.7 after which it again decreases. When cavitator is placed at 65% of the torpedo length, amplification factor starts above 1.3 but drops sharply below 1 at cavitation number of 0.06. and then remains close to 1 for higher values of cavitation number.
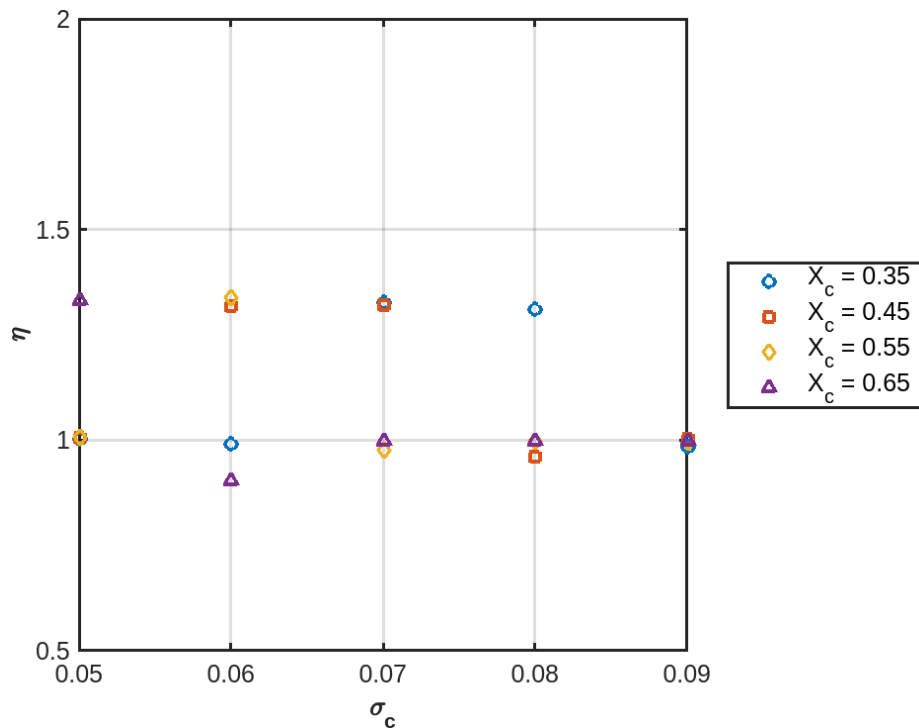
Fig. 5.6: Amplification factor for various location of secondary cavitator at different cavitation number

This suggest that the optimized location of cavitator depends on the cavitation number of the flow. For instance, when the cavitation number is around 0.08, the highest amplification is observed when the cavitator is placed at 35% of the torpedo length. However, when the cavitation number is 0.06, highest amplification factor is observed when secondary cavitator is placed 55% of the torpedo length. Table

5.2 shows the optimal location of secondary cavitator in percentage of the torpedo length for various cavitation numbers.

Table 5.2**:** Optimum location of secondary cavitator for various cavitation numbers

Cavitation Number	Optimal Location of secondary cavitator in percentage of torpedo's length.	Corresponding Amplification Factor
0.05	65 %	1.33
0.06	45% - 55%	1.32 – 1.34
0.07	35% - 45%	1.32 – 1.33
0.08	35%	1.31

The results indicate that the size of the cavitation number and hence the primary supercavity plays an important role in placing the secondary cavitator. Therefore, the amplification factor is plotted with the cavitator location in percentage of primary supercavity length X_{cs} for all the cases as shown in Fig. 5.7. It is observed that the maximum amplification factor is obtained when secondary cavitator is placed from 70% to 90% of the supercavity length.
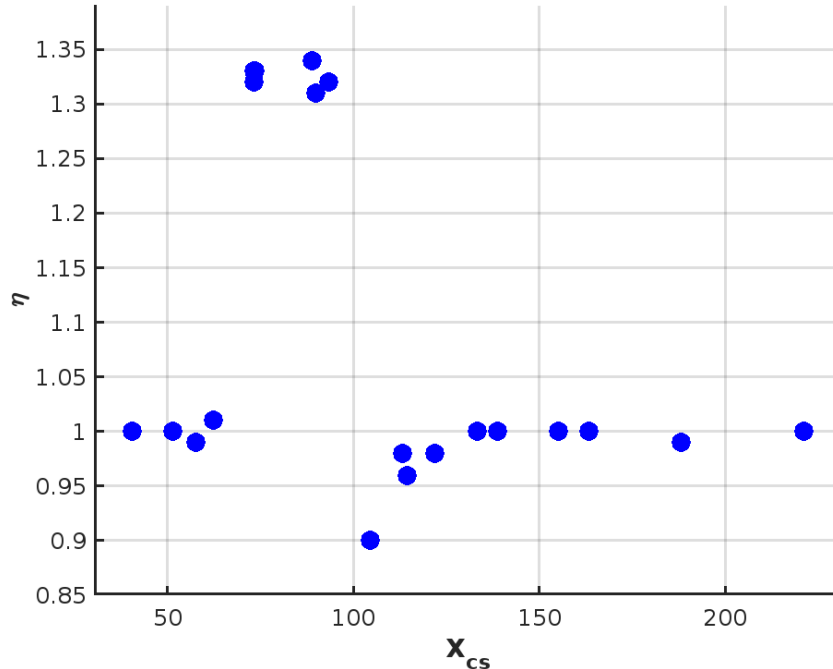
Fig. 5.7: Variation of amplification factor with the secondary cavitator location in percentage of primary supercavity length (X_{cs}).

5.2.4 Amplification factor for different $\tilde{d}_{sp}$

For further study, the secondary cavitator is installed at 80% of the primary supercavity's length. It was observed that the amplification factor depends prominently on the size of the secondary cavitator. To understand the dependence more clearly, the amplification factor is plotted against $\tilde{d}_{sp}$ (Fig. 5.8) for various cases with varying $\tilde{d}_{cv}$, Fr. It was observed that the amplification factor (η) increases with an increase in $\tilde{d}_{sp}$ up to a certain limit (Fig. 5.9(a), Fig. 5.9(b), Fig. 5.9 (c) and Fig. 5.9(d)). When amplification factor reaches its maximum value (Fig. 5.9(e)), the corresponding $\tilde{d}_{sp}$ is termed as critical $\tilde{d}_{sp}$ ($\tilde{d}_{sp}^*$). The increase in the supercavity length is because the secondary cavitator deflect the vapour away from the surface. This causes the expansion of the vapour which in turn increase the supercavity size. Further increasing the value of $\tilde{d}_{sp}$ initiated the formation of water jets in the upstream direction, which suddenly suppresses the primary supercavity prominently as shown in Fig. 5.9(f). Though, the large size of the secondary cavitator forms a larger secondary supercavity but it does not merge with the primary supercavity. In such cases, even with the presence of a large secondary cavity, the surface of the torpedo upstream of the secondary cavitator remains in contact with water as shown in Fig. 5.9(g), Fig. 5.9(h) and Fig. 5.9(i).
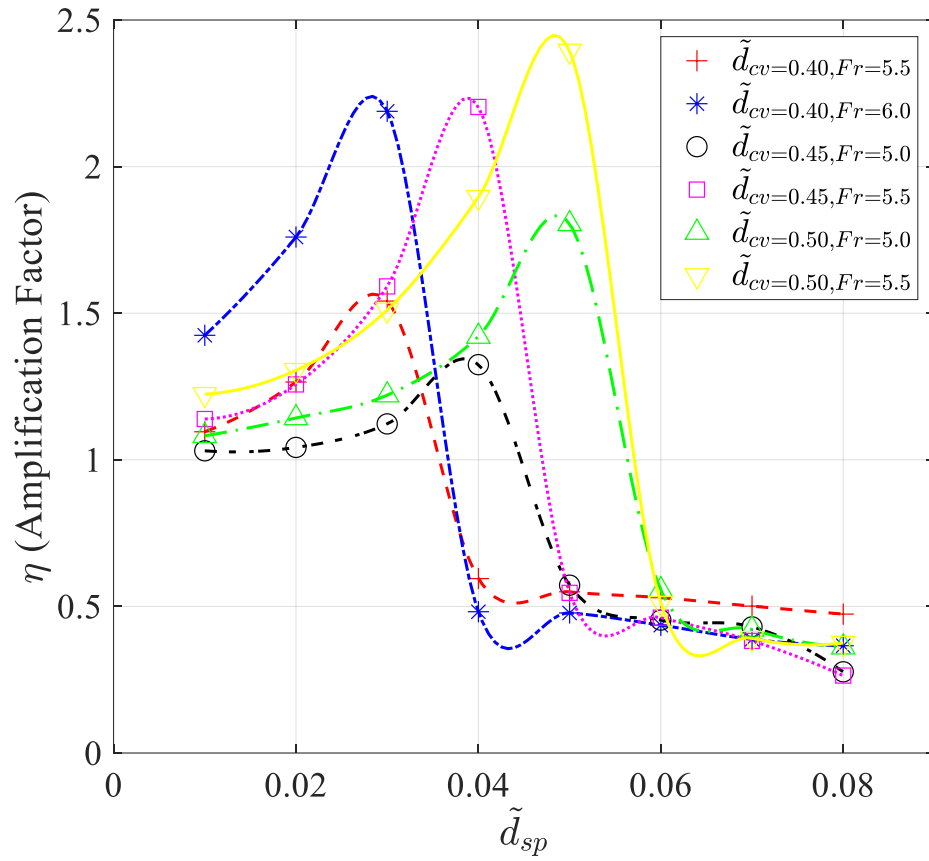
Fig. 5.8: Variation of amplification factor (η) with $\tilde{d}_{sp}$
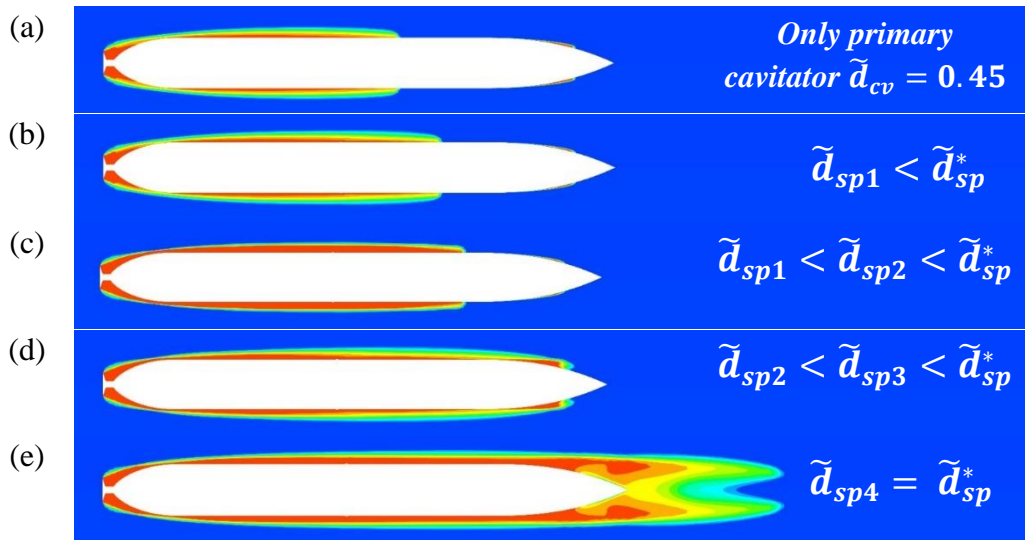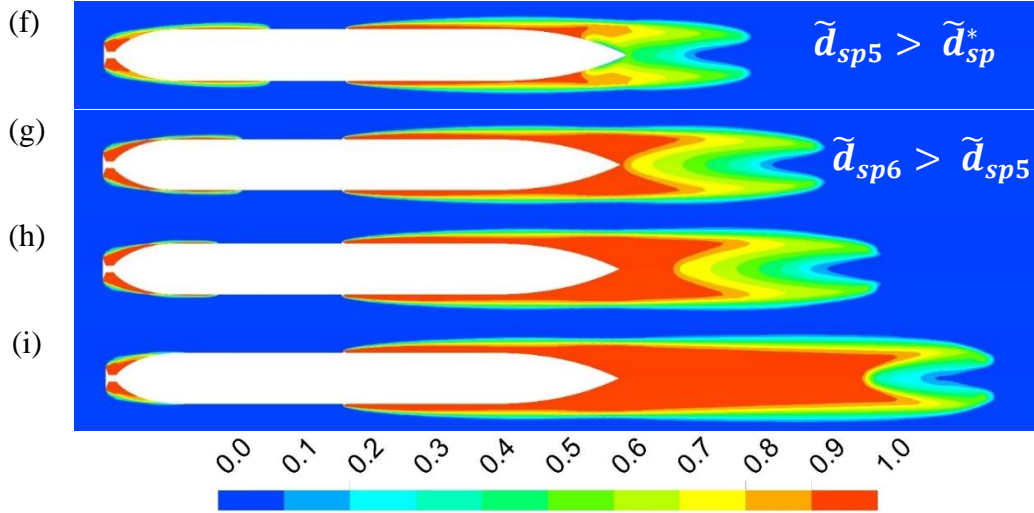
Fig. 5.9: Contour of volume fraction of water vapour over the torpedo with primary cavitator diameter corresponds to $\tilde{d}_{cv}$= 0.45 at Fr=5.5 with secondary cavitator diameter corresponds to $\tilde{d}_{sp}$ of (a) No secondary cavitator, (b) 0.01, (c) 0.02, (d) 0.03, (e) 0.04, (f) 0.05, (g) 0,06 (h) 0.07, and (i) 0.08

5.2.5 Effect of primary cavitator size $(\widetilde{\boldsymbol{d}}_{cv})$ on $\widetilde{\boldsymbol{d}}_{sp}^{*}$

The shift in the peak of the curves of amplification factor plotted in Fig. 5.8 for various $\tilde{d}_{cv}$ is observed. Therefore, $\tilde{d}_{sp}^{*}$ is plotted against $\tilde{d}_{cv}$ in Fig. 5.10, the data shows that the value of $\tilde{d}_{sp}^{*}$ is correspondingly 0.03, 0.04, and 0.05 for $\tilde{d}_{cv}$ of 0.40, 0.45, and 0.5. This demonstrates that as the primary cavitator's size ($\tilde{d}_{cv}$) increases, the value of $\tilde{d}_{sp}^{*}$ rises as well.
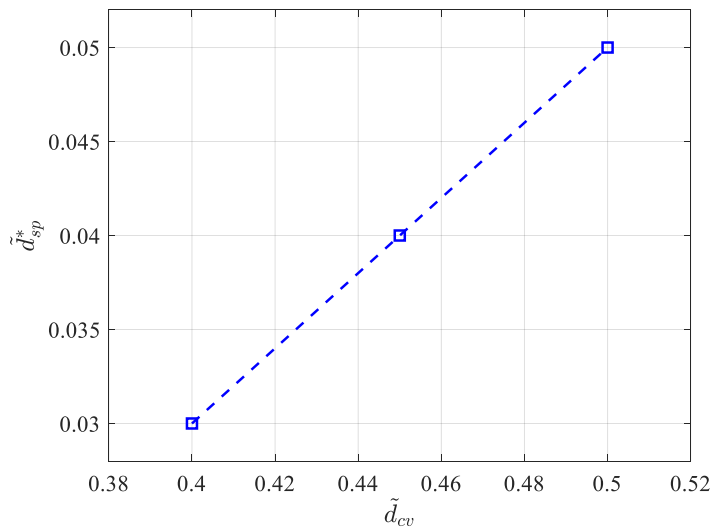
Fig. 5.10: Variation of critical $\tilde{d}_{sp}$ ($\tilde{d}_{sp}^{*}$) with the primary cavitator diameter

5.2.6 Effect of velocity on amplification factor (η) at $\tilde{d}_{sp}^*$

To better comprehend the effect of velocity on the amplification factor, the simulations are performed at a constant value of $\tilde{d}_{cv}$, i.e., 0.5 at $\tilde{d}_{sp}^*$ (0.05 for this case), with and without a secondary cavitator. The simulations are carried out at velocities between 47.5 and 60 m/s, which is corresponding to the Froude number range of 4.75 and 6. When the velocity exceeds 60 m/s, the primary cavitator develops a supercavity large enough to encompass the entire torpedo; whereas, when the velocity is dropped less than 47.5 m/s, the cavitation bubble produced by the primary cavitator is very small. In both scenarios, the secondary cavitator becomes ineffective and the primary cavitator dictates the size of the cavity over the torpedo. The supercavity length is compared both with and without a secondary cavitator, and thus the amplification factor is plotted against the Froude Number in Fig. 5.11. It is apparent from the graph that the amplification factor increases with the flow velocity. It also illustrates that the secondary cavitator though placed at 80% of supercavity length for a fixed value of velocity, also plays a crucial role in enhancing the supercavity size even at other nearby velocity regimes.
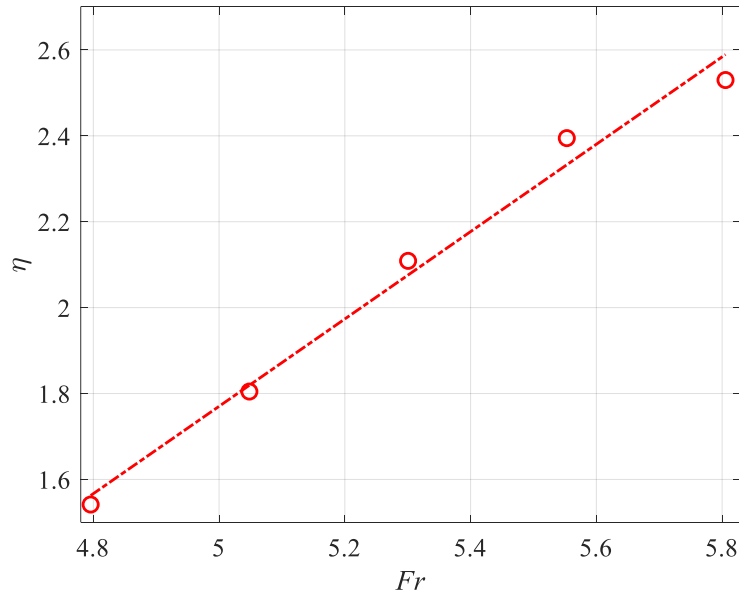
Fig. 5.11: Variation of amplification factor (η) with the velocity represented in terms of Froude number of the torpedo at secondary cavitator size corresponds to critical $\tilde{d}_{sp}$

5.2.7 Effect of depth on amplification factor (η) at $\widetilde{d}_{sp}^*$

The simulations are performed at various depths to better understand the impact of torpedo depth on the amplification factor. The simulations are carried out at a depth between 9 and 16 meters, or between 4.4 and 5.9 on the Froude scale. The primary cavitator generates a supercavity large enough to envelop the entire torpedo when the torpedo is raised above 9 meters, but it only creates a very small cavitation bubble when the torpedo is dropped below 16 meters. In either case, the primary cavitator regulates the size of the cavity over the torpedo while the secondary cavitator loses its efficacy. For each case, the amplification factor is represented against the Froude Number in Fig. 5.12. The graph indicates that as torpedo depth increases, the amplification factor decreases. This occurs because the increase in depth causes a reduction in the Froude number, which ultimately lowers the flow's capacity to cavitate. As a result, the supercavity size as well as the amplification factor is decreased.
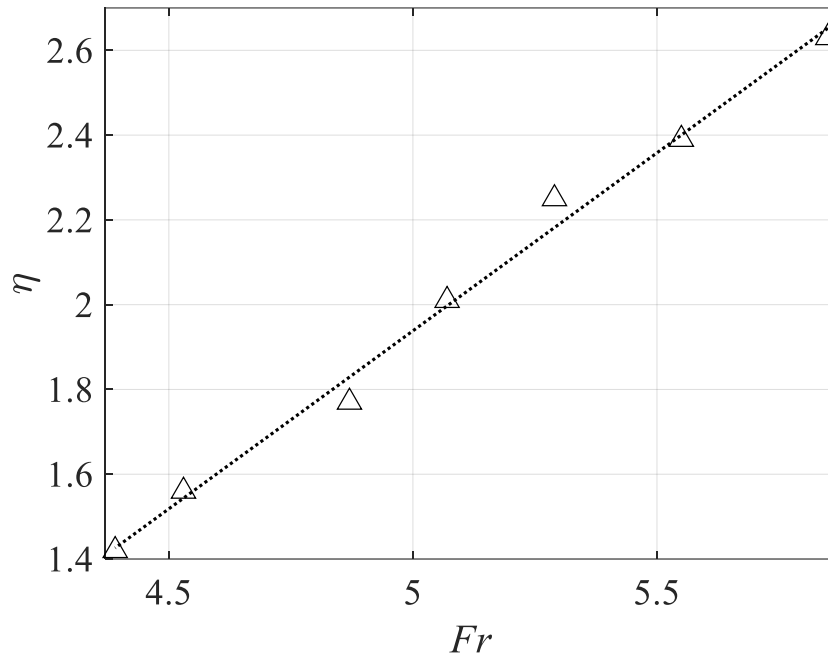
Fig. 5.12: Variation of amplification factor (η) with the depth of torpedo underwater represented in terms of Froude number at secondary cavitator size corresponds to $\tilde{d}_{sp}^*$

5.3 Significance of the findings

The simulations are carried out over various geometries with varying diameter of primary cavitator ($\tilde{d}_{cv} = 0.4 - 0.5$) and secondary cavitator ($\tilde{d}_{sp} = 0.01 - 0.07$) at different Froude numbers. In present study, a novel concept of installing a secondary cavitator on the surface of the torpedo is proposed to achieve supercavitation at comparatively lower speeds. The secondary cavitator generates a secondary supercavity, which interacts with the primary supercavity to form a resulting cavity. The resulting cavity primarily depends on the location and height of the secondary cavitator. Through a series of systematic experiments, it has been deduced that the secondary cavitator is most effective when placed at 70% - 90% of the length of primary supercavity. Therefore, while evaluating the effect of the height, the secondary cavitator is placed at 80% length of the primary supercavity. Further it is observed that if the size of the secondary cavitator is smaller than the critical value ($\tilde{d}_{sp} < \tilde{d}_{sp}^*$), then the secondary supercavity coalesce with the primary supercavity and forms a new larger supercavity. The size of the newly formed coalesced supercavity can be increased by increasing the height of the secondary cavitator. On the other hand, if the size of the secondary cavitator exceeds the critical value ($\tilde{d}_{sp} > \tilde{d}_{sp}^*$), then the seconday cavitator supress the primary supercavity. In these cases, a larger secondary supercavity forms but will not coalesce with primary supercavity. Therefore, it can be interpreted that the amplification factor initially increases with d_{sp}, upto certain limit referred as critical $\tilde{d}_{sp}$ ($\tilde{d}_{sp}^*$), then decreases suddenly. It is also observed that the critical size of secondary cavitator ($\tilde{d}_{sp}^*$) increases with increase in the size of the primary cavitator ($\tilde{d}_{cv}$). To test the performance of the critical secondary cavitator size at different flow conditions, simulation are conducted at different velocity and depth. It was found that on increasing the velocity of the vehicle, the amplification factor increases whereas on increasing the depth of the vehicle, the amplification factor decreases at fixed value of $\tilde{d}_{cv}$ and $\tilde{d}_{sp}$.

Chapter 6

Conclusions and future scope

Supercavitation and its enlargement stand as crucial areas of exploration in fluid dynamics, with a direct impact on reducing drag in high-speed underwater vehicles like torpedoes. The generation and manipulation of supercavities through different cavitator geometries have significant implications for performance optimization. Through a series of studies, it becomes clear that both primary cavitators and innovative enhancements, such as secondary cavitators, play a pivotal role in controlling supercavity size and effectiveness.

The first study focuses on the formation and coalescence of bubbles, drawing parallels to supercavitation in terms of how fluid forces and geometrical parameters dictate the behavior of bubbles in different fluids. Similar to the interaction between leading and trailing bubbles, where the wake of one bubble elongates the other, supercavitation involves complex interactions between the cavitator and the surrounding fluid. By analyzing bubble shapes through non-dimensional numbers like Reynolds, Weber, and Froude numbers, researchers derived scaling laws that can predict fluid behavior in different conditions. These insights into bubble dynamics can be analogously applied to supercavitation, where the forces at play—such as viscous, gravitational, and inertial forces—must be balanced to optimize cavity size and stability.

In the second study, supercavitation is directly explored by simulating different cavitator geometry. The ability of a cavitator to deflect flow radially outward determines the size of the resulting supercavity. Among various shapes, the disc cavitator produced the most expansive supercavity, with the size increasing as the cavitation number decreased. However, the cavitator's shape, not just the cavitation number, was the critical factor in generating a large supercavity. The study also

highlights the trade-off between reducing skin friction drag and increasing pressure drag, emphasizing the importance of selecting cavitators that create a supercavity large enough to encapsulate the torpedo. If the supercavity is too small, skin friction drag increases, while excessively large supercavities lead to higher pressure drag due to larger stagnation regions. This delicate balance between supercavity size and drag reduction is central to optimizing underwater vehicle performance.

The third study highlights the crucial role of fluid operating temperature in controlling the geometry of supercavities. As the difference in the operating temperature and the fluid's saturation temperature decreases, there is a noticeable increase in supercavity length, especially at lower cavitation numbers. This temperature sensitivity decreases as the cavitation number increases, indicating a complex interaction between temperature and cavitation dynamics. The study successfully models the relationship between cavitation number and non-dimensional critical temperature using a quadratic equation, offering a predictive framework for evaluating supercavity behavior under different conditions. These findings are essential for optimizing the performance and stability of supercavitating vehicles by enabling precise control over cavity size.

The fourth study introduces a novel approach to enhancing supercavitation using secondary cavitators. The researchers propose installing a secondary cavitator on the surface of a torpedo to achieve supercavitation at lower speeds. The secondary cavitator generates an additional supercavity that interacts with the primary one, potentially forming a larger resulting cavity. The effectiveness of this enhancement depends on the size of the secondary cavitator relative to the primary one. If the secondary cavitator is smaller than a critical value, it coalesces with the primary supercavity to form a larger cavity. However, if it exceeds the critical size, the secondary cavitator suppresses the primary supercavity, preventing the formation of a larger unified cavity. This study underscores the potential for secondary cavitators to enhance supercavitation, provided that their size and placement are carefully optimized.

Overall, supercavitation and its enlargement through geometric manipulation are central to advancing the performance of high-speed underwater vehicles. Whether by selecting the optimal cavitator shape or enhancing supercavity size with secondary cavitators, a deep understanding of fluid dynamics and cavitation is essential. By leveraging these insights, engineers can minimize drag, improve vehicle speed and efficiency, and advance the capabilities of underwater technologies.

References:

Agostini, B., Revellin, R., & Thome, J. R. (2008). Elongated bubbles in microchannels. Part I: Experimental study and modeling of elongated bubble velocity. *International Journal of Multiphase Flow*, *34*(6), 590–601. https://doi.org/10.1016/j.ijmultiphaseflow.2007.07.007

Al-Hayes, R. A. M., & Winterton, R. H. S. (1981). Bubble diameter on detachment in flowing liquids. *International Journal of Heat and Mass Transfer*, *24*(2), 223–230. https://doi.org/10.1016/0017-9310(81)90030-2

Alyanak, E., Grandhi, R., & Penmetsa, R. (2006). Optimum design of a supercavitating torpedo considering overall size, shape, and structural configuration. *International Journal of Solids and Structures*, *43*(3), 642–657. https://doi.org/10.1016/j.ijsolstr.2005.05.040

Arcanjo, A. A., Tibiriçá, C. B., & Ribatski, G. (2010). Evaluation of flow patterns and elongated bubble characteristics during the flow boiling of halocarbon refrigerants in a micro-scale channel. *Experimental Thermal and Fluid Science*, *34*(6), 766–775. https://doi.org/10.1016/j.expthermflusci.2010.01.006

Benhmidene, A., Chaouachi, B., & Gabsi, S. (2011). Effect of operating conditions on the performance of the bubble pump of absorption-diffusion refrigeration cycles. *Thermal Science*, *15*(3), 793–806.

Benzing, R. J., & Myers, J. E. (1955). Low Frequency Bubble Formation at Horizontal Circular Orifices. *Industrial \& Engineering Chemistry*, *47*(10), 2087–2090. https://doi.org/10.1021/ie50550a022

Calzavarini, E., Kerscher, M., Lohse, D., & Toschi, F. (2008). Dimensionality and morphology of particle and bubble clusters in turbulent flow. *Journal of Fluid Mechanics*, *607*, 13–24. https://doi.org/10.1017/S0022112008001936

Cao, L., Karn, A., Arndt, R. E., Wang, Z., & Hong, J. (2017). Numerical investigations of pressure distribution inside a ventilated supercavity. *Journal of Fluids Engineering*, *139*(2), 021301.

Chen, G., Sun, T., Yang, S., Miao, Z., & Tan, H. (2023). A study on the cavitating flow around an elliptical disk-shaped cavitator for non-body-of-revolution underwater vehicles. *Engineering Applications of Computational Fluid Mechanics*, *17*(1). Scopus. https://doi.org/10.1080/19942060.2022.2159882

Coulibaly, A., Bi, J., Lin, X., & Christopher, D. M. (2014). Effect of bubble coalescence on the wall heat transfer during subcooled pool boiling. *International Journal of Thermal Sciences*, *76*, 101–109. https://doi.org/10.1016/j.ijthermalsci.2013.08.019

Craig, V. S. J., Ninham, B. W., & Pashley, R. M. (1993a). Effect of electrolytes on bubble coalescence. *Nature*, *364*(6435), 317–319. https://doi.org/10.1038/364317a0

Craig, V. S. J., Ninham, B. W., & Pashley, R. M. (1993b). The effect of electrolytes on bubble coalescence in water. *The Journal of Physical Chemistry*, *97*(39), 10192–10197. https://doi.org/10.1021/j100141a047

De Jonge, R. M., Barendrecht, E., Janssen, L. J. J., & Van Stralen, S. J. D. (1982). Gas bubble behaviour and electrolyte resistance during water electrolysis. *International Journal of Hydrogen Energy*, *7*(11), 883–894.

Dular, M., Griessler-Bulc, T., Gutierrez-Aguirre, I., Heath, E., Kosjek, T., Krivograd Klemenčič, A., Oder, M., Petkovšek, M., Rački, N., Ravnikar, M., Šarc, A., Širok, B., Zupanc, M., Žitnik, M., & Kompare, B. (2016). Use of hydrodynamic cavitation in (waste)water treatment. *Ultrasonics Sonochemistry*, *29*, 577–588. https://doi.org/10.1016/j.ultsonch.2015.10.010

Fan, C., Li, Z., Du, M., & Yu, R. (2021). Numerical study on the influence of vehicle diameter reduction and diameter expansion on supercavitation.

Applied Ocean Research, *116*. Scopus. https://doi.org/10.1016/j.apor.2021.102870

Fan, X., Yang, Z., Parker, D. J., & Armstrong, B. (2008). Prediction of bubble behaviour in fluidised beds based on solid motion and flow structure. *Chemical Engineering Journal*, *140*(1–3), 358–369.

Gaurav, K., Mittal, G., & Karn, A. (2022). On the morphology of elongated bubbles during their formation at submerged orifices. *Chemical Engineering Science*, *250*, 117395. https://doi.org/10.1016/j.ces.2021.117395

Gerlach, D., Alleborn, N., Buwa, V., & Durst, F. (2007). Numerical simulation of periodic bubble formation at a submerged orifice with constant gas flow rate. *Chemical Engineering Science*, *62*(7), 2109–2125. https://doi.org/10.1016/j.ces.2006.12.061

Ivey, H. J. (1967). Relationships between bubble frequency, departure diameter and rise velocity in nucleate boiling. *International Journal of Heat and Mass Transfer*, *10*(8), 1023–1040. https://doi.org/10.1016/0017-9310(67)90118-4

Jiang, C.-X., Li, S.-L., Li, F.-C., & Li, W.-Y. (2017). Numerical study on axisymmetric ventilated supercavitation influenced by drag-reduction additives. *International Journal of Heat and Mass Transfer*, *115*, 62–76. https://doi.org/10.1016/j.ijheatmasstransfer.2017.08.015

Jiang, C.-X., Shuai, Z.-J., Zhang, X.-Y., Li, W.-Y., & Li, F.-C. (2016). Numerical study on the transient behavior of water-entry supercavitating flow around a cylindrical projectile influenced by turbulent drag-reducing additives. *Applied Thermal Engineering*, *104*, 450–460. https://doi.org/10.1016/j.applthermaleng.2016.05.102

Jiang, Y., Hong, J.-W., Pham, V.-D., & Ahn, B.-K. (2023). Experimental study on supercavitating flow by injection of 773 K ventilated gas. *European Journal of Mechanics - B/Fluids*, *99*, 136–147. https://doi.org/10.1016/j.euromechflu.2023.01.006

Karn, A., Arndt, R. E. A., & Hong, J. (2015). Dependence of supercavity closure upon flow unsteadiness. *Experimental Thermal and Fluid Science*, *68*, 493–498. https://doi.org/10.1016/j.expthermflusci.2015.06.011

Karn, A., Arndt, R. E. A., & Hong, J. (2016a). An experimental investigation into supercavity closure mechanisms. *Journal of Fluid Mechanics*, *789*, 259–284. https://doi.org/10.1017/jfm.2015.680

Karn, A., Arndt, R. E. A., & Hong, J. (2016b). Gas entrainment behaviors in the formation and collapse of a ventilated supercavity. *Experimental Thermal and Fluid Science*, *79*, 294–300. https://doi.org/10.1016/j.expthermflusci.2016.08.003

Karn, A., Arndt, R. E. A., & Hong, J. (2016c). Gas entrainment behaviors in the formation and collapse of a ventilated supercavity. *Experimental Thermal and Fluid Science*, *79*, 294–300. https://doi.org/10.1016/j.expthermflusci.2016.08.003

Karn, A., Arndt, R., & Hong, J. (2016d). Gas entrainment behaviors in the formation and collapse of a ventilated supercavity. *Experimental Thermal and Fluid Science*, *79*, 294–300.

Karn, A., & Chawdhary, S. (2018). On the synergistic interrelation between supercavity formation through vaporous and ventilated routes. *International Journal of Multiphase Flow*, *104*, 1–8. https://doi.org/10.1016/j.ijmultiphaseflow.2018.03.015

Karn, A., Ellis, C., Hong, J., & Arndt, R. (2015a). Investigations into the turbulent bubbly wake of a ventilated hydrofoil: Moving toward improved turbine aeration techniques. *Experimental Thermal and Fluid Science*, *64*, 186–195.

Karn, A., Ellis, C., Hong, J., & Arndt, R. E. A. (2015b). Investigations into the turbulent bubbly wake of a ventilated hydrofoil: Moving toward improved turbine aeration techniques. *Experimental Thermal and Fluid Science*, *64*, 186–195. https://doi.org/10.1016/j.expthermflusci.2014.12.011

Karn, A., Ellis, C. R., Milliren, C., Hong, J., Scott, D., Arndt, R. E. A., & Gulliver, J. S. (2015a). Bubble size characteristics in the wake of ventilated

94

hydrofoils with two aeration configurations. *International Journal of Fluid Machinery and Systems*, *8*(2), 73–83.

Karn, A., Monson, G., Ellis, C., Hong, J., Arndt, R., & Gulliver, J. (2015b). Mass transfer studies across ventilated hydrofoils: A step towards hydroturbine aeration. *International Journal of Heat and Mass Transfer*, *87*. https://doi.org/10.1016/j.ijheatmasstransfer.2015.04.021

Karn, A., Monson, G. M., Ellis, C. R., Hong, J., Arndt, R. E. A., & Gulliver, J. S. (2015c). Mass transfer studies across ventilated hydrofoils: A step towards hydroturbine aeration. *International Journal of Heat and Mass Transfer*, *87*, 512–520. https://doi.org/10.1016/j.ijheatmasstransfer.2015.04.021

Karn, A., & Rosiejka, B. (2017a). Air entrainment characteristics of artificial supercavities for free and constrained closure models. *Experimental Thermal and Fluid Science*, *81*, 364–369. https://doi.org/10.1016/j.expthermflusci.2016.10.003

Karn, A., & Rosiejka, B. (2017b). Air entrainment characteristics of artificial supercavities for free and constrained closure models. *Experimental Thermal and Fluid Science*, *81*, 364–369. https://doi.org/10.1016/j.expthermflusci.2016.10.003

Karn, A., Shao, S., Arndt, R., & Hong, J. (2016). Bubble coalescence and breakup in turbulent bubbly wake of a ventilated hydrofoil. *Experimental Thermal and Fluid Science*, *70*, 397–407.

Khadiya, S., Kumari, S., & Gupta, R. (2021). Hydrodynamics of bubble coalescence in microchannels. *The Canadian Journal of Chemical Engineering*, *99*(5), 1199–1210. https://doi.org/10.1002/cjce.23918

Kheradmandnia, S., Hashemi-Najafabadi, S., Shojaosadati, S. A., Mousavi, S. M., & Malek Khosravi, K. (2015). Development of parallel miniature bubble column bioreactors for fermentation process. *Journal of Chemical Technology \& Biotechnology*, *90*(6), 1051–1061.

Kim, M.-J., Kim, S.-H., Lee, K.-C., Paik, B.-G., & Kim, M.-C. (2021). Cavitator design for straight-running supercavitating torpedoes. *Applied Sciences (Switzerland)*, *11*(14). Scopus. https://doi.org/10.3390/app11146247

Kim, S., Lee, J., Lee, H., Lim, J., & Cho, J. (2022). Effect of rotating, non-axisymmetric cavitator on supercavity size. *Journal of Mechanical Science and Technology*, *36*(7), 3437–3447. Scopus. https://doi.org/10.1007/s12206-022-0622-8

Kyriakides, N. K., Kastrinakis, E. G., Nychas, S. G., & Goulas, A. (1997). Bubbling from nozzles submerged in water: Transitions between bubbling regimes. *The Canadian Journal of Chemical Engineering*, *75*(4), 684–691. https://doi.org/10.1002/cjce.5450750405

Leonard, C., Ferrasse, J.-H., Lefevre, S., Viand, A., & Boutin, O. (2021). Bubble rising velocity and bubble size distribution in columns at high pressure and temperature: From lab scale experiments to design parameters. *Chemical Engineering Research and Design*, *173*, 108–118. https://doi.org/10.1016/j.cherd.2021.07.003

Li, M., Hu, L., Xu, H., Chen, W., Xie, H., & Fu, X. (2019). Jet formation during the gas penetration through a thin liquid layer. *Physics of Fluids*, *31*(1), 17105. https://doi.org/10.1063/1.5066593

Likhachev, D. S., Li, F., & Kulagin, V. A. (2014). Experimental study on the performance of a rotational supercavitating evaporator for desalination. *Science China Technological Sciences*, *57*(11), 2115–2130. https://doi.org/10.1007/s11431-014-5631-0

Liu, B., Xiang, M., Xie, Z., & Zhang, W. (2023). On ventilated supercavities moving horizontally near free surface. *Ocean Engineering*, *267*. Scopus. https://doi.org/10.1016/j.oceaneng.2022.113229

Livinus, A., & Verdin, P. G. (2021). Experimental study of a single elongated bubble in liquid in under 10-degree upwardly inclined pipes. *Experimental Thermal and Fluid Science*, *120*, 110247. https://doi.org/10.1016/j.expthermflusci.2020.110247

Logvinovich, G. V., & Serebryakov, V. V. (1975). Methods of Calculating the Shape of Slender Axisymmetric Cavities. *Gidromekhanika*, *32*, 47–54. Scopus.

Matsuda, N., Kurobe, Y., Ukon, Y., Kudo, T., & Okamoto, M. (1994). Experimental investigation into the performance of supercavitating propellers. *Senpaku Gijutsu Kenkyusho Hokoku/Papers of Ship Research Institute*, *31*(5), 1–61. Scopus.

Mohseni, E., Jose Kalayathine, J., Reinecke, S. F., & Hampel, U. (2020). Dynamics of bubble formation at micro-orifices under constant gas flow conditions. *International Journal of Multiphase Flow*, *132*, 103407. https://doi.org/10.1016/j.ijmultiphaseflow.2020.103407

Muller, R. L., & Prince, R. G. H. (1972). Regimes of bubbling and jetting from submerged orifices. *Chemical Engineering Science*, *27*(8), 1583–1592. https://doi.org/10.1016/0009-2509(72)80051-4

Myring, D. F. (1976). *THEORETICAL STUDY OF BODY DRAG IN SUBCRITICAL AXISYMMETRIC FLOW. 27*(3), 186–194. Scopus.

Nesteruk, I. (2012). *Supercavitation: Advances and Perspectives A collection dedicated to the 70th jubilee of Yu.N. Savchenko*. Springer Science & Business Media.

Olmos, E., Gentric, C., Vial, C., Wild, G., & Midoux, N. (2001). Numerical simulation of multiphase flow in bubble column reactors. Influence of bubble coalescence and break-up. *Chemical Engineering Science*, *56*(21), 6359–6365. https://doi.org/10.1016/S0009-2509(01)00204-4

Olowson, P. A., & Almstedt, A. E. (1990). Influence of pressure and fluidization velocity on the bubble behaviour and gas flow distribution in a fluidized bed. *Chemical Engineering Science*, *45*(7), 1733–1741. https://doi.org/10.1016/0009-2509(90)87051-S

Orvalho, S., Stanovsky, P., & Ruzicka, M. C. (2021). Bubble coalescence in electrolytes: Effect of bubble approach velocity. *Chemical Engineering Journal*, *406*, 125926. https://doi.org/10.1016/j.cej.2020.125926

Painmanakul, P., Sastaravet, P., Lersjintanakarn, S., & Khaodhiar, S. (2010). Effect of bubble hydrodynamic and chemical dosage on treatment of oily wastewater by Induced Air Flotation (IAF) process. *Chemical Engineering Research and Design*, *88*(5), 693–702. https://doi.org/10.1016/j.cherd.2009.10.009

Park, H., & Wang, L. (2015). Experimental studies and modeling of surface bubble behaviour in froth flotation. *Chemical Engineering Research and Design*, *101*, 98–106.

Rajaseenivasan, T., & Srithar, K. (2017). An investigation into a laboratory scale bubble column humidification dehumidification desalination system powered by biomass energy. *Energy Conversion and Management*, *139*, 232–244.

Rajkumar, R., Gaurav, K., Karn, A., Kumar, V., & Shukla, H. (2023). Numerical Investigation of the Effect of Liquid Temperature on Supercavitation. In S. Narendranth, P. G. Mukunda, & U. K. Saha (Eds.), *Recent Advances in Mechanical Engineering* (pp. 19–27). Springer Nature. https://doi.org/10.1007/978-981-19-1388-4_2

Roig, V., Roudet, M., Risso, F., & Billet, A.-M. (2012). Dynamics of a high-Reynolds-number bubble rising within a thin gap. *Journal of Fluid Mechanics*, *707*, 444–466. https://doi.org/10.1017/jfm.2012.289

Sarc, A., Kosel, J., Stopar, D., Oder, M., & Dular, M. (2018). Removal of bacteria Legionella pneumophila, Escherichia coli, and Bacillus subtilis by (super)cavitation. *Ultrasonics Sonochemistry*, *42*, 228–236. https://doi.org/10.1016/j.ultsonch.2017.11.004

Schmid, A. (2010). New jet-aeration system using 'Supercavitation.' *Environmental Science and Pollution Research*, *17*(3), 582–585. https://doi.org/10.1007/s11356-009-0199-0

Schnerr, G. H., & Sauer, J. (2001). Physical and numerical modeling of unsteady cavitation dynamics. *Fourth International Conference on Multiphase Flow*, *1*.

Semenenko, V. N. (2001). *Artificial supercavitation. Physics and calculation*.

Shao, S., Balakrishna, A., Yoon, K., Li, J., Liu, Y., & Hong, J. (2020). Effect of mounting strut and cavitator shape on the ventilation demand for ventilated supercavitation. *Experimental Thermal and Fluid Science*, *118*. Scopus. https://doi.org/10.1016/j.expthermflusci.2020.110173

Shao, S., Karn, A., Ahn, B.-K., Arndt, R. E. A., & Hong, J. (2017). A comparative study of natural and ventilated supercavitation across two closed-wall water tunnel facilities. *Experimental Thermal and Fluid Science*, *88*, 519–529. https://doi.org/10.1016/j.expthermflusci.2017.07.005

Stover, R. L., Tobias, C. W., & Denn, M. M. (1997). Bubble coalescence dynamics. *AIChE Journal*, *43*(10), 2385–2392. https://doi.org/10.1002/aic.690431002

Tomov, P., Khelladi, S., Ravelet, F., Sarraf, C., Bakir, F., & Vertenoeuil, P. (2016). Experimental study of aerated cavitation in a horizontal venturi nozzle. *Experimental Thermal and Fluid Science*, *70*, 85–95. https://doi.org/10.1016/j.expthermflusci.2015.08.018

Waid, R. L. (1957). *Cavity shapes for circular disks at angles of attack*.

Wang, T., & Wang, J. (2007). Numerical simulations of gas–liquid mass transfer in bubble columns with a CFD–PBM coupled model. *Chemical Engineering Science*, *62*(24), 7107–7118. https://doi.org/10.1016/j.ces.2007.08.033

Wu, H., Wang, B., DiMarco, S. F., & Tan, L. (2021). Impact of bubble size on turbulent statistics in bubble plumes in unstratified quiescent water. *International Journal of Multiphase Flow*, *141*, 103692. https://doi.org/10.1016/j.ijmultiphaseflow.2021.103692

Xu, H., Wang, C., Wei, Y., & Cao, W. (2023). On the nonlinear hydrodynamic characteristic of a ventilated supercavitating vehicle with high Froude number. *Ocean Engineering*, *268*. Scopus. https://doi.org/10.1016/j.oceaneng.2022.113457

Yang, D., Xiong, Y. L., & Guo, X. F. (2017). Drag reduction of a rapid vehicle in supercavitating flow. *International Journal of Naval Architecture and*

Ocean Engineering, *9*(1), 35–44. https://doi.org/10.1016/j.ijnaoe.2016.07.003

Yang, W., Luo, Z., Lai, Q., & Zou, Z. (2019). Study on bubble coalescence and bouncing behaviors upon off-center collision in quiescent water. *Experimental Thermal and Fluid Science*, *104*, 199–208. https://doi.org/10.1016/j.expthermflusci.2019.02.016

Yi, J.-J., Kim, M.-J., Kim, S.-H., Paik, B.-G., & Kim, K. C. (2022). Prediction of supercavitation shapes for a wide range of Froude numbers. *International Journal of Naval Architecture and Ocean Engineering*, *14*. Scopus. https://doi.org/10.1016/j.ijnaoe.2021.11.009

Yi, W., Tan, J., & Xiong, T. (2009). Investigations on the drag reduction of high-speed natural supercavitation bodies. *Modern Physics Letters B*, *23*(03), 405–408. https://doi.org/10.1142/S0217984909018515

Zheng, Z.-Y., Li, Q., Wang, L., Yao, L.-M., Cai, W.-H., Kulagin, V. A., Li, H., & Li, F.-C. (2019). Numerical study on the effect of steam extraction on hydrodynamic characteristics of rotational supercavitating evaporator for desalination. *Desalination*, *455*, 1–18. https://doi.org/10.1016/j.desal.2018.12.012

Zhou, Y., Ji, B., Zhao, C., & Bo, H. (2021). Bubble formation from a submerged orifice in a thin liquid layer: Detachment and bursting. *Physics of Fluids*, *33*(1), 13305. https://doi.org/10.1063/5.0036330

List of Publications

1. Chemical Engineering Science (SCI Indexed Journal)

Kumar Gaurav, Gaurav Mittal, Ashish Karn, (2022)

On the morphology of elongated bubbles during their formation at submerged orifices, Chemical Engineering Science, Volume 250, 117395, ISSN 0009-2509, https://doi.org/10.1016/j.ces.2021.117395.

2. Journal of Applied Fluid Mechanics (SCI Indexed Journal)

Gaurav, K., Venkatesh, N., & Karn, A. (2024).

A Comparative Assessment of Various Cavitator Shapes for High-speed Supercavitating Torpedoes: Geometry, Flow-physics and Drag Considerations, Journal of Applied Fluid Mechanics, 17(9), 2028–2044.

https://doi.org/10.47176/jafm.17.9.2631

3. Recent Advances in Mechanical Engineering (Scopus Indexed Conference)

Rajkumar, R., Gaurav, K., Karn, A., Kumar, V., Shukla, H. (2023)

Numerical Investigation of the Effect of Liquid Temperature on Supercavitation, Recent Advances in Mechanical Engineering. Lecture Notes in Mechanical Engineering. Springer, Singapore.

https://doi.org/10.1007/978-981-19-1388-4_2

PhD Thesis

9%	**6**%	**9**%	**1**%
SIMILARITY INDEX	INTERNET SOURCES	PUBLICATIONS	STUDENT PAPERS

PRIMARY SOURCES

1 Ehsan Mohseni, Jaunty Jose Kalayathine, Sebastian Felix Reinecke, Uwe Hampel. "Dynamics of Bubble Formation at Micro-orifices under Constant Gas Flow Conditions", International Journal of Multiphase Flow, 2020
Publication
<1%

2 link.springer.com
Internet Source
<1%

3 conservancy.umn.edu
Internet Source
<1%

4 Wen-Ching Yang. "Handbook of Fluidization and Fluid-Particle Systems", CRC Press, 2003
Publication
<1%

5 Jong-Ju Yi, Min-Jae Kim, Seon-Hong Kim, Bu-Geun Paik, Kyung Chun Kim. "Prediction of supercavitation shapes for a wide range of Froude numbers", International Journal of Naval Architecture and Ocean Engineering, 2021
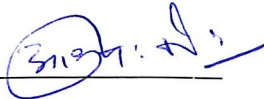Publication
<1%

UPES

PLAGIARISM CERTIFICATE

1. We _Dr. Ashish Karn_ (Internal Guide), ___–___(Co Guide/ External Guide) certify that the Thesis titled

   SYSTEMATIC INVESTIGATIONS ON SOME STRATEGIES FOR ENHANCEMENT OF SUPERCAVITY SIZE

   submitted by Scholar Mr/ Ms _KUMAR GAURAV_ having SAP ID _500072287_ has been run through a Plagiarism Check Software and the Plagiarism Percentage is reported to be _9_ %.

2. Plagiarism Report generated by the Plagiarism Software is attached .

_____
Signature of the Internal Guide

_____
Signature of External Guide/ Co Guide

_____
Signature of the Scholar